UNIVERSIDADE FEDERAL DE SANTA CATARINA
PROGRAMA DE PÓS-GRADUAÇÃO EM ENGENHARIA MECÂNICA

Filipe Dutra da Silva

WAVEPACKET MODELING WITH COHERENCE DECAY FOR PREDICTING JET-PLATE INTERACTION NOISE

Florianópolis
2017

Filipe Dutra da Silva

MODELAGEM DE PACOTES DE ONDA COM DECAIMENTO DE COERÊNCIA PARA PREVISÃO DO RUÍDO DA INTERAÇÃO JATO-PLACA.

Tese submetida ao Programa de Pós-Graduação em Engenharia Mecânica da Universidade Federal de Santa Catarina para a obtenção do título de Doutor em Engenharia Mecânica.

Orientador: Prof. César José Deschamps, Ph.D.
Coorientador: Prof. Andrey Ricardo da Silva, Ph.D.

Florianópolis
2017

Ficha de identificação da obra elaborada pelo autor,
através do Programa de Geração Automática da Biblioteca Universitária da UFSC.

Silva, Filipe Dutra da
Modelagem de pacotes de onda com decaimento de coerência para previsão do ruído da interação jato placa. / Filipe Dutra da Silva ; orientador, César José Deschamps, coorientador, Andrey Ricardo da Silva, 2017.
184 p.

Tese (doutorado) - Universidade Federal de Santa Catarina, Centro Tecnológico, Programa de Pós Graduação em Engenharia Mecânica, Florianópolis, 2017.

Inclui referências.

1. Engenharia Mecânica. 2. Ruído de jatos. 3. Interação jato-placa. 4. Pacotes de onda. I. Deschamps, César José. II. Silva, Andrey Ricardo da. III. Universidade Federal de Santa Catarina. Programa de Pós-Graduação em Engenharia Mecânica. IV. Título.

Filipe Dutra da Silva

MODELAGEM DE PACOTES DE ONDA COM DECAIMENTO DE COERÊNCIA PARA PREVISÃO DO RUÍDO DA INTERAÇÃO JATO-PLACA

Esta Tese foi julgada adequada para obtenção do Título de "Doutor em Engenharia Mecânica", e aprovada em sua forma final pelo Programa de Pós-Graduação em Engenharia Mecânica.

Florianópolis, 21 de Setembro de 2017.

Prof. Jonny Carlos da Silva, Dr.
Coordenador do Curso

Prof. César José Deschamps, Ph.D. - Orientador
Universidade Federal de Santa Catarina

Prof. Andrey Ricardo da Silva, Ph.D. - Coorientador
Universidade Federal de Santa Catarina

Banca Examinadora:

Prof. César José Deschamps, Ph.D. - Orientador
Universidade Federal de Santa Catarina

Prof. Daniel Rodriguez Álvarez, Ph.D.
Universidade Federal Fluminense

Prof. André Valdetaro Gomes Cavalieri, Dr.
Instituto Tecnológico de Aeronáutica

Prof. William Roberto Wolf, Ph.D.,
Universidade Estadual de Campinas
(videoconferência)

Prof. Juan Pablo de Lima Costa Salazar, Ph.D.
Universidade Federal de Santa Catarina

Prof. Júlio Apolinário Cordioli, Dr.
Universidade Federal de Santa Catarina

Aos meus pais por todo apoio e incentivo.
À minha noiva, Vanessa, por todo amor e carinho.

ACKNOWLEDGEMENTS

I would like to thank my supervisors Prof. César Deschamps and Prof. Andrey da Silva for the support provided during the research and for the opportunities to work in the jet-noise research field.

A very important part of this study was conducted in a 12-month academic exchange in the University of Poitiers, France, under the supervision of Peter Jordan. I would like to express my sincere gratitude to Peter Jordan for the constant support, guidance and encouragement to conclude this thesis. I also acknowledge the technical support provided by the *Centre d'Études Aérodynamiques & Thermiques* (CEAT).

I also acknowledge the research groups in ITA and at the University of Poitiers: Prof. André Cavalieri, Petrônio Nogueira, Selene Piantanida, Vincent Jaunet, Mengqi Zhang, Jerôme Huber and Maxime Le Rallic, for the valuable discussions and for the collaboration by either providing the experimental data used in this study or supporting the implementation of the codes. I also would like to thank Igor Maia and Francisco Lajus Jr. for their help and valuable opinions.

I would like to thank my fiancée, Vanessa, for the love, dedication and comprehension. I also express my gratitude to my parents, Adair and Maria Ivonete, and my brother Pablo, for the support and encouragement.

The present study was partially developed as part of a technical-scientific cooperation program between the Federal University of Santa Catarina and EMBRAER. I also acknowledge the support provided by EMBRAPII Unit Polo/UFSC, FINEP, CAPES and CNPq through Grants No.142293/2013-0 and No. 232820/2014-7 (Ph.D. Scholarships) and No. 465448/2014-3 (National Institute of Science and Technology in Refrigeration and Thermophysics).

The Large-eddy simulation used in this work was performed by Cascade Technologies with support from NAVAIR SBIR project, under the supervision of Dr. John T. Spyropoulos. The main LES calculations were carried out on DoD HPC systems in ERDC DSRC.

RESUMO

O jato proveniente da exaustão dos motores é uma das principais fontes de ruído em aeronaves. Além disso, a integração do motor com a estrutura da asa modifica o campo sonoro em relação ao jato isolado e é cada vez mais importante em novos projetos. Os pacotes de onda são estruturas com importante contribuição para o ruído de jatos, bem como no ruído da interação com o bordo de fuga. Neste trabalho, uma análise de modelos de pacotes de onda para previsão do ruído de jatos instalados foi realizada com o uso geometrias simplificadas. Explorou-se o ajuste dos modelos por meio de dados de escoamento provenientes de simulação numérica. Para tanto, avaliou-se a acurácia de modelos de simulação baseados no método de Lattice Boltzmann (LBM) e de grandes escalas das equações de Navier-Stokes (LES). Somente o modelo LES se mostrou suficientemente acurado para fornecer dados do escoamento requeridos no presente estudo. A partir da equação de Lighthill, um termo fonte simplificado foi extraído dos dados da simulação LES, considerando somente o modo axissimétrico e o primeiro termo do tensor de Lighthill. O campo acústico correspondente foi obtido através de uma abordagem baseada na estatística de dois pontos, utilizando as funções de Green de espaço livre, para o jato isolado, e uma função adaptada representativa de placa semi-infinita, para o jato instalado. Mesmo com essas simplificações, foi possível prever as principais características do campo acústico de jatos isolados e posicionados próximos a placas planas. Um modelo de pacote de onda volumétrico foi ajustado com base no termo fonte da simulação LES. Notaram-se desvios consideráveis na previsão da diretividade do jato isolado em relação ao experimento. Entretanto, boa concordância com os dados experimentais foi obtida com a presença da placa. Grandes diferenças foram também observadas entre resultados de densidade espectral cruzada da simulação LES e do modelo, possivelmente provenientes de erros das funções simplificadas usadas no ajuste dos parâmetros do modelo. Apesar desses erros, os efeitos de ruído do bordo de fuga da placa foram razoavelmente capturados. Além disso, avaliou-se a sensibilidade do campo acústico em relação à modelagem do decaimento de coerência. Os casos com a presença da placa se mostraram muito menos sensíveis a esse parâmetro do que no caso do jato isolado. Frente a elevada sensibilidade do jato isolado a erros nos parâmetros do modelo, avaliou-se também uma fonte

unidimensional, envolvendo maior facilidade nos ajustes. Esta foi ajustada com os dados LES integrados radialmente, o que levou melhorias consideráveis na previsão do ruído de jato isolado em baixo número de Strouhal. Em uma avaliação geral, a modelagem para previsão de ruído de jatos instalados se mostrou muito mais simples, com resultados muito menos sensíveis a variações nas características da fonte.

Palavras-chave: Ruído de jato, interação jato-placa, pacotes de onda.

RESUMO EXPANDIDO

Introdução

O jato proveniente da exaustão dos motores é uma das principais fontes de ruído em aeronaves. Além disso, a integração do motor com a estrutura da asa modifica o campo sonoro em relação ao jato isolado e é cada vez mais importante em novos projetos. Neste sentido, o ruído proveniente do espalhamento acústico no bordo de fuga da asa é uma fonte importante em baixas frequências. Os pacotes de onda são estruturas coerentes com importante contribuição para o ruído de jatos, bem como no ruído da interação com o bordo de fuga. Existe uma demanda por métodos simples de previsão de ruído baseados em aspectos físicos dos mecanismos de geração de ruído, tanto para jato isolado quanto para jatos instalados. Neste sentido, a ideia da modelagem baseada em estruturas coerentes, ou pacotes de onda, se torna atrativa, devido a baixa ordem dessas estruturas em comparação com o escoamento não-linear de um jato turbulento.

Objetivos

Esse trabalho teve como objetivo analisar um modelo de pacote de onda ajustado com dados numéricos do escoamento para a previsão o ruído da interação jato-placa. Objetivos específicos envolveram a análise de simplificações nos termos do termo fonte de Lighthill, a avaliação do ajuste dos modelos por meio de dados de escoamento provenientes de simulação numérica de alta fidelidade e a análise dos efeitos do decaimento de coerência em configurações jato-placa.

Metodologia

Primeiramente, avaliou-se a acurácia de simulações baseadas no método de Lattice Boltzmann (LBM) e de grandes escalas das equações de Navier-Stokes (LES) para fornecer dados para o ajuste dos parâmetros dos modelos de pacote de onda. Em seguida, a partir da equação de Lighthill, um termo fonte simplificado foi extraído dos dados da simulação LES, considerando somente o modo axissimétrico e o primeiro termo do tensor ($T_{xx}(m = 0)$). O campo acústico correspondente foi obtido através de uma abordagem baseada na estatística de dois pontos, utilizando as funções de Green de espaço livre, para o jato isolado, e uma

função adaptada, representativa de placa semi-infinita, para o jato instalado. Por fim, variações de modelos de pacotes de onda apresentados na literatura foram utilizados. Os parâmetros dos modelos de pacote de onda foram ajustados com base nos resultados fluidodinâmicos da base de dados numérica. As capacidades de previsão dos modelos foram avaliadas.

Resultados e Discussão

Através de um código comercial baseado no método de Lattice Boltzmann, avaliaram-se modelos de simulação para jato simples isolado com números de Mach 0.4 e 0.9. Apesar de aceitáveis em um contexto de indústria, os resultados não foram considerados suficientemente acurados para a estudo em questão, apresentando inconsistências nos perfis turbulentos na saída do bocal e deficiências na previsão de ruído em baixos ângulos e números de Strouhal (St). Optou-se então pelo uso de resultados disponíveis e validados de uma Simulação de Grandes Escalas para um jato simples com número de Mach 0.9 e Reynolds 10^6. Somente o modelo LES se mostrou suficientemente acurado para fornecer dados do escoamento requeridos no presente estudo.

O termo fonte simplificado ($T_{xx}(m = 0)$), foi utilizado para prever o campo acústico de jatos isolados e próximo a uma placa plana. Os resultados apresentaram boa concordância com os dados experimentais para o modo axissimétrico em baixos ângulos de radiação e baixos números de Strouhal. Já no caso de altos ângulos, a previsão dos níveis experimentais foi prejudicada pela ausência dos demais termos do tensor de Lighthill e demais modos azimutais. Considerando a presença de uma placa semi infinita, a parcela considerada do termo fonte se mostrou suficiente para uma previsão muito boa dos níveis experimentais em direções e St nos quais os efeitos de espalhamento no bordo de fuga são dominantes.

Após analisar as principais características do termo fonte proveniente da simulação, os dados foram utilizados para ajustar um modelo de fonte simples, de seis parâmetros, com estrutura no plano x-r. O campo acústico correspondente foi obtido. Notaram-se desvios consideráveis na previsão da diretividade do jato isolado em relação ao experimento e aos resultados do LES. Entretanto, razoável concordância com os dados de referência foi obtida com a presença da placa. Grandes diferenças foram observadas entre resultados de densidade espectral cruzada do termo fonte da simulação LES e do modelo, possivelmente

provenientes de erros das funções simplificadas usadas no ajuste dos parâmetros do último. Essas disparidades no campo da fonte foram tomadas como o principal motivo para as deficiências na previsão do campo sonoro. Apesar desses erros, os efeitos de ruído do bordo de fuga da placa foram bem capturados para $St = 0.3$. Além disso, avaliou-se a sensibilidade do campo acústico em relação à modelagem do decaimento de coerência. Os casos com a presença da placa se mostraram muito menos sensíveis a esse parâmetro do que no caso do jato isolado.

Frente a elevada sensibilidade do jato isolado a erros nos parâmetros do modelo, avaliou-se também uma fonte unidimensional com cinco parâmetros, sem componente radial, envolvendo maior facilidade nos ajustes. Esta foi ajustada com os dados LES integrados radialmente, o que levou melhorias consideráveis na previsão do ruído de jato isolado em baixo número de Strouhal. Os desvios aumentaram com St e ainda aparentaram ser devido a erros nos ajustes dos parâmetros e a limitação das funções utilizadas no modelo. Com relação aos casos com a presença da placa, resultados com a fonte unidimensional apresentaram muito boa concordância com os dados experimentais para os números de Strouhal analisados.

Considerações Finais

No geral, o trabalho utilizou-se de resultados numéricos de campo fluido dinâmico provenientes de uma simulação para o ajuste de parâmetros dos modelos de pacotes de onda. O uso de dados numéricos, concretos, complementa os resultados dos demais estudos na literatura que obtiveram os ajustes através por meio do campo acústico. As limitações do modelo e as consequências da falta de precisão no ajuste destes parâmetros foram analisadas com profundidade. Tanto o processamento dos campo de velocidade da simulação quanto a avaliação dos modelos, também trouxe na medida do possível, uma contribuição para o maior entendimento físico do fenômeno da interação jato-placa. A modelagem do jato isolado se mostrou delicada, não só pela necessidade de consideração de mais termos do tensor de Lighthill e mais modos azimutais, mas também pela alta sensibilidade dos resultados a erros nos parâmetros da fonte e na modelagem do decaimento de coerência. Em uma avaliação geral, a modelagem para previsão de ruído de jatos instalados se mostrou muito mais

simples, com resultados muito menos sensíveis a variações nas características da fonte.

Palavras-chave: Ruido de jato, interação jato-placa, pacotes de onda.

ABSTRACT

The jet flow from engine exhaust is one of the main noise sources in aircraft. Moreover, the effects of engine integration with airframe further intensify noise levels compared to the isolated jet and it is becoming increasingly important in new projects. Wavepackets are structures with important contributions to jet noise, as well as to the noise from the jet interaction with the trailing edge. The wavepacket modeling for installed jet noise prediction was analyzed using simplified geometries. Model parameters were adjusted by means of flow-field data from numerical simulations. Therefore, the accuracy of simulation models based on the Lattice Boltzmann Method (LBM) and Large-eddy Simulation (LES) of the Navier-Stokes equations was analyzed. Only the LES results were considered sufficiently accurate for providing the required flow data for the present study. From the Lighthill's equation, a simplified source term was extracted from the LES data, considering only the axisymmetric mode and the first term of the tensor. The corresponding acoustic field was obtained by a two-point statistics approach, using the free-field Green's function for the isolated jet and a tailored function for a semi-infinite plate for the installed jet. Even with the simplifications, it was possible to predict the main characteristics of the acoustic field of both free jets and from jets positioned under flat plates. A volume wavepacket source model was adjusted based on the LES source term. Significant deviations from the experiments were observed in the prediction of the free-jet directivity. Nevertheless, good agreement with the experimental data could be achieved with presence of the plate. Large disparities were also observed between the cross spectral densities of the LES and source model, which possibly came from the use of a simplified function in the model parameter fitting. Even with such errors, the trailing-edge scattering effects were reasonably captured. Furthermore, the sensitivity of the sound field to the coherence decay modeling was assessed. The jet-plate cases were much less sensitive to this parameter than the isolated jet. Due to the high sensitivity of the free jet to errors in the model parameters, an one-dimensional source model was also analyzed, involving greater ease in the adjustments. This source model was adjusted with the use of a radially integrated LES data and led to improvements on the noise prediction of the free jet at low Strouhal number. In general, the modeling for installed jets

was shown to be much simpler, with results much less sensitive to variations on the source characteristics.

Keywords: jet noise, jet-plate interaction, wavepackets.

LIST OF FIGURES

LIST OF TABLES

LIST OF SYMBOLS AND ABBREVIATIONS

Roman

A	Maximum PSD amplitude
c	Speed of sound
c_0	Ambient speed of sound
C_i	BGK collision operator
C_μ	Turbulence model constant
C_s	Lattice sound-speed
c_v	Specific heat at constant volume
D	Nozzle exit diameter
f	Particle distribution function
F_i	Equilibrium distribution function
G	Green's function
G_0	Free-field Green's function
G_t	Tailored Green's function
h	Distance to the wall
k	Acoustic wavenumber
k_h	Hydrodynamic wavenumber
St	Strouhal number
k_t	Turbulent kinetic energy
L	Gaussian characteristic length
L_c	Gaussian characteristic length of coherence decay
L_m	Modified length scale
M	Jet acoustic Mach number

m	Azimuthal Fourier mode number
M_j	Local Mach number at the nozzle exit
N_x, N_r	Number of points in a certain direction
N_{blocks}	Number of fft blocks
$Nfft$	Number of points per block
p	Pressure fluctuation
R	Distance between source point and observer
r	Radial distance from the jet centerline
Re	Reynolds number
R'	Distance between image source point and observer
S	Source term
s	Entropy
Sf	Window scaling factor
T	Fluid temperature
t	Time
T_{ij}	Lighthill's tensor
T_l	Lattice temperature
t_{sim}	Total simulation time
T_w	Width of window in time
U	Velocity magnitude
u	Velocity fluctuation
U_c	Phase velocity
U_J	Maximum velocity at the jet centerline
$\overline{U}$	Mean velocity
$\mathbf{U}$	Velocity vector
w_i	Weight factors

w Window function

$\mathbf{x}$, $\mathbf{y}$, $\mathbf{z}$ Position vectors

X_c Maximum position of the Gaussian profile

x, r, ϕ Components of the position vector in cylindrical coordinates

x, y, z Components of the position vector in Cartesian coordinates

Greek

q_α Heat flux

ϵ Turbulence dissipation rate

$\tilde{\eta}$ Closure Function

γ Ratio of specific heats

ω Angular frequency

μ Dynamic viscosity

ν Kinematic viscosity

Ω Collision operator

Φ Viscous dissipation function

ϕ Azimuthal angle

ρ Fluid density

ρ_0 Mean ambient density value

τ Relaxation time scale

τ_{eff} Effective relaxation time scale

θ Polar angle

δ_{ij} Kronecker delta

ξ Particle velocity

Subscript

dim Dimensional quantity

dom Dimension of the domain

i Index for the discretized velocity space

i, j Tensor and vector indexes / Indexes of points in the discretized space

l Relative to the line source

n Index if the fft subsample

obs Coordinate of the observer point

rms Root-mean square value

$plate$ Position of the plate's trailing edge

ref Reference value

s Relative to the source field

x, y, z, r Property relative to a specific direction

Abbreviations and Acronyms

AVC Azimuthally Varying Chevrons

BPR By-Pass Ratio

CAA Computational Aeroacoustics

CAEP Committee on Aviation and Environmental Protection

CFD Computational Fluid Dynamics

DNL Day-Night Average Sound Level

DNS Direct Numerical Simulation

EPNdB Effective Perceived Noise level

FFT Fast Fourier Transform

FWH Ffowcs-Williams and Hawkings method

ICAO International Civil Aviation Organization

JFI Jet-Flap Interaction

LBE Lattice Boltzmann Equation

LBM Lattice Boltzmann Method

LES Large-Eddy Simulation of the Navier-Stokes Equation

LSAF Boeing Low Speed Aeroacoustics Facility

LST Linear Stability Theory

NASA National Aeronautics and Space Administration

NS Navier-Stokes

OASPL Overall Sound Pressure Level

PAA Propulsion Airframe Aeroacoustics

PIV Particle Image Velocimetry

POD Proper Orthogonal Decomposition

PSD Power Spectral Density

PSE Parabolized Stability Equations

RANS Reynolds Averaged Navier-Stokes

SPL Sound Pressure Level

TKE Turbulent Kinetic Energy

VLES Very Large-Eddy Simulation

CONTENTS

1 INTRODUCTION

Noise can be understood as the negative aspect of acoustics. It is frequently related to environmental pollution and has numerous effects on human health and work environment (HÜTTL, 2007). According to Nelson (1987), noise induces several physiological reactions such as increases in blood pressure, heart rate, and breathing. Additionally, according to the Committee on Environmental Health (1997), exposure to excessive noise during pregnancy may result in high-frequency hearing loss in newborns and may be associated with prematurity and intrauterine growth retardation.

Unwanted sounds influence many issues in human life like sleep, performance at work and mood. Regarding sleep, noise can affect it in many ways, such as shortening its period, increasing the frequency of awakenings and modifying the duration of its stages. Moreover, exposure to noise can also affect child learning. Research pointed out that children chronically exposed to aircraft noise develop deficits in reading and speech acquisition (HÜTTL, 2007).

Aircraft noise is dominant for residents near airports when planes fly at low altitudes such as during take off and landing (HÜTTL, 2007). Not only engines, but aerodynamic noise from structures - e. g. wings, high-lift devices, landing gear - have considerable contribution on noise emission. According to ICAO (2010), even though aircraft noise emissions today are 75% lower than of those of 50 years ago, it is still the main cause of adverse community reaction to the operation of airports.

Figure 1.1 presents the progress of aircraft certification levels, represented by the chapters in Annex 16 of ICAO (ICAO, 2008), and the evolution of aircraft engines[1]. Chapter 4 is currently applicable, however, the Committee on Aviation and Environmental Protection (CAEP) recommended increasing the stringency of $7EPNdB$[2] to the current regulation. This new standard is to be applied on aircraft submitted for certification on or after December 31, 2017 (ICAO, 2013).

---

[1] Evolution of turbofan engines in respect to the By-pass Ratio (BPR) which is the ratio between mass flow from the fan and from the primary jet.

[2] The Effective Perceived Noise Level (EPNdB) is a measure of human annoyance to aircraft noise which considers human response to spectra shape, intensity, tonal content and duration of noise (ICAO, 2010).

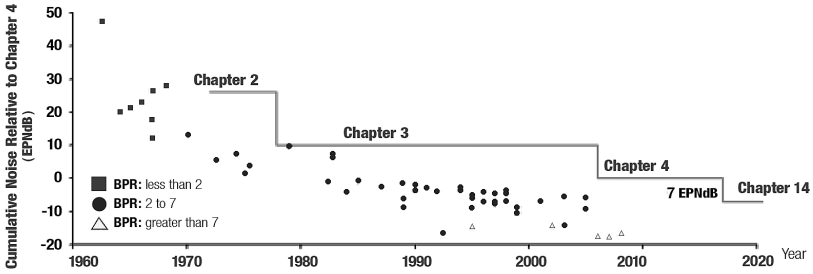

Figure 1.1 – Aircraft noise trends and regulations. Adapted from ICAO (2010).

More concern is directed to the expected growth of airport services. In the near future, the number of commercial flights is expected to continue increasing, and this obviously brings benefits to people and to economy all over the world. However, it comes at the cost of environmental issues, such as noise and pollutant emissions (ICAO, 2013). Moreover, requirements of larger aircraft fleet and airport capacity are expected. ICAO (2013) predicted an average annual growth rate of 4.9% in passenger traffic between 2010 and 2030 and of 4% between 2040 and 2050.

The impact of airport noise on community is often measured by the number of people exposed to it. Figure 1.2 shows the future trends of the population exposed to aircraft noise under four different scenarios of technological and operational improvements. The Day-Night Average Sound Level (DNL) is the metric used to evaluate this exposure, which is an average of the noise level in 24 hours and has a greater weight at night time. Population prone to levels as $55dB\ DNL$ is considered susceptible to significant levels (ICAO, 2010). As one can observe in Figure 1.2, with moderate to high technological advances, the expected growth of the exposed population can be considerably minimized.

The large research effort in the last 50 years has greatly suppressed noise emissions from the jet flow exhausted from engines, especially with the introduction of the turbofan engines in the seventies. The by-pass flux of turbofan creates a dual-stream jet with the primary flux. The higher the By-Pass Ratio (BPR), the lower the noise emissions, whose trend can also be observed in Figure 1.1. Nevertheless, the jet remains one of the main sources of aircraft noise. In the last decades, several investigations have

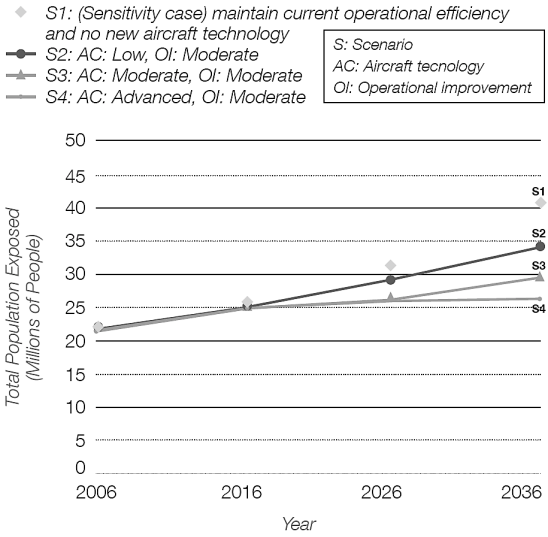

Figure 1.2 – Future trends of population exposed to aircraft noise under four different scenarios of technological and operational advances. From Fleming and Ziegler (2013), ICAO (2013).

been conducted in order to control jet noise using passive noise suppression devices, such as chevron nozzles[3].

Propulsion Airframe Aeroacoustics (PAA) is an area of study concerned with the noise generated by the integration of aero-engines with the structure of the aircraft, such as wings, flaps and pylons. Studies in this area have gained importance with the rise of stricter noise regulations. One of the problems that arises with this integration, also defined as installation effect, is due to the interaction of the jet flow with the wing and high-lift devices such as flaps. In this case, the problem is intensified by the close-coupling between the engine and the wing, required to provide sufficient distance to the ground with the use of large high-by-pass engines (POTT-POLLENSKE, 2011). According to Bondareko *et al.* (2012), this installation problem affects the design of aircraft and the understanding of this interaction helps developing more efficient and more environmental friendly aircraft.

[3] Chevron or serrated nozzles consist of a sawtooth geometry in the nozzle exit which acts modifying the jet turbulent field.

Although many studies have been carried out in this area, the phenomenon is still not completely understood and needs further investigation. The cost of the experimental apparatus and its limitation on characterizing the entire jet turbulent plume, lead to the use of numerical simulations as a complement to experiments in jet noise generation studies (HABIBI *et al.*, 2011). According to Lew *et al.* (2010), computational methods have been an essential tool in recent jet noise assessments. In the case of installed jets, a detailed experimental analysis can be quite expensive, thus evidencing the importance of computational tools in this case. In this sense, there is a demand for simple and low-cost prediction models that would allow the analysis of a significant number of configurations.

1.1 JET NOISE

The complex nature of the sound generation mechanism in turbulent flows makes jet noise one of the most difficult problems in aeroacoustics. Further research effort is required to draw fundamental phenomenological concepts that will help in aircraft design for low jet noise emission and also improve methods for jet noise prediction (UZUN, 2003).

According to Moore (2009), a jet is a stream of fluid that is injected, usually by a nozzle, in a surrounding ambient which can be stationary or with a co-flow.

Jets can be initially laminar or turbulent. When the fluid with higher velocity passes the orifice and emerges into the ambient flow, it creates the so called shear layer, which separates the high speed flow from the external fluid. In an initially laminar jet, the shear-layer exhibits an unstable behaviour and growth of Kelvin-Helmholtz instabilities, which lead to a rapid break-down to turbulence at sufficiently high Reynolds numbers (MATHIEU; SCOTT, 2000). The region involved by the shear layer is called the potential core, in which turbulence levels are still low. In the turbulent region, the jet spreads incorporating the ambient fluid by a process called entrainment and the potential core reduces in diameter. Further downstream of the end of the potential core, the velocity profile eventually reaches a self-similarity condition (MOORE, 2009). Figure 1.3 depicts the main flow regions. The turbulence interaction in different parts of the jet acts as sources of noise.

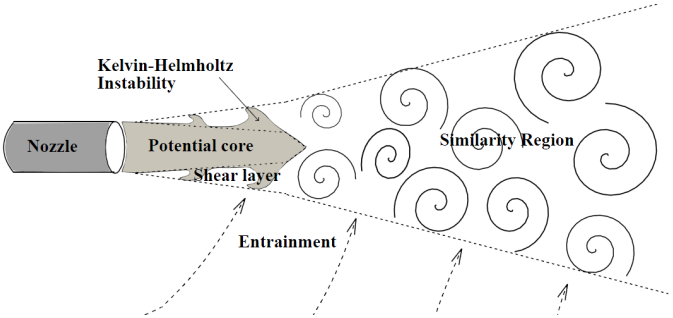

Figure 1.3 – Sketch of the main regions of a single flow jet. Adapted from Moore (2009).

In the development of the jet flow, not all the disturbances are amplified. It is the Reynolds number that qualifies which perturbations and range of frequencies are amplified. Also, although a wide range of pressure fluctuations are present in the flow, only a small portion of them radiate as sound. Pressure fluctuations that do not propagate as sound are defined as *pseudo-sound* (FFOWCS WILIAMS; LIGHTHILL, 1971). Smith (1989) classifies the jet noise into two main components, the shock-associated noise and the mixing noise. In subsonic jet speeds, however, only the latter phenomenon occurs and this work is focused on this situation.

In the fifties, Sir James Lighthill published two papers (LIGHTHILL, 1952; LIGHTHILL, 1954), which presented an acoustic analogy that has become a consolidated jet noise theory. These works marked the beginning of studies on jet noise and also of the aeroacoustics research field. Lighthill rearranged the momentum and continuity equations in the form of an inhomogeneous wave equation, in which the source term accounted for the non-linearities of the Navier-Stokes equation. This source term is interpreted as a volume distribution of acoustic quadrupoles. Also, one valuable conclusion of his research is that jet mixing noise scales with the eighth power of the exhaust velocity, a fact which instigated the *turbofan revolution* in the seventies. Nevertheless, deviations of this behavior occur in aft directivity angles and high Mach numbers. Several improvements to this theory, e. g. source convection and refraction effects, were applied by many authors and are summarized in Tam (1998).

The acoustic analogy proposed by Lighthill (1952) and Lighthill (1954), however, only estimates the sound based on the given information in the flow field. Thus, it is not designed to deeply investigate the details of sound generation and radiation processes. What in the flow/turbulent field effectively radiates as sound may be the great question in jet noise research.

1.1.1 Noise from coherent structures

About 160 years ago, eight people met after tea to hear the performace of some of the grad trion of Beethoven. In that evening, John Leconte (LECONTE, 1858) noted that the flames of the gas-burners, which presented steadiness before the music, started to respond to the music, especially to the violoncello. He was admired of how perfectly the beats were reproduced on the flame: "A deaf man might have seen the harmony". According to Crow and Champagne (1971) these observations were the beginning of the study of orderly jet fluctuations.

It was only a century later, during the sixties and seventies, that researchers discovered that large organized coherent structures could play a role in jet noise (MOLLO-CHRISTENSEN, 1967). This idea triggered several studies in this area, including linear instability approaches, that led to studies of the role of instability waves in jet mixing noise, also referred to as wavepackets. Several experimental and theoretical studies highlighted the importance of such structures in jet noise. These studies began with the observations from Mollo-Christensen (1967), that near-field pressure measurements reveal significant correlation levels in distances larger than one jet diameter. Moreover, a visualization technique by Crow and Champagne (1971) helped in the identification of these organized structures in the jet flow (Figure 1.4). The authors identified a series of consecutive structures ("puffs") which were formed in an intermittent manner in a forced jet.

Many subsequent studies (MICHALKE; FUCHS, 1975; ARMSTRONG *et al.*, 1977; MOORE, 1977) confirmed the existence of such coherent structures by observing both the near and far fields. However the connection between the fluid motions and the sound field is still the motivation of the research with coherent structures. Other authors also evidenced that some of the characteristics of the far-field sound are consistent with organized flow structures (CROW, 1972; CRIGHTON; HUERRE, 1990;

MICHALKE, 1970; MICHALKE; FUCHS, 1975), e.g. the superdirectivity towards low angles, the different spectral shape at these positions and the intermittency of the noise. Many source models, built in the frame work of stochastic and uncorrelated turbulence, used along with Lighthill's analogy, failed to predict these features. This possibly means that they are not representative of the main physical phenomena (CAVALIERI *et al.*, 2011b).

An efficient source model should be able to physically reproduce the main features of the flow field that effectively propagates as sound. Indeed, this is far from being an easy task, due to the complexity of the turbulent jets. However, the evidences of the organized motions beneath the much more complex turbulent field appears as very good choice towards a simple and physically consistent prediction model. In this sense, the effort in the present work is focused on the analysis of coherent structures/wavepacket modeling.

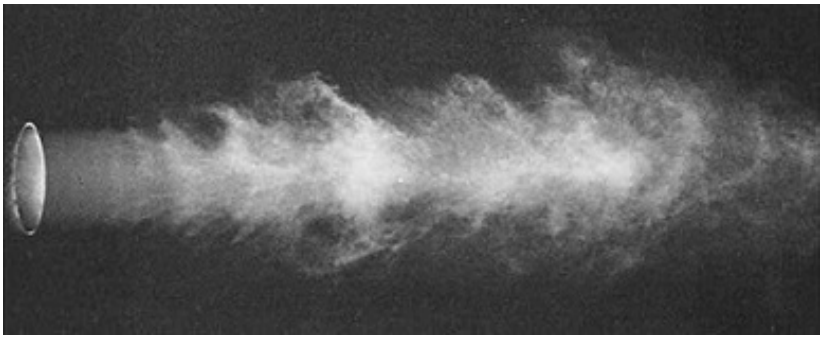

Figure 1.4 – Instantaneous image with CO_2 in low Mach number. Reproduced from Crow and Champagne (1971).

1.2 INSTALLATION NOISE

Adverse effects arising from the presence of solid surfaces near turbulent regions have been known for decades. Curle (1955) presented an extension of Lighthill's theory in order to account for the influence of solid boundaries on the acoustic field. In addition to the quadrupoles, the surface pressure leads to the appearance of dipole sources, which have stronger far-field contribution. Furthermore, Ffowcs Williams and Hall (1970) studied the case

when there are bodies with sharp edges in the flow. In this case, the deduced edge scattering source is even more efficient than both Lighthill's quadrupoles and Curle's compact dipoles.

It is well known that the coupling of engines with aircraft structures such as wing and fuselage can lead to significant modification of the flow and noise generation compared to the isolated jet. Acoustic propagation effects arise from reflection, scattering, refraction and shielding of jet noise from solid airframe surfaces. Moreover, modifications on the jet flow development, like the presence of the pylon and deflection of flaps, leads to the creation or modification of sources if compared to the isolated jet.

Installation effects manifest in different manners depending on the aircraft configuration, i. e. under- or over-the-wing mounted engines or even tail-mounted engines. Figure 1.5 shows the EMB170 airliner (EMBRAER, 2014). It can be inferred, observing the engine position, that jet flow and radiated noise are subjected to interactions with several different airframe surfaces with reflective, refractive or shielding characteristics.

The main effects of under-the-wing configurations are presented in Figure 1.6. Besides the flow interaction with the pylon structure, such configurations may present effects of jet-wing and -flap interaction. In this case, the wing structure plays an important role, augmenting considerably the low frequency noise. Further increase in noise levels ensues when flaps are deflected.

These PAA effects have grown in importance with the increasing strictness of noise regulations. In addition, the rise in engine diameters led to engines closer to the wing, so minimization of the installation noise should be considered in aircraft design. However, due to its complexity, the phenomenon of noise generation is not completely understood. Thus, more efforts should be applied in order to understand PAA effects and also to develop prediction tools that will aid in the design of low noise aircraft.

Figure 1.5 – EMBRAER EMB170 airliner showing the engine mounting under the wing (EMBRAER, 2014).

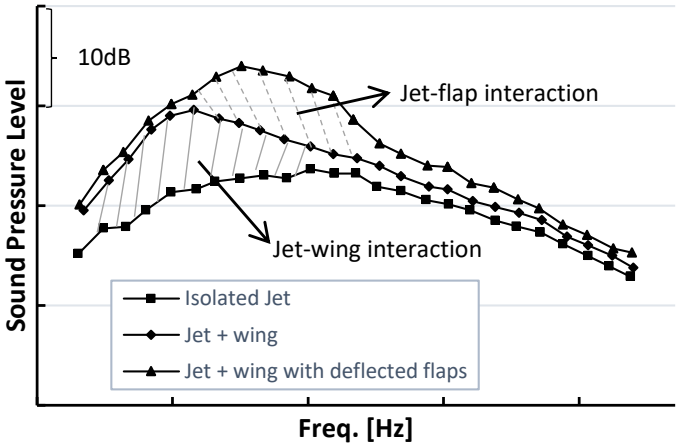

Figure 1.6 – Main installation effects occurring in under-the-wing mounted engines. Adapted from Smith (1989).

1.3 COMPUTATIONAL AEROACOUSTICS (CAA)

When dealing with aeroacoustic problems through computational tools, several approaches can be considered. The so called direct methods perform the noise computation in the same domain as the flow field, without any modeling for the sound. The full set of equations, Navier-Stokes or Euler, is solved in the domain of interest for both the flow and acoustic fields. This requires a domain sufficiently large in order to calculate noise propagation up to the receptor points. Moreover, especially at low Mach numbers, the flow and acoustic fields represent a multi-scale problem. Hereupon, the numerical method should prevent that small acoustic perturbations are influenced by numerical errors of the much larger aerodynamic fluctuations[4]. The combination of these factors requires extremely high spatio-temporal resolution. Furthermore, even if the necessary computer power were available, the discretization schemes used in traditional CFD present intolerable dispersion and dissipation errors, which causes wave damping and distortion (KESSLER, 2007).

Due to the difficulties of using direct methods, the so called hybrid approaches are promising. In these approaches, sound-generation due to aerodynamics is treated separately from the acoustic propagation process. Therefore, sound sources must be considered either by numerically solving the transient flow field or by using semi-empirical source models. When the former approach is used, the requirements for both the fluid dynamics and acoustic regions must be kept just up to the coupling region between the source and acoustic domains, greatly minimizing the costs relative to direct computation. On the other hand, semi-empirical source modeling emerges as a much simpler and faster alternative, where empirical relations, which can be based on mean flow turbulent quantities, model the source behavior. Nevertheless, this approach usually presents a great dependence on calibration constants and is usually very specific.

The ensuing acoustic propagation step can be done both computationally or analytically. In the first approach, an acoustic solver is used in a specific domain, in which assumptions, approximations and schemes are chosen to obtain accurate solutions. In the second, analytical approach, acoustic analogies

[4] The ratio between sound and flow energy is of the order of $10^{-4}M^5$ (KESSLER, 2007).

are used and the sound field is calculated by integration of source terms (KESSLER, 2007). The acoustic analogies of Lighthill (1952) and Ffowcs Williams and Hawkings (1969) are commonly used. For jet aeroacoustics problems, surface integral methods like the Ffowcs-Williams and Hawkings (FWH) surface method, described in di Francescantonio (1997), are broadly used. In this case, far-field noise is obtained by integrating the source term in an arbitrary shaped permeable surface included in the domain of the flow field computation.

Figure 1.7 summarizes the main CAA approaches previously described. The following section describes numerical methods commonly used for calculation of the flow field in aeroacoustics simulations.

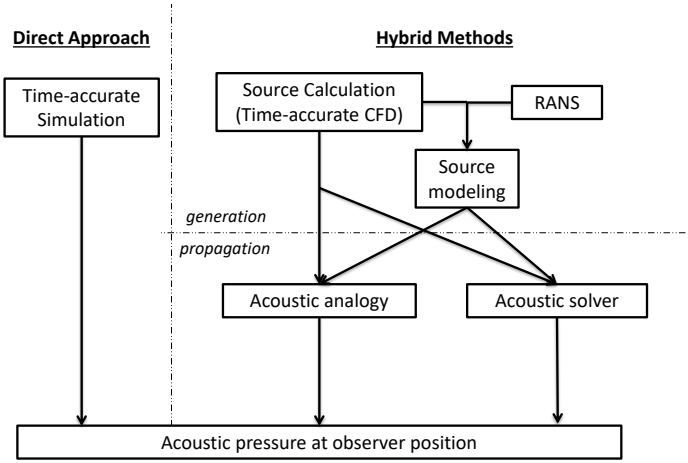

Figure 1.7 – Summary of main CAA approaches.

1.3.1 Traditional CFD methods for source computation

The numerical solution of the Navier-Stokes (NS) equation is the main approach for simulation of turbulent flows. Direct Numerical Simulation (DNS) consists of the resolution of the full NS equation, without any turbulence modeling. To reach this goal, the grid spacing and time step should account for the dynamics of the finest turbulent scales. Indeed, for high Re, the computational cost of such approach is unacceptable and thus DNS is nowadays almost only used for fundamental analyses (SAGAUT, 2007).

In order to minimize computational cost, averaging or filtering procedures are applied to the equations in order to select which range of turbulent scales will be solved and which range will be modeled. Reynolds Averaged Navier-Stokes (RANS) simulations apply a statistical average to the equations, yielding the simulation of the mean turbulent flow. In this way, no turbulent scales are resolved, and their contribution is considered by the use of turbulence models. As it is not suitable for solving instantaneous turbulence, synthetic turbulence techniques and/or semi-empirical approaches are required for noise source modeling.

One the other hand, Large-Eddy Simulation (LES) resolves the large turbulent scales and models the smaller ones. This approach significantly reduces the simulation cost compared to DNS, making it more feasible for complex flows. The use of LES for sound predictions is also justified by the fact that larger scales are more efficient than small ones as sound sources (LABBÉ *et al.*, 2013). This method has been an important tool in recent jet noise studies (BRÈS *et al.*, 2015). However, it still requires high computational effort in high Reynolds numbers, due to the disparities of wall turbulent scales and jet structures. In order to minimize the computational costs, hybrid RANS/LES (XIA *et al.*, 2012; LYUBIMOV, 2013) and wall-modeled LES (BRÈS *et al.*, 2015) approaches have been used by some authors.

1.3.2 Lattice Boltzmann Method approach

An alternative approach to the ones which solve the Navier-Stokes equation, is the Lattice Boltzmann Method (LBM), which is based on the kinetic theory. In this method, the quantity solved is the particle distribution function f, which represents the probability to find, in the elementary volume $d\mathbf{x}$ around $\mathbf{x}$ and in the time interval $(t, t + dt)$, a number of fluid particles with velocity in the interval $(\xi, \xi + d\xi)$ (CASALINO *et al.*, 2014a). The particle distribution function is governed by the Boltzmann Equation:

$$\frac{\partial f}{\partial t} + \xi \frac{\partial f}{\partial \mathbf{x}} = \Omega(f) \tag{1.1}$$

where $\Omega(f)$ is the collision operator. It is frequently modeled by the simple BGK collision model (BHATNAGAR *et al.*, 1954; QIAN *et al.*, 1992), which is actually a relaxation to the

equilibrium Maxwell-Boltzmann distribution. It was shown by He and Luo (1997) that a discrete form of Eq. 1.1, known as the lattice Boltzmann equation (LBE), can be directly derived from the continuous Boltzmann equation.

The macroscopic properties, such as density and velocity, can be obtained by the moments of the distribution function (HABIBI *et al.*, 2011). By using the Chapmann-Enskog expansion, it can be demonstrated that the LBE recovers the NS equations. The accuracy of this recovery is linked to the models used for the velocity space discretization. For instance, using BGK with the well-known D3Q19 discrete velocity model, the NS equation can be recovered for isothermal flow with low compressibility. This also limits the application of LBM to low Mach number cases. More complex models for thermal and higher Mach number flows can be found in the literature (HEGELE, 2010; PHILIPPI *et al.*, 2006; PHILIPPI *et al.*, 2007).

Habibi *et al.* (2011) point out several advantages of the LBM over the Navier-Stokes equation based methods. The absence of Jacobians to compute the grid metrics and the use of particle-based models for solid-fluid boundaries, make it suitable for handling complex geometries like chevron nozzles or even installed jets. Moreover, the method is intrinsically parallelizable, as the convection operator is linear while the non-linear features are recovered by collision/ advection relations. The objective here is not to provide complete description on the LBM. Further information can be found in Succi (2001), Qian *et al.* (1992) and He and Luo (1997).

The use of the LBM in jet aeroacoustics studies has shown a recent growth (LEW *et al.*, 2010; HABIBI *et al.*, 2011; BRÈS *et al.*, 2009). In some of these cited studies, the so called Very Large Eddy Simulation (VLES) approach is used with an eddy-viscosity turbulence model to account for the subgrid scales[5]. More details about the LBM code used in this study are given in Chapter 4.

[5] Although the use of LBM for jet flow can be also considered a large-eddy simulation, the term LES in this work refers to the numerical solution of the Navier-Stokes equation.

1.4 OBJECTIVE

The objective of this study is to analyze wavepacket source models, adjusted with numerical flow data, for the prediction of jet-plate interaction noise.

The specific goals involve:

- Investigation of simplifications on the Lighthill's source term and their relevance to the total sound field;
- Adjustment of a simplified wavepacket model source with flow field data from numerical simulations;
- Analysis of the importance of accuracy in the source adjustment procedure and of the adequacy of simple functions used in the modeling;
- Assessment of the effects of the coherence decay in such models for a jet-plate configuration.

1.5 DOCUMENT OUTLINE

This document is composed of six chapters. Chapter 2 consists of the literature review about numerical and experimental works in jet-wing and jet-flap interaction, with special attention to studies regarding wavepackets and their modeling. Chapter 3 presents the methods, the main considered hypothesis and derivation of the used equations. Chapter 4 consists of an analysis of the prediction capabilities of LBM and the justificative for choosing a numerical database for the remaining analyses. Chapter 5 presents the simplifications of the source term obtained from the high fidelity simulation, and the impact of such simplifications on the noise field. Chapter 6 is concerned with the modeling of the source field by a simple wavepacket source an its sensitivity to coherence decay modeling. Finally, Chapter 7 presents the main conclusions.

2 LITERATURE REVIEW

2.1 CAA FOR JET NOISE PREDICTION

2.1.1 Recent advances in LES for jet noise prediction

Large Eddy Simulation has been applied to the study of turbulent flows since the milestone works of Smagorinsky (1963) and Deardorff (1970). Since then, LES methods passed through a series of numerical developments and were applied to several jet aeroacoustics cases (BOGEY *et al.*, 2003; UZUN, 2003; UZUN *et al.*, 2005; BOGEY; BAILLY, 2006; MOORE, 2009). Due to the increase in computational power and advances in numerical methods, LES is becoming a feasible method for studying the phenomena of noise generation in both installed and isolated jets. Therefore, some recent developments on jet noise prediction using LES are described herein.

Advancements of the use of unstructured meshes with complex geometries in LES are highlighted by the use of the solver CharLES. Khalighi *et al.* (2011) presented a series of jet validation cases, including a dual stream and a supersonic impinging jet. Results for a single flow jet ($M = 1.4$) were in good agreement with experimental data. In the case of the dual stream jet, the flow showed a non-physical separation from the nozzle due to errors in boundary layer assumptions.

Brès *et al.* (2012) also used CharLES in order to investigate a heated over-expanded supersonic jet from a chevron nozzle. The author included the nozzle geometry and used an adaptive mesh technique. Simulations were conducted for a jet with $Re = 1.3 \times 10^5$, $M = 1.35$ and temperature ratio of 2.53. Results for the near and far-field sound levels were in good agreement with experimental data up to a Strouhal number of 3.

Faranosov *et al.* (2013) investigated an axisymmetric jet using LES in conjunction with the CABARET MILES method. Their study highlights advances in LES numerical schemes and implicit turbulence modeling. The jet case with $Re = 8 \times 10^5$ and $M = 0.75$ took around $24 - 72h$ with $500 - 1000$ cores with the HECToR super-computer. The flow field results showed good agreement with experimental data, considering fourth order correlations. Acoustic results were obtained with reasonable agreement with experimental data up to Strouhal number 5.

Brès *et al.* (2015) used the LES code CharLES in order to simulate the jet flow ($M = 0.9$, $Re = 10^6$) from a round nozzle. The boundary layer was forced by a synthetic turbulence approach, in order to achieve a desirable turbulent profile in the nozzle exit. Results using the forced boundary layer showed very good agreement with experimental nozzle-exit profiles and, as consequence, an impressive agreement with the far-field noise data. The comparison between configurations emphasized the importance of a good prediction of the boundary layer turbulent profiles.

Recent advances, mainly in code parallelization, hybrid methods and unstructured meshes, are enhancing LES as a numerical tool to predict jet noise. The development of this approach mostly involves cases with high Mach numbers and relatively low Reynolds numbers. Although this method still presents high computational costs, the very good agreement with experimental data such as the obtained by Brès *et al.* (2015) make these high fidelity simulations suitable for investigating the phenomena of jet noise. The use of LES to investigate installation effects is clearly a tendency and appears as a very promising tool for future studies.

2.1.2 Use of LBM for jet-noise investigation

An alternative to the high cost LES is based in the VLES (Very Large Eddy Simulation) approach combined with the numerical capabilities of the Lattice Boltzmann Method. This combination was successfully applied in automotive and aeronautical applications with high Reynolds flows (BRÈS *et al.*, 2009). The VLES is based on eddy viscosity models to account for the subgrid turbulent scales, mainly modeling the inertial and dissipative ranges. Under these conditions, the required mesh is not so restrictive as in LES, which is computationally advantageous. The use of LBM as a CAA tool was then investigated.

The acoustic prediction capabilities of a LBM based code have been assessed by means of simple benchmark problems by Crouse *et al.* (2006) (one-dimensional plane wave, two-dimensional cylindrical wave, standing wave tube and Helmholtz resonator) and Brès *et al.* (2009) (planar wave and planar Gaussian pulse). In general, the results showed good agreement with analytic and experimental data, with low numerical dispersion and dissipation. Brès *et al.* (2009)

also found that the phase speed of the sound wave is essentially unaffected by the turbulence modeling, and that the method retains their low dispersive properties.

Some jet noise studies were recently conducted for low Mach and Reynolds numbers. Most of them did not use turbulence modeling. Lew *et al.* (2010) assessed a $M_j = 0.4$, $Re = 6000$ turbulent axisymmetric single flow jet. Mean flow, turbulence statistics and acoustic results showed good agreement with experimental data and with LES results. One problem found by the author were spurious tones created in the mesh refinement transition regions. However, these tones did not have a strong influence on the final results. Lew *et al.* (2013) carried out a numerical study of a $M = 0.5$ and $Re = 10^5$ jet with microjets[1]. The runtime was around one week using 128 processors in a Dell Xeon cluster. Simulations were conducted with and without microjets. Overall results showed trends similar to the ones observed in experimental studies.

The investigation of heated jets was addressed by Habibi *et al.* (2011) with $Re = 6000$, using energy transport equations, which were solved with a second-order finite difference scheme. Isothermal jets had $M_j = 0.5$ while heated cases could only reach $M_j = 0.2$ due to code limitations. Flow-field statistics showed similar results to those found in the literature. The directivity trend on OASPL results were consistent with experimental data, except for the higher temperature ratio.

While previous works used no turbulence modeling, Habibi *et al.* (2013) conducted LBM simulations of the flow through an internal mixing nozzle with lobed mixers using turbulence modeling. Heat transfer was considered as in Habibi *et al.* (2011). Analyses were conducted with $Re = 1.36 \times 10^6$ and $M = 0.5$. The RNG k-ϵ model was used for modeling sub-grid scales and the FWH method with permeable surface was used to obtain the far-field noise. According to the authors, the results were consistent with the trends shown in NASA tests for the same nozzles with lobed mixers. This analysis was further extended in Habibi *et al.* (2014), by using an entropic Lattice Boltzmann scheme, which allowed higher Mach number ($M_j = 0.83$) and temperature ratio (2.37).

[1] Microjets are noise suppression devices where fluid is injected on the main jet shear layer by an circumferential array of smaller jets.

Other results using this high subsonic Mach approach were obtained for single flow jets heated $M = 0.9$ (LEW *et al.*, 2014; GOPALAKRISHNAN *et al.*, 2016) and a coaxial Mach 0.9 jet (CASALINO; LELE, 2014). In general reasonable agreement with experimental data was obtained, with more deficiencies in predicting the noise at low angles.

The methodologies implemented within the LBM based code PowerFLOW were shown to have the capabilities for solving aeroacoustic problems. Recent development increased the range of Mach numbers and temperature ratios that can be used in the simulations. Although results were not as accurate as the most recent LES results, the low computational cost is very attractive. The automatic generation of the Cartesian mesh and the parallelization capabilities make the use of this commercial code suitable for noise predictions in complex geometries on both isolated and installed jets. The limitations of using this implementation for jet noise prediction are further commented in Chapter 4.

2.2 JET NOISE, COHERENT STRUCTURES AND WAVEPACKETS

Mollo-Christensen (1963), Mollo-Christensen (1967) suggested that the turbulence could be less irregular than was thought before. By the end of the sixties and in the seventies, several authors identified the characteristics of more organized, coherent structures in the far field, acoustic near field and flow field of jets. However, much discussion was still present regarding the relevance of such structures for the sound field of subsonic and high Reynolds jets. Due to the limitations of early experiments, the connections between what was observed at the far field and near field was not clear. The developments in more recent experimental studies and numerical simulations are tending to confirm the importance of such structures for jet noise (JORDAN; COLONIUS, 2013). The debate and investigation of the role of large, coherent structures remain up to this date, however much has evolved since the end of the seventies and the main conclusions and remaining questions are presented herein.

The idea behind the generation of the sound field purely by stochastic eddies, and so compact uncorrelated quadrupoles, was called into question by some characteristics of the jet noise field which cannot be attributed to this kind of turbulent flow. The main point that causes uncertainties about these early theories is the jet directivity. It is clear that the flow radiates considerably higher noise to low polar angles. Not only the amplitude is higher, but also the spectral shape presents a rapid spectral decay in this direction, while at higher angles, the sound field is more broad band. Structures like non-compact wavepackets present envelops with more than one oscillation in the axial direction. This leads to axial interference, creating the antenna effect defined by Mollo-Christensen (1967) (JORDAN; COLONIUS, 2013), which justify the jet superdirective characteristics (CRIGHTON; HUERRE, 1990; CAVALIERI *et al.*, 2012). This effect cannot be generated by a field of stochastic eddies as they lack phase synchronization.

Another view of the problem is addressed by Tam *et al.* (1996) and Tam (1998). In this perspective, the sound field is supposed to hold contributions of two source types. These sources are the so called large-scale turbulence, interpreted as instability waves, which are responsible for the Mach wave radiation and the directivity towards low angles, and the fine-scale turbulence, with broad-band sound field, responsible for the radiation to high angles. Two similarity spectra were proposed and fitted well with subsonic and supersonic jet experimental data. However, Jordan and Gervais (2008), Jordan and Colonius (2013) and Kleinman and Freund (2008) state that the physics of the separation between these scales is still unclear, and actually, some propose that the noise at high angles could arise from different behaviors of a wavepacket source.

Mollo-Christensen (1963), Mollo-Christensen (1967) and Mollo-Christensen *et al.* (1964) are landmark studies regarding orderly structures in jets and their relation to the noise field. Mollo-Christensen (1967) measurements of pressure correlations outside a fully turbulent jet indicated the presence of a regular structure in the jet flow. The author proposed with a concept in which the jet acted like a semi-infinite line emitter for sound. By means of flow-visualization experiments, Crow and Champagne (1971) identified an ordely axisymmetric pattern, which was clearly visualized up to $Re = 7 \times 10^4$. The observed train of

"puffs", as defined by the authors, showed a characteristic average frequency of formation equivalent to $St = fD/U = 0.3$. The experiments with a forced jet[2] resulted in axisymmetric waves. The forcing at $St = 0.3$ resulted in the greatest downstream amplification, with its maximum about 4 diameters from the nozzle. For lower St this maximum was reached further downstream and for higher St, more upstream.

Lau *et al.* (1972) performed measurements in the region up to the end of the potential core and suggested the existence of a "relatively periodic and deterministic flow structure". The author observed a regular pattern of an axial array of vortices convected downstream with convection velocity $0.6U_j$. Fuchs (1972) analyzed two-point correlation coefficients of the jet flow field. Strong coherence was found up to 8 diameters from the jet exit. The author found that axial correlation showed a wavepacket structure in both the core and entrainment regions. The author identified this as a semi-deterministic wave-like structure and classified the jet source to be non-compact.

By taking cross correlation measurements with microphones positioned on a sphere at the far field of a subsonic, round jet, Maestrello (1976) observed that the noise at low angles is coherent while for large angles, the sources were incoherent. However, other authors showed that the coherence for high angles was also significant for low St (FUCHS; MICHEL, 1978; CAVALIERI, 2012).

Some experimental analyses explored the decomposition of the noise field. Michalke and Fuchs (1975) evaluated azimuthal cross correlations of pressure and velocity, allowing the decomposition of the data into azimuthal Fourier modes. The low-order modes 0, 1 and 2 were predominant in the pressure field, in spite of the low contribution of the axisymmetric mode ($m = 0$) to the velocity field.

The same conclusions regarding the dominance of the first three modes were found by Armstrong *et al.* (1977), by analyzing the coherence between two microphones in a circle around the jet. The authors also verified that coherent structures persist, but with decaying energy, as the Mach number increases. These observations were even further reinforced by Juvé *et al.* (1979) by taking spatial cross-correlation coefficients from microphones at the far-field for

[2] A jet submitted to specific external perturbations, often periodic in time.

three St numbers. Results suggested the dominance of mode 0 at polar angle 30°, modes 1 and 2 for 60° and mode 2 for 90°. No major changes could be observed by varying St in the analyzed range.

Studies in the area of linear stability appeared as a form to model the coherent structures. This approach is based on the linearization of the Navier-Stokes equations for small perturbations. Although this is valid for laminar regimes, it can be extended based on the average turbulent field and on the concept of separation between instability waves and turbulent eddies. This approach was validated for turbulent flows (ARMSTRONG *et al.*, 1977; CROW; CHAMPAGNE, 1971). Early results of stability analysis using parallel base flows (MICHALKE, 1977) agreed well with the phase speeds of the previously observed coherent structures (CROW; CHAMPAGNE, 1971), however these parallel flow models led to instabilities with unlimited downstream growth.

The application of linear stability models on axisymmetric jets by Crighton and Gaster (1976), considering the slow divergence of the mean flow, showed that instability waves did not present unlimited growth in the flow direction, but rather a saturation and decay. So the instability wave takes the form of a wavepacket, in which the saturation can be associated with the slow spread of the mean flow (GUDMUNDSSON; COLONIUS, 2011; CAVALIERI, 2012)). According to Crow and Champagne (1971) the decay may be also justified by the action of turbulence, which dissipates the instability wave. Another reason could be the increased importance of non-linear effects, which are not considered in the analysis (CROW; CHAMPAGNE, 1971; CAVALIERI, 2012).

More recent near-field pressure measurements have been used as an effective tool for the identification of coherent structures inside the flow field. Picard and Delville (2000) used the Proper Orthogonal Decomposition (POD) for the identification of the dominant modes in the jet along with the technique of Linear Stochastic Estimation (LSE) in order to find the velocity field associated with each mode. The latter enabled a visualization of the advection of large vortical structures.

Panda *et al.* (2005) measured the fluctuating $\rho U_x U_x$ and $\rho U_r U_r$ stress terms, where U_x is the longitudinal and U_r the transversal velocity components, and correlated them with sound pressure fluctuations at several polar angles. The highest correlation levels were found for $\rho U_x U_x$, especially for the first

order fluctuations. A cross-spectral analysis showed that the correlations at low angles were higher in the low St range, which is typical of large coherent structures, according to the authors.

Hall *et al.* (2005) used near-field pressure information with velocity field measurements in order to investigate the role of the large-scale structures in a $M = 0.6$ jet. Results revealed the dominance of mode 0 around the end of the potential core region, while in the shear layer, the modes 1 and 2 showed considerable energy.

The already mentioned evidences of the importance of wavepackets for jet-noise were found in the acoustic near and far field and at the flow field of the isolated jets. More specifically, the near-acoustic field was used by many authors to investigate coherent structures. According to Jordan and Colonius (2013), fluctuations in this region are small enough to permit linearization and also contain non-propagating waves in the form of evanescent waves, with exponentially decaying amplitude with the radial distance. In this region, the pressure fluctuations contain the hydrodynamic signatures of coherent structures, but less affected by the more energetically turbulent motions, present in the non-linear hydrodynamic field. The near-field can be also considered a matching region between the jet flow field and the radiated sound field (JORDAN; COLONIUS, 2013).

With the objective of identifying the presence of an evanescent pressure field associated with instability waves in the jet flow, Suzuki and Colonius (2006) positioned a conical microphone array just outside the mixing layer. A modified beanforming technique was used, substituting the usual monopole source by an eigenfunction obtained from linear stability analysis. The results confirmed the relation between the measured fluctuations with evolving instability waves in the turbulent flow.

The study of Tinney and Jordan (2008) consisted of pressure measurements in the near-field of a heated coaxial jet and showed again the predominance of the low order modes. Their result suggest that these coherent structures persist and are important in high Mach and Reynolds numbers. The findings of a POD analysis indicate a structure with the behavior of an axial wave suffering amplification, saturation and decay (wavepacket).

Viswanathan *et al.* (2010) used space-time correlation between near-field microphones in a cage array and far-field microphones for identifying jet noise sources behavior. Results led to the discovery of a large coherent source which is located between $13D$ to $30D$ in the axial direction. Near-farfield correlation reinforced the presence of this source, whose contribution was significant at low angles. The authors also reinforced the theory that random fine-scale turbulence is responsible for noise radiation in upstream positions. However, these results were questioned by Jordan and Colonius (2013), since the microphones were positioned too far away from the jet and so in the linear acoustic region. That is possibly the reason why such a large source extension was found.

The studies looking at the far-field tend to confirm the consistency of the noise field with a wavepacket source. The directivity towards low angles, with spectra peaking about $St = 0.2$ with narrow spectral content in comparison with the more broad-band spectra of higher angles (JORDAN; COLONIUS, 2013). Some of these characteristcs could be mimicked by the use of simple wavepacket models, which were proposed as an attempt to provide a simple description of jet noise source (CROW, 1972; CRIGHTON, 1975; FFOWCS WILLIAMS; KEMPTON, 1978). The low-angle directivity with exponential decay at high angles, resulting from these models, was defined as superdirectivity (CRIGHTON; HUERRE, 1990; CAVALIERI *et al.*, 2012).

The experimental investigation of Cavalieri *et al.* (2012) aimed at the presence of superdirective wavepacket signatures in the sound field of an unforced subsonic jet. Acoustic experimental data obtained by microphone arrays were decomposed into azimuthal Fourier modes and the focus was on the axisymetric mode as it was shown to dominate the radiation towards low angles (MICHALKE; FUCHS, 1975; JUVÉ *et al.*, 1979). The line source model from (CROW, 1972) (see Crighton (1975)),

$$T_{xx}(x, r, m = 0, \omega) = 2\rho_0 U \hat{\mathrm{u}}_x e^{-ik_h x} e^{-x^2/L^2}, \tag{2.1}$$

was used to provide a theoretical background for the phenomenon, where ρ_0 is the density of the undisturbed fluid, U is the amplitude of the mean velocity and $\hat{\mathrm{u}}_x$ is the amplitude of the axial velocity fluctuation, k_h is the axial wavenumber and L the characteristic length of the wavepacket envelope.

Cavalieri *et al.* (2012) found that the superdirectivity is a function of $k_h L$. This parameter dictates the level of interference that comes from more than one oscillating wavelength in the axially distributed source. The noncompact characteristic of the source leads to axial interference, which causes the radiation to be concentrated at low polar angles. These parameters were obtained by the best fit of the experimental noise data.

The dominance of the axisymmetric mode decreases with decreasing Mach number. Results with increasing St numbers tend to deviate from the superdirective behaviour, a fact which may be caused by refraction effects. Cavalieri *et al.* (2012) found that the source reduces its extension with increasing St number, approaching the compact limit at $St > 0.8$, however the fitting could be biased in this region by the presence of refraction effects. An analysis of the velocity dependence of SPL for different modes showed that the exponent of the velocity scaling is greater for the mode 0 than the other modes at low polar angles, so, at high Mach number, the axisymmetric becomes more dominant over the other modes. For both helical wavepackets (modes 1 and 2), the present azimuthal interferences cause a decrease in the super-directive behaviour.

More comprehensive analyses of the flow field were also addressed, with comparison with results of the linear stability theory. Gudmundsson and Colonius (2011) investigated the limitations of the description of velocity fluctuations in subsonic jets as linear perturbations of a mean flow (Parabolized Stability Equations - PSE). With the aid of data from a microphone array positioned outside the mixing layer of cold and hot $M = 0.5$ and $M = 0.9$ jets, the authors extended the investigation of Suzuki and Colonius (2006) by employing PSE and showing that the results agreed well with PIV measurements and with the characteristics of convecting wavepackets. The authors filtered the signal by applying the Proper Orthogonal Decomposition (POD), with the objective of separating uncorrelated data from instability waves. This procedure allowed much better agreement between the PSE and experiments even downstream of the potential core for both amplitude and phases. The array discretization limited the analysis up to $St = 0.65$. For $m = 0$ and $St < 0.2$ the agreement was not satisfactory. Here, deviations are supposed to be due to the underprediciton of the growth rate of instabilities close to the nozzle exit.

Cavalieri *et al.* (2013) investigated wavepackets in the velocity field of non-forced subsonic jets ($M = 0.4$, 0.5 and 0.6 and Re from 4.2×10^5 to 5.7×10^5). This was done by measuring the flow field and decomposing it into azimuthal Fourier modes with comparison to synchronous measurements of the sound field. Although the far-field noise is dominated by the the axisymmetric mode ($m = 0$), the flow field shows its peaks between $m = 4$ and 11. Moreover, it was not possible to identify azimuthally coherent structures by looking at snapshots of the turbulent velocity field of unforced jets which is dominated by small eddies. Nevertheless, the decomposition of the velocity into azimuthal Fourier modes revealed that only a small part of the flow energy is contained in lower azimuthal modes. At low St numbers, radial compactness can be assumed, and the authors argued that, in this situation, higher azimuthal modes present low acoustic efficiency due to destructive azimuthal interference. Furthermore, significant correlation levels were found between the axissymmetric modes of the velocity field and far-field sound at low directivity angles, despite of the very low amplitude levels of the former. Two-point correlation levels were negligible when the non-decomposed velocity field was considered. Up to the end of the potential core, wavepackets resulting from PSE solutions agreed well with the axisymmetric and first helical modes of the velocity field. This observation supports such modelling for velocity fluctuations.

Both Cavalieri *et al.* (2013) and Gudmundsson and Colonius (2011) found a deficiency in the linear stability approach to predict the growth rate of instability waves for low frequencies, $m = 0$ and in positions close to the nozzle exit.

A further analysis of the poor agreement of the PSE with fluctuations downstream of the potential core was conducted by means of near-field pressure measurements by Breakey *et al.* (2013), with the PSE data being compared with the full $m = 0$ signal and with the first POD mode of the $m = 0$ pressure fluctuations. The agreement between the PSE results and the first POD mode was very good even downstream of the potential core. This analysis suggests the existence of linear wavepackets in this region, which are masked by the presence of high incoherent pressure/velocity fluctuations. The authors also reconstructed the time pressure signals by projecting the POD modes and compared the results with the full signals. Results highlighted the wavepacket structure of the near pressure field. The correlation

between the near-field POD modes and the far-field sound resulted in significant levels, not only for the first mode, but also for other high other POD modes. The authors concluded that only one POD mode was insufficient to represent the acoustically efficient sources. Indeed, the propagation of the PSE and first POD mode results presented noise levels much lower in comparison with the full data. The unit-coherence nature of the approaches is pointed as possible main cause.

2.2.1 Intermittency and coherence decay

One of the main observed features of coherent structures is the interminttency of the generated noise field (MOLLO-CHRISTENSEN, 1967; CROW; CHAMPAGNE, 1971; JUVÉ *et al.*, 1980; GUJ *et al.*, 2003; HILEMAN *et al.*, 2005; TINNEY; JORDAN, 2008). Crow and Champagne (1971), observed an intermittent behavior in the formation of the observed "puffs" in the flow. Juvé *et al.* (1980) showed that 50% of the noise is produced during only 10% to 20% of the time. Freund (2001) could observe these caracteristics in the flow field, while Tinney and Jordan (2008) made these observations in the near-field of a coaxial jet. This phenomena was further explored by numerical simulations and experimental investigations in conjuction with wavelet transforms (CAVALIERI *et al.*, 2011a; KOENIG *et al.*, 2013).

Cavalieri *et al.* (2011a) analyzed LES data of a $M = 0.9$ single-stream jet. Some high, temporally localized levels were found in the acoustic pressure data for the axisymmetric mode, specially for low polar angles, say 30°. Also, the axisymmetric mode radiation was shown to be related with the temporal modulation of wavepacket structures. By observing the hydrodynamic near field, the authors concluded that the axisymmetric part of the flow presents fluctuations in the amplitude as well as in the length of its envelope. This phenomenon was denominated "wavepacket jittering" (CAVALIERI *et al.*, 2011b).

The studies reviewed in the previous section showed that linear stability analysis of the mean flow provides results in good agreement with the main characteristics of the experimental hydrodynamic field. However, the propagation of these models resulted in very low noise levels in subsonic jets. On the other

hand, the agreement was good for supersonic jet flows (SINHA *et al.*, 2014; LÉON; BRAZIER, 2011).

In fact, the linear models provide a kind of average wavepacket structure, while actually, both length and amplitudes vary in time, which enhances the sound radiation. These models lack on the representation of the jittering effect (CAVALIERI *et al.*, 2011b), which is a space-time characteristic of coherent structures related to the observed intermittency in sound generation.

In order to verify if the jitter was the missing piece, several works focused on introducing these characteristics into the modeling. One of the first studies considering such effects was addressed by Ffowcs Williams and Kempton (1978). They introduced jittering in the form of a randomness in the phase velocity and observed an increase of noise levels. Some years later, Cavalieri *et al.* (2011a) introduced the modulation effect observed on LES results in a line wavepacket-source model, which was fed with simulation velocity data. The improved model provided results much closer to the LES data compared to the time-averaged wavepacket model source.

Cavalieri *et al.* (2011b) analyzed more deeply the effects of introducing space-time modulations in simple models. A simple T_{xx} model line source (CROW, 1972) was modified by the introduction of temporal modulations with three approaches. Sound radiation was increased both by introducing amplitude time variations and variable length of envelope, especially for high angles. The third approach used both time varying amplitudes and characteristic length which were adjusted using available simulation data. The results presented deviations of only $1.5dB$ from the LES results (in comparison to $10dB$ for the time-average source) for subsonic jets. By Fourier transforming the source in time and space, it could be observed that jittering spread the spectral content of fluctuating energy into radiating conditions. On the other hand, the modeling of the jittering effect did not seem to be necessary for the noise prediction from convectively supersonic jets.

Jordan *et al.* (2014) employed several linearized wavepacket models in conjunction with LES data in order to analyze the effects of time-variable base flows. In this way, the authors could generate jittering wavepackets which were shown to considerably increase acoustic efficiency, but the noise increase was still not sufficient to reach the LES levels. The authors stated that the approach required

further improvements in order to provide better agreement with the reference data.

Tissot *et al.* (2017) stated that the poor prediction of the hydrodynamic region downstream of the potential core, the unit coherence and the low levels in the farfield resulting from linear stability models are related to the missing jittering, which is related to non-linearities. In their study, these non-linearities were introduced via external forcing and the flow response was analyzed. Such modeling intended to represent the non-linearity that came from the interaction of the wavepackets with turbulence. The effects of the forcing were noted downstream of the potential core, where the linear models presented limitations. The authors showed that the sensitivity to the forcing is higher in the critical layer[3] and reinforced the necessity of correctly accounting for coherence decay for jet noise prediction. Nevertheless more information is still necessary in order to understand how these non-linearities affect the coherence decay.

In order to evaluate the effects of the coherence decay in wavepacket models, Cavalieri and Agarwal (2014) used an integral solution based on two-point statistics of the source term. The idea was to understand the possible causes of the discrepancies between linear models and the expected far-filed results in convectively subsonic jets, by including the effects of jittering in the frequency domain. A model line source was defined by including the effets of coherence decay modeled by a Gaussian envelope with characteristic length L_c. When the sources were Fourier transformed in space, those which accounted for the coherence decay were more spread out in wavenumber space, with a better fullfillment of the radiation condition for subsonic jets[4], which is not accomplished by the unitary coherence source. Not only the coherence affected the levels in lower radiation angles, but also changed the directivity of the far-field noise, specially for the subsonic case. The main conclusion was that the propagation of a wavepacket model matching the average amplitudes and phases is not sufficient to correctly reproduce the sound field. In addition to that, the coherence function of the flow should also be considered. That is the reason why even though linear solutions well matched the average amplitude and phases of the velocity field (SUZUKI; COLONIUS, 2006; CAVALIERI *et al.*, 2013), the propagation of

[3] location where phase speed is equal to the local velocity

[4] $|\omega| \leqslant | \, k_h \, | \, c$ for this case

these sources lead to sound levels orders of magnitude lower than those expected.

Motivated by the findings of Cavalieri and Agarwal (2014), Baqui *et al.* (2015) explored comparisons between the solution of the Linearized Euler Equation (LEE) and linear PSE with experimental data in the St range from 0.3 to 0.7. The results further confirmed the lack of agreement of the models in the near-field downstream of the potential core and showed that the far-field sound was considerably underpredicted. Coherence profiles taken from the experiments were thus imposed in the cross spectral density (CSD) on cylindrical and conical surfaces enclosing the computed near field. The propagation of this modified surface data yielded results much closer to experimental data and reinforced the conclusion about the importance of the coherence decay. An analysis of the CSD surface data revealed that the application of the experimental coherence led to a source more concentrated in space and more spread out in the wavenumber space, thus resulting in a more efficient acoustic source with better fulfillment of the radiation condition.

Jaunet *et al.* (2017) used two independent and synchronized stereo PIV systems in order to obtain experimentally measured two-point statistics of wavepackets in an isothermal jet ($M = 0.4$ and $Re = 4.6 \times 10^5$). The fluctuating velocity data in the plane was decomposed into azimuthal Fourier modes. The contribution of the acoustically efficient modes ($m = 0, 1, 2$) to the total cumulative coherence was less than 10%. The CSD was shown to be dictated by the modes that dominate the fluctuating energy. Therefore, the authors highlighted that only considering the statistics of the whole set of modes may result in misleading conclusions. The coherence data was explored by exponential fits from which a characteristic coherence length (L_c) could be obtained. By observing $St \times x/D$ maps for L_c considering the energy containing eddies (higher order modes), the St of the peak L_c could be identified for each axial position. The peak St reduced when the reference points moved downstream, a trend which was related to the vorticity thickness. For the specific case of the axisymmetric mode, the L_c peaks do not show the same behavior, with values considerably higher in some $x - St$ positions when compared with the maps from all modes. The regions in which the wavepacket L_c differs the most from the value of higher order modes is coincident with the range in which the prediction of linear models are successful.

The studies presented in this section show strong evidences of the dominance of wavepackets on the noise field of turbulent jets. A deeper understanding of the main physical characteristics of the source contributes to the development of simple models for noise prediction.

2.3 ANALYSIS AND MODELING OF SOURCE TERM EXTRACTED FROM LES AND DNS

Even though the acoustic analogy does not carry information regarding the physics of sound generation, it has been used extensively for the prediction of the noise field based on source terms extracted from LES and DNS or modeled semi-empirically. Some authors tried to examine the sound generation by separating the contribution of different terms and/or filtering the source field.

Samanta *et al.* (2006) analyzed the robustness of some acoustic analogies by introducing errors into the source, obtained from a DNS of a two-dimensional mixing layer. These errors were representative of missing small-scale turbulence or errors in the prediction of large turbulent scales. This separation was done by performing an orthogonal decomposition and modifying or taking out the modes relative to each range of scales. Although the considered analogies showed very similar errors when higher modes were taken out, the Lighthill's analogy showed greater errors at low frequencies and high angles when the first POD mode coefficient was divided by 2.

Bastin *et al.* (1997) assessed the contribution of coherent structures with a numerical approach[5], in which only large-scale fluctuations were calculated. Lighthill's analogy was used to compute the sound field for plane jets with $M = 0.5$ and 1.33. Although the coherent structure information seemed to be sufficient for supersonic jet prediction, in the subsonic case, the spectrum contained only the low frequency region ($St < 0.2$).

Important studies were also conducted by splitting the source term into linear and non-linear momentum terms, as well as, entropy terms. This is the case of Freund (2001), who analyzed a DNS of a turbulent jet ($Re = 3600$, $M = 0.9$). The source term based on Lighthill's analogy was Fourier transformed in space and

[5] Called Semi-deterministic modeling (SDM)

time and filtered in order to identify the components that radiate effectively to the far field. The author observed that the spatial position of the peak of the radiating portion of the source is neither coincident with the peak of the full source nor the peak of the turbulent intensity. So, the mean turbulent field may not be well correlated to the radiating source and its use for modeling should be considered with care. Also, the identified sources were found to be non-compact in the axial direction. The peak frequency of the radiation was found to correspond to $St = 0.2$. By applying streamwise wavenumber filters to the source term at this frequency, the author observed a wavepacket form even downstream of the potential core. This specific source modes were propagated, resulting in high directive noise fields (more directive than the prediction using Doppler factors).

Freund (2003) further explored the previous simulation to obtain turbulence statistics, splitting the linear, quadratic and entropy terms of Lighthill's tensor. He found that the entropy term has a cancellation contribution to the linear term at low angles for this isothermal jet. The noncompact characteristics of the source were again observed. The results showed the dominance of the linear term in the low-frequency part of the spectrum at 30°, suffering from cancellation effects due to the entropy term. At 54°, the linear term was still dominant at $St < 0.3$, and had comparable contributions to the non-linear term at higher St. At higher angles, the non-linear term was dominant.

Bodony and Lele (2008) assessed the contribution of the momentum and entropy terms of Lighthill's source obtained by the LES of cold Mach jets ($M = 0.9$ and 2) and hot jets $M = 1$. In the first case, the momentum term resulted in levels about 2dB higher than the total level and about 10 dB higher than the entropy terms at 30° up to $St = 0.3$. Over $St = 0.8$ momentum and entropy terms result in similar magnitudes, but both higher than the total level. These results evidence the presence of cancellation between both terms. At 90° the momentum term is completely dominant. For the other Mach numbers, cancellation effects between the terms were found to be much more substantial.

Lele *et al.* (2010) filtered LES azimuthal decomposed data in the $k_x - \omega$ space in order to separate subsonic and supersonic wave components. POD was also applied and the filtered data was visualized. For the subsonic jet, a large helical wavepacket structure could be identified in the supersonic components of the

jet with $M_j = 0.51$. Azimuthal modes $m = 0$ and $m = 1$ presented dominance of subsonic wave components for the low Mach jet, while the high speed ($M_j = 1.95$) jet presented dominance of the supersonic wave components.

The studies in the literature underline the importance of deeper analyses on the physics of the source term, since acoustic analogies alone do not highlight the main contributions to the jet noise field. Studies like Freund (2001), Freund (2003), Bodony and Lele (2008) have greatly contributed to the comprehension of important terms in the sound generation, providing useful information for simplified models. This aspect of modeling will be analyzed in Chapter 5 of the present study.

2.3.1 Use of model sources with acoustic Analogy

Two-point statistics have been used as base for several models based on Lighthill (1952) expression for the sound power radiation as function of the space-time velocity correlations. Further, the separation of the contribution of turbulence alone (self-noise) and interaction of turbulence with mean flow (shear noise), proposed by Ribner (1969), motivated some of these models. Such models carried the assumption of isotropic and homogeneous turbulence in the modeling of the space-time correlation of the Reynolds stress tensor. More complex versions were also analyzed, including effects of source convection and anisotropy in the modeling, frequency dependent scales, and/or with data extracted from RANS turbulence models (FREUND, 2003; SELF, 2004; KERHERVÉ *et al.*, 2004; KERHERVÉ *et al.*, 2006; JORDAN; GERVAIS, 2005; MORRIS; ZAMAN, 2010; POKORA; MCGUIRK, 2015; ROSA *et al.*, 2016).

Bailly *et al.* (1996), assessed a method to estimate the Mach wave noise based on Ffowcs Williams and Maidanik (1965) who developed an expression relating the acoustic autocorrelation pressure in the farfield to the spacetime pressure correlation in the near field. RANS solutions were used to provide inputs to the approach which is also based on the Lighthill's analogy. The model presented good agreement with experiments for supersonic jets for the directivity and spectral shapes, however, one of its limitation is the use of a specific Green's function for Lighthill's equation.

The present review, however, is focused on methods that explore the physics of coherent structures and use two-point statistics from specific modes, whose differences to the full turbulent data were highlighted by Jaunet *et al.* (2017). The discovery of coherent structures motivated the possiblity of modeling of the jet sources by means of reduced order models (BREAKEY *et al.*, 2013). Simple wave-like line source models have been used with success to predict the noise field characteristics due to coherent structures (MICHALKE, 1970; CROW, 1972; CAVALIERI *et al.*, 2012). These line wavepacket sources were mostly variations of the one proposed by Crow (1972) (see Crighton (1975)). As mentioned in the previous section, the addition of jittering effects into these models has greatly improved the noise prediction (SANDHAM *et al.*, 2006; REBA *et al.*, 2010; CAVALIERI *et al.*, 2011a; CAVALIERI *et al.*, 2011b; CAVALIERI *et al.*, 2012; KERHERVÉ *et al.*, 2012; CAVALIERI; AGARWAL, 2014).

Reba *et al.* (2010) used a simple wavepacket model defined by experimental data of two-point space-time pressure correlations in a surface surrounding the jet flow. The results were in very good agreement with experiments at low angles and low St for the supersonic jets and underpredicted the noise levels for the subsonic cases.

Dynamic source modelling using linear stability theory has been greatly used as well. Although the far-field results present the already mentioned deficiencies due to unit coherence, the addition of coherence decay was shown to enhance the prediction of such models (BAQUI *et al.*, 2015).

2.4 FUNDAMENTALS OF JET-SURFACE INTERACTION EFFECTS

Important theoretical works about the influence of solid boundaries in the flow were presented by Curle (1955) and Ffowcs Williams and Hall (1970). The former study extended Lighthill's theory by considering the presence of solid boundaries in a turbulent flow, but using the free-field Green's function. Simplifications introduced to the formulation showed that an acoustically compact surface acts as a compact dipole source, more efficient than the Lighthill's compact quadrupoles and scaling with U^6. Ffowcs Williams and Hall (1970) considered the problem of

sharp-edges in the flow, by employing a tailored Green's function, representative of a semi-infinite plane. The authors found that the edge scattering noise is even more efficient at low Mach numbers, scaling with U^5 when eddies are close to the edge of the half plane ($2kr_0 \ll 1$, r_0 is the distance between source and edge).

2.4.1 Experimental investigations

Experimental investigations on jet-wing and jet-flap interaction are reported herein. The objective is to analyze the main parameters employed in each study and observe the main conclusions about the phenomenon of installation noise. Figure 2.1, shows a summary of the main parameters investigated in the literature: L_{TE} is the axial position of the trailing edge, H is the radial position of the model wing or plate and δ is the flap deflection (if considered in the study). Some studies also considered the presence of a cutouts or discontinuities in the flaps (Figure 2.1(b))

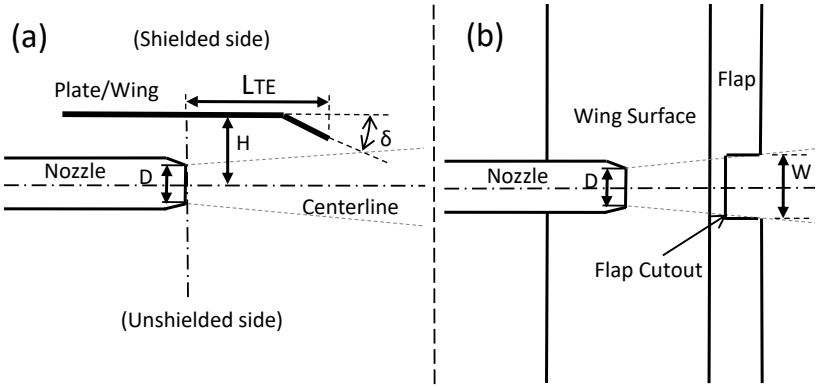

Figure 2.1 – Scheme of the main parameters investigated experimentally in the literature. (a)side view, (b)under-the-wing view.

The work of Wang (1980) is an experimental investigation of the jet-wing interaction noise using a single-flow nozzle and a flat wing model section. The parameters analyzed under static conditions were the distance between the plate and the jet axis, the axial position of the wing relative to the nozzle and the jet exhaust velocity.

Surface effects on the entrainment regions between jet and wing were highlighted by the author as a potential noise source in the low-frequency region. Moreover, reflection of jet noise was considered the main contribution for the high-frequency noise. The author pointed out that jet characteristics are important factors at high frequencies, since the reflected jet noise components must pass through the jet flow in order to reach the observer. During this path, such components are subjected to reflection, refraction and absorption. These effects lead to azimuthal variations of the sound field.

Shearin (1983) investigated the jet-installation effects under static conditions with a model scale wing with flaps and a single-flow nozzle. Parametric tests were carried out including the presence of cut-outs on the flaps (see Figure 2.1(b)). The author identified the major sources of noise in each frequency range. The low-frequency region was dominated by the effects of the jet-wing surface interaction and the jet-wing vertical distance was found to be the main parameter. In the mid-frequencies, the main contribution came from the trailing edge and side edge of the cut-outs. Finally, the major source in high frequencies was associated with the impingement of the jet flow on the flaps, high flap deflections and small cut-out widths. In other conditions, without cut-out and with no direct impingement, the jet noise reflection is taken as the main source in this frequency range. The parametric analysis showed that reduction in noise levels is obtained by increasing the jet-wing distance and cut-out widths. On the other hand, greater axial distances between the nozzle exit and the trailing edge (L_{TE}) and flap deflections increased the noise levels.

A significant drawback of previous works is the fact that they were carried out under static conditions. Pastouchenko and Tam (2005) highlighted the importance of considering flight effects due the interaction of the flow around the wing with the jet. Also, Mengle (2011) reinforced the importance of flight effects, as it changes the development of the jet flow, and consequently, affects the interaction between the turbulent scales and the structures of the aircraft.

An important study by Boeing was realized at the Low Speed Aero-acoustics Facility (LSAF) and reported by Shivashankara and Blackner (1997) and Blackner and Bhat (1998). The authors tested a high BPR engine model in conjunction with

a model aeroplane. The flight effects were also considered and different flap configurations were assessed. Sources of noise were also identified using an elliptic mirror microphone. The installation affected all frequencies and increased noise levels of the jet mixed-ambient and secondary-ambient sources. Between the wing and the jet, the flow velocity was slower when compared to the isolated jet, increasing the relative velocity, thus rising the noise levels. The wing reflection was also an important effect, especially for the secondary-ambient source. The effect of flap deflection was perceived as a monotonic increase in noise. It affects both the flow speed under the wing and the flow angularity due to wing camber, which modify the jet entrainment region and the deformation of the jet by the downwash effect. The authors included the effect of the pylon and found out that the use of wider bifurcations lead to noise level increase. Also, pitching the nozzle up caused a flattening in the upper part of the jet wake, increasing noise levels, while pitching the nozzle down led to insignificant changes in noise levels.

Mead and Strange (1998) experimentally studied the jet-wing installation effects using a model-scale nozzle and several wing geometries (a rectangular flat plate, a wing planform shaped flat plate and a detailed wing model). One of the main features of their work is the focus on sideline noise. Tests were realized with and without external flow and with different sets of engine power. Results from the rectangular plate highlighted the effects of the trailing-edge scattering, which tends to have less importance at lower azimuth angles, that is, closer to the wing (dipole directivity). Similar conclusions to Wang (1980) were drawn about the high-frequency reflection and its azimuthal variations due to the jet refraction effect. Based on the results for other wing geometries, the authors suggested that the wing area for noise reflection and position of trailing edge are important parameters. Results for the model wing presented low-frequency reduction in the forward arc. However, reflection noise was not modified by the surface curvature change and flight effects.

Elkoby (2005) conducted a full-scale investigation of the installation effects comparing a full scale flight test with a full scale static engine test. In summary, the full-scale tests showed similarity with model scale results. Noise increases in the forward arc low frequencies were similar to those due to the trailing edge and wing effects. The author pointed out the significance of the

leading-edge diffraction, which is not considered in some model scale tests. Although good results were obtained, the complexity of the tests and the comparison of the flight test with the static engine test under different external conditions made it difficult to identify the sources in full-scale.

The work of Mengle (2011) was concerned with the parametric study of the jet-flap interaction including the effects of the wing height, flap deflection angle and the use of chevron nozzles. Flap deflection and small wing heights led to the appearance of two peaks in the front-arc spectra. A close analysis of both of the two peaks shows that, for the same emission angle, the lower frequency peak shifts to a higher frequency band when the flight effect was considered. However, no significant changes occurs in the high frequency peak. The author suggested that the former arises from amplification of the outer shear layer turbulent structures by the flap trailing edge. Moreover, the higher frequency peak was attributed to the gap left between the inboard and outboard flaps, generating a flap side-edge component, or even by the amplification of the inner shear-layer. The author suggested more analyses for unequivocal conclusions.

The effects of chevron nozzles on installation effects was assessed by some authors. Mengle *et al.* (2007) used a dual-stream nozzle with azimuthally varying fan chevrons in a study of flap trailing edge modifications aimed at installation noise reduction. Chevrons affected the effectiveness of these geometry modifications. Moreover, Mengle (2011) concluded that chevrons reduced the installation noise in the front arc by around 5 dB compared to the round nozzle. Also, this nozzle geometry led to the appearance of multiple peaks in the spectra. Kopiev *et al.* (2013) analyzed the influence of four dual-stream nozzle geometries, one without chevrons, one with chevrons on the secondary and two configurations with chevrons on the primary and secondary. Chevron nozzles reduced the low frequency noise associated with diffraction, but also resulted in a thicker shear-layer, reducing the proximity of the jet to the wing.

Although several investigations comprised complex or detailed geometries, some authors assessed simpler cases of jet-flat-plate interactions, seeking a more fundamental analysis. Lawrence *et al.* (2011) and Lawrence (2014) experimental studies were focused on the interaction of the jet flow with a large flat-plate. The main geometric parameter of the test consisted of

the plate trailing edge position. The authors found out that, if the trailing edge position is moved downstream, the corresponding peak is shifted to lower frequencies and the noise level is risen. The new position leaves the trailing edge subjected to interaction with larger scales which are responsible for lower frequencies noise and also have the major part of the flow energy. The peak frequency also changes with the height of the plate. Different types of source characteristics were observed whether the trailing edge was located inside the non-linear hydrodynamic field or not.

Cavalieri *et al.* (2014) conducted an experimental investigation of jet-plate interaction. The Mach numbers ranged from 0.4 to 0.6 and the distances of the plate relative to the jet axis ranged from 1 to 2 jet diameters. Results of the installation effects were similar to those found by Mead and Strange (1998) and Lawrence *et al.* (2011). An analysis of the distance between the plate and the jet showed an exponential variation of the SPL with the distance, which led to the conclusion that the increase in the sound levels comes from the fluctuations on the hydrodynamic near-field and could be related to the scattering of wavepackets in the jet. Futhermore, the coherence values between microphones at 90° and 20°, which were not significant for isolated jets, presented considerable values with the presence of the plate and became even higher when the plate was positioned closer to the jet. As already explored, wavepackets have important contribution to the noise at 20° and this coherence analysis supports the idea of the scattering of wavepackets in the installation noise.

Piantanida *et al.* (2016b) investigated the jet-plate interaction considering variations of the trailing-edge sweep angle[6] in addition to Mach number and plate radial position. The results confirmed the exponential dependence of the noise with the plate distance when the plate is not inside the region with strong flow interaction. In this specific case, at a distance of H=0.6D, a change in the polar trends of the spectrum occurred and it was suggested that the grazing flow on the plate adds a second source independent of the wavepacket due to the scattering of the boundary layer noise. In general, the sweep angle caused a narrowing of the azimuthal radiation lobes, with the peak at the long-chord side and considerable noise reductions at azimuthal angles 90° and 270° (shielded and unshielded sides respectively). The maximum reductions were about $8dB$ for the sweep angle 45°.

[6] Angle between the jet axis and the trailing edge

In cases with strong jet-surface interaction, in configurations with deployed flaps and specific Mach numbers, some authors found the presence of multiple anharmonic tones in narrow-band far-field spectra (LAWRENCE, 2014; LAWRENCE; SELF, 2015). These tones could be also related to the double peak observed in 1/3 octave spectra by Mengle (2011). Lawrence and Self (2015) related the occurrence of these peaks to a jet instability feedback mechanism. Recently Jaunet *et al.* (2016) attributed the peaks to trapped acoustic waves inside the potential core of subsonic turbulent jets (TOWNE *et al.*, 2017).

In general, the analyses of the experimental works led to a series of conclusions related to the installation effects. The following main features were pointed by the authors:

- Trailing edge and leading edge scattering;
- Exponential dependence of the scattered noise with plate proximity (without strong flow interaction);
- Jet entrainment modification due to the presence of the wing;
- Acoustic reflection on the wing and flaps;
- Jet refraction/blockage, which influences mainly in the azimuthal directivity;
- Flap side-edge noise when gaps are present on the flaps;
- Tonal noise in configurations with high flap intrusion.

Furthermore, the installation effect is more prominent in the forward arc and its effects reduces as the observer moves to the rear arc (WANG, 1980; SHIVASHANKARA; BLACKNER, 1997; MEAD; STRANGE, 1998; MENGLE, 2011). A dipole azimuthal directivity pattern was found for the low frequency noise while the jet blockage is responsible for azimuthal variation in high frequencies (WANG, 1980; MEAD; STRANGE, 1998). Finally, the wing position related to different jet flow regions and the exponential dependence of noise with plate proximity were pointed out as key aspects of the trailing-edge noise field (LAWRENCE *et al.*, 2011; CAVALIERI *et al.*, 2014; PIANTANIDA *et al.*, 2016b).

About geometrical modifications, the trailing-edge sweep angle was shown to be a very effective solution to reduce scattering noise. Some efforts were also directed to the use of composite plates (CAVALIERI *et al.*, 2015; PIANTANIDA *et al.*, 2016a).

2.4.2 Semi-Empirical Prediction Methods

The prediction of installation effects is substantial in the aeroacoustic design of aircraft and, due to computational limitations, steady state CFD simulations together with semi-empirical methods play an important role inside the industrial context. The review of works presented herein has the purpose of introducing semi-empirical prediction methods for the jet-wing and jet-flap interaction, as well as the main conclusions of parametric analyses.

Bhat and Blackner (1998) extended the coaxial jet semi-empirical method of Lu (1986) to predict installation effects. Basically, the differences of noise level between installed and isolated configurations were considered to be associated with flap deflections, engine position, angle of attack, external flow, pylon, etc. Good predictions in lower frequencies were verified with experimental data, but the spectral SPL curve shape of the higher frequencies was not satisfactory.

Pastouchenko and Tam (2005) used a computational acoustic method, designed to predict the noise generated by the fine scale turbulence (TAM; AURIAULT, 1999), in order to investigate the interactions between the jet and the downwash of the wing. The analysis was carried out in three main parts. First, the calculation of the downwash from a wing-flap in high-lift configuration was solved considering an inviscid flow model (Euler and energy equations). Second, a RANS simulation of a dual stream jet was performed with a modified $k - \epsilon$ turbulence model, using results of the previous simulation as a boundary condition. Finally, acoustic results were obtained. Good agreement with experimental data at higher frequencies was verified, as the model was only concerned with the noise from what they called fine scale turbulence. Moreover, the authors pointed out the necessity of a method which can account for the noise from the large turbulent structures.

Mc Laughlin *et al.* (2007) developed a method based on ray theory, designed to predict noise from the reflection of the wing and hot-jet blockage. This approach is an approximation valid only for high frequencies and does not account for diffraction effects at sharp edges. A 2D model was used to predict the effects of jet blockage by the hot jet. The results showed good agreement with experimental data. Further improvement, using an empirical jet blockage model, was carried out by Mc Laughlin *et al.* (2008).

Although some interesting methods are available in the literature, only the method of Bhat and Blackner (1998) seem to cover most of the issues behind the jet-flap installation, being also a convenient method in terms of implementation and computational cost. However, this method was developed mostly based on empirical data, with limited amount of flow physics (PASTOUCHENKO; TAM, 2005). Still, there is a demand for simple and fast methods for predicting noise from the jet-flap interaction. In the following section, models based on wavepacket theory, but concentrated on the scattering effects in simple geometries, are discussed.

2.4.3 Wavepacket models and installation noise

Cavalieri *et al.* (2014) used a wavepacket source model for the jet and calculated the scattering on a flat plate in two ways: using a tailored-green function (FFOWCS WILLIAMS; HALL, 1970) and by solving the Helmholtz equation using a Boundary Element Method (BEM). Measurements of the turbulent velocity field showed that there was no considerable deformation of the jet in the range of the positions of the experiments, a fact that allows the use of such a model source. The tailored Green's function approach was applied in the analysis of a semi-infinite plane, while the BEM solution of the Helmholtz equation was used in a finite plate. Directivity results showed that, in the case of the finite plate, the scattering in each plate edge created an interference pattern. Results showed lower noise levels in comparison with the experimental results for 90°. However, both methods captured some characteristics of the installation effects: the low-frequency amplification, the dipolar directivity and the exponential behaviour of sound due to the jet-plate distance.

In a similar way, Piantanida *et al.* (2016b) applied the wavepacket model source with the tailored Green's function and a computation by BEM, to analyze the effects of the trailing-edge sweep. The model could predict well the variation of the noise with the plate distance. The sweep trends could also be effectively predicted by the model, specially at the shielded side.

Nogueira *et al.* (2016a) extended the analysis of Cavalieri *et al.* (2014) by using the solutions from PSE instead of the simplified wavepacket model with the tailored Green's function approach. The method was shown to capture the directivity trends for the scattering effect, however, levels were about $13dB$ lower for

$St = 0.2$ and plate positioned at a radial distance $r/D = 1$. These deviations increased as the plate was moved away from the jet, tending towards the isolated jet condition. As previously observed, these deviations are due to the linearity of the method.

More recently, Nogueira *et al.* (2017) considered a cylindrical wavepacket source concentrated on the lipline instead of the complete radial information and propagated it with the tailored Green's function approach (CAVALIERI *et al.*, 2014). Results showed that this simplification is valid, with small changes to the radiated sound. The study used the model paramenters obtained from far-field measurements by Cavalieri *et al.* (2012). In order to help in the analysis, the spatial Fourier transform of the tailored Green's function was used. Similar to the findings with the free field Green's function, for the z direction (parallel to the trailing edge), only wavenumbers corresponding to supersonic phase velocities were seen to radiate to the far field ($|k_z| < k$) (CAVALIERI; AGARWAL, 2014). However, in the axial direction, the absolute steep decay normally found in this radiation region was not present, and so, wavenumbers outside this region that would normally generate evanescent waves can now radiate noise with the presence of the plate. Results in the wavenumber space also supported the sensitivity analysis in relation to the wavepacket parameters. In summary, the authors found that the axisymetric mode is the most efficient for installed jets, the scattered field increases exponentially with the wavepacked phase velocity, the scattered field in not very sensitive to the source extent and coherence decay and that compact sources are less efficient in the installed jet problem. In addition to the radial distance of the plate, the authors also investigated the axial position of the trailing edge. The scattering effects were found to be significant when the center of the wavepacket is positioned upstream of the trailing edge. Noise reductions due to trailing-edge sweep and plate angle of attack were also explored with the model.

2.5 CONTRIBUTIONS OF THE PRESENT STUDY

The wavepacket models reproduce many jet-noise characteristics, such as axisymmetric superdirectivity, the azimuthal structure of the sound field and the intermittency in sound generation (JORDAN; COLONIUS, 2013). The idea of modeling the jet noise generation based on orderly structures is

tempting, due to their low order in comparison with the complete non-linear jet flow. Based on the literature review, the following contributions are proposed for the present work:

- **Assessment of the prediciton capabilities of simulations based on the LBM**

  As already mentioned, the development of numerical tools allows complementary analyses to the experiments, specially regarding the analysis of two-point statistics of the flow field. The recent developments of the Lattice Boltzmann Method (LBM) are worthy of attention, specially due to the reduced computational cost. Results obtained with a LBM simulation model are compared to a LES database in Chapter 4. The adequacy of predictions from both approaches for the present study was thus assessed.

- **Investigation of the source terms that possess the main contributions to the jet-plate interaction noise**

  Based on the studies that indicated the dominance of the linear part of momentum term of Lighthill's source (FREUND, 2001; FREUND, 2003; BODONY; LELE, 2008), one of the contributions of this work is to analyze and identify the components that contribute the most to the installed jet sound field. The focus of this work is directed to the axisymmetric mode of the term T_{xx}. This term is dominant in the sound radiation towards low angles as pointed out by Crighton (1975) and may be the most important term in the jet-plate interaction case. Hence, by using a numerical simulation database, the idea is to further split the source for the axisymmetric mode in order to observe the contribution of T_{xx} at the far-field, especially for the installed case.

- **Adjutment of simplified wavepacket models, including coherence decay, based on data from high fidelity simulations. Sensitivity analysis to errors in the adjustment procedure**

  Some studies showed that, in the case of jet-plate interaction, the installation noise comes from the scattering of the wavepackets in the near-field (CAVALIERI *et al.*, 2014; PIANTANIDA *et al.*, 2016b; NOGUEIRA *et al.*, 2017). Even results with unit coherence model sources were promising. In this work the parameters of simple wavepacket models are educed from the jet velocity field, rather than from the far-field noise data as done in the aforementioned studies. Results based on linear stability theory and simplified linear wavepackets models fail to predict the correct noise levels in subsonic jets. This is possibly due to the missing jittering effect. Studies showed that the coherence decay found in turbulent jets, when included in the linear models, increase the radiating efficiency of the source (CAVALIERI *et al.*, 2011b; CAVALIERI; AGARWAL, 2014; BAQUI *et al.*, 2015). The effects of the source coherence modeling for the installed case are also assessed in the present work.

  The importance of the accuracy in the model source adjustments for the studied configurations and the adequacy of the simple functions used in the modeling are also discussed by comparisons with numerical simulation data.

- **Description of the characteristics of the radiated sound based on simulation and model data**

  The use of a LES adjusted source is expected to give further confirmation about the observations of Cavalieri *et al.* (2014), Cavalieri and Agarwal (2014) and Nogueira *et al.* (2017). There is a demand for simple prediction models for isolated and installed jet noise based on the physics of the noise generation mechanisms. The use of numerical data to adjust simplified wavepacket models and investigation of coherence effects in installed jets contribute to the understanding of the jet noise phenomena and also to the development of a simple prediction method for installed jet noise.

3 MODELS AND SOLUTION PROCEDURES

The present analysis involves the use of a numerical database to explore the most significant source mechanisms mainly for installed jets but also for free jets. Once this information is obtained, simplified wavepacket models are adjusted based on the source field information. The primary idea is to avoid adjusting the models with far-field data, as done by Cavalieri *et al.* (2012). Due to its high influence in both directivity and noise level of free jets (CAVALIERI; AGARWAL, 2014; BAQUI *et al.*, 2015), sensitivity to the modeled coherence decay for installed jets is to be explored with fitted data from a convenient numerical source.

The first attempt to find a numerical database involved LBM based simulations. The prediction capabilities of the method are assessed by comparison with experimental data for jets with $M = 0.4$ and 0.9. The reliability of the simulations for the analyses that follow is inspected and results are confronted to available LES data (BRÈS *et al.*, 2015) in order to define the most suitable database for the study.

3.1 GEOMETRY AND EXPERIMENTAL DATA

Simulations were based on the experiments realized at CEAT (*Centre d'Études aérodynamiques & Thermiques*), Poitiers, France by Piantanida *et al.* (2016b). The experiment consisted of a single flow nozzle of diameter $D = 50$ mm, positioned under a rectangular plate, as shown in the sketch of Figure 3.1. A total of 324 acoustic field measurements were taken in a cylindrical surface of radius $R = 14.2D$.

The trailing-edge position at the center of the plate is $x/D = 4$ and r is the distance measured from the nozzle axis. From all the studied configurations, only the free-jet case and cases with the rectangular plate positioned at $r/D = 1$ and $r/D = 1.5$ are explored in the present study. Also, only data with Mach numbers $M = 0.4$ and 0.9 are presented.

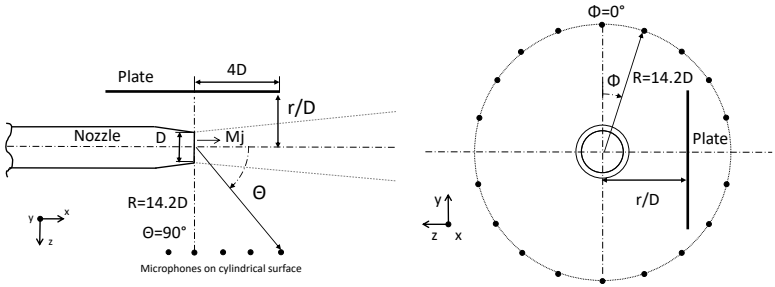

(a) (b)

Figure 3.1 – Scheme of the experimental tests used as reference in this analysis. (a) xz plane view, (b) yz plane view.

3.2 NON-DIMENSIONAL DATA

The data in this document are presented in dimensionless form. All the distances and length scales are divided by the nozzle exit diameter D in m, velocities by the centerline velocity at the nozzle exit U_J in m/s, and densities by the free-field quantity ρ_0. Other variables are defined as follows:

- Strouhal number: $St = \frac{fD}{U_J}$, where f is the frequency in Hz;
- Time: $t = \frac{t_{dim}U_J}{D}$, where t_{dim} is the dimensional time in s.
- Reynolds number: $Re = \frac{\rho_0 U_J D}{\mu}$, μ is the dynamic viscosity of the fluid
- Jet acoustic Mach number: $M = U_J/c_0$, where c_0 is the free-field sound speed in m/s.

3.3 SOURCE TERM AND ITS SIMPLIFICATIONS

The source term used in this study is based on the right side of the Lighthill (1952) equation given by,

$$\frac{\partial^2 \rho}{\partial t^2} - c_0^2 \nabla^2 \rho = \frac{\partial^2 T_{ij}}{\partial x_i \partial x_j}, \tag{3.1}$$

where the Lighthill's tensor T_{ij}, with viscous terms neglected, is defined as,

$$T_{ij} = \rho U_i U_j + (p - c_0^2 \rho)\delta_{ij}. \tag{3.2}$$

Now, several simplifications are applied to the source term. The entropy term is not considered and source density variations are substituted by the mean ρ_0. The Lighthill's equation can also be written for the pressure fluctuation,

$$\nabla^2 p - \frac{1}{c_0^2}\frac{\partial^2 p}{\partial t^2} = -\frac{\partial^2 \rho_0 U_i U_j}{\partial x_i \partial x_j}. \tag{3.3}$$

Under the hypothesis of the predominance of the momentum term T_{xx}, the source term in cylindrical coordinates is given by:

$$\frac{\partial^2 T_{xx}(x, r, \phi, t)}{\partial x^2} = \rho_0 \frac{\partial^2}{\partial x^2} U_x^2(x, r, \phi, t). \tag{3.4}$$

By separating mean and fluctuating parts of the axial velocity $U_x = \overline{U_x} + u_x$ and considering only the linear part by neglecting the quadratic terms u_x^2,

$$S^t(x, r, \phi, t) = \frac{\partial^2 T_{xx}}{\partial x^2} = \rho_0 \frac{\partial^2}{\partial x^2} 2\overline{U_x}(x, r) u_x(x, r, \phi, t). \tag{3.5}$$

The source is decomposed into azimuthal Fourier modes, as we are only interested in the axissymmetric component:

$$S^t(x, r, m, t) = \frac{1}{2\pi}\int_{-\pi}^{\pi} S^t(x, r, \phi, t) e^{im\phi} d\phi, \tag{3.6}$$

and only $m = 0$ is considered, i. e.:

$$S^t(x, r, m = 0, t) = \rho_0 \frac{\partial^2}{\partial x^2} 2\overline{U_x} u_x(x, r, m = 0, t). \tag{3.7}$$

The superscript t implies that the quantities are in the time domain. This source term is Fourier transformed by using the following convention:

$$S = \frac{1}{2\pi}\int_{-\infty}^{\infty} S^t e^{-i\omega t} dt. \tag{3.8}$$

3.4 COMPUTATION OF THE ACOUSTIC PRESSURE AT OBSERVER POSITION

The calculation is done in the frequency domain, based on the integral solution of the inhomogeneous Helmholtz equation for the acoustic pressure,

$$p(\mathbf{x},\omega) = \int_V S(\mathbf{y},\omega)G(\mathbf{x},\mathbf{y},\omega)d\mathbf{y}. \tag{3.9}$$

For the free jet case, $G = G_0$ is the free-field Green's function given as,

$$G_0 = \frac{e^{-ikR}}{4\pi R} \tag{3.10}$$

where R is the distance between source an observer and $k = \omega/c_0$ the acoustic wavenumber.

For the installed jet case, the problem is modeled as the jet scattering from a semi-infinite plate. This approach has been used with wavepacket models and was shown to be representative of the problem, although some deviations occur due to the differences to the actual geometry of finite plate (CAVALIERI *et al.*, 2014; PIANTANIDA *et al.*, 2016b; NOGUEIRA *et al.*, 2017). The tailored Green's function from Ffowcs Williams and Hall (1970) is used,

$$4\pi G_t = \frac{e^{\frac{1}{4}i\pi}}{\sqrt{\pi}} \left\{ \frac{e^{-ikR}}{R} \int_{-\infty}^{U_R} e^{-iu^2} du + \frac{e^{-ikR'}}{R'} \int_{-\infty}^{U_{R'}} e^{-iu^2} du \right\} \tag{3.11}$$

where,

$$U_R = 2\left(\frac{krr_0}{D+R}\right)^{\frac{1}{2}} \cos\frac{\theta-\theta_0}{2} = \pm\left[k(D-R)\right]^{\frac{1}{2}}, \tag{3.12}$$

$$U_{R'} = 2\left(\frac{krr_0}{D+R'}\right)^{\frac{1}{2}} \cos\frac{\theta+\theta_0}{2} = \pm\left[k(D-R')\right]^{\frac{1}{2}}, \tag{3.13}$$

$$R = \left\{r^2 + r_0^2 - 2rr_0\cos(\theta-\theta_0) + (z-z_0)^2\right\}^{\frac{1}{2}}, \tag{3.14}$$

$$R' = \left\{ r^2 + r_0^2 - 2rr_0 \cos(\theta + \theta_0) + (z - z_0)^2 \right\}^{\frac{1}{2}}, \tag{3.15}$$

$$D = \left\{ (r - r_0)^2 + (z - z_0)^2 \right\}^{\frac{1}{2}}. \tag{3.16}$$

The tailored Green's function in its original form, assumes a cylindrical coordinate system with the axial coordinate aligned with the trailing edge. The position of the source point in this coordinate system is (r_0, θ_0, z_0) and the observer (r, θ, z). R is the distance between source and observer and R' is the distance between the source's mirrored image $(r_0, -\theta_0, z_0)$ and observer. Calculating in the default coordinate system from Figure 3.1:

- Distance between source and observer

$$R = \sqrt{(x_{obs} - x_s)^2 + (z_{obs} - z_s)^2 + (y_{obs} - y_s)^2} \tag{3.17}$$

-Distance between image source and observer

$$R' = \sqrt{(x_{obs} - x_s)^2 + (z_{obs} - z_{image})^2 + (y_{obs} - y_s)^2}, \tag{3.18}$$

- Distance between observer and trailing edge

$$r = \sqrt{(x_{obs} - x_{plate})^2 + (z_{obs} - z_{plate})^2}, \tag{3.19}$$

- Distance between source and trailing edge

$$r_0 = \sqrt{(x_s - x_{plate})^2 + (z_s - z_{plate})^2}, \tag{3.20}$$

$$\theta = \arcsin \frac{(z_{obs} - z_{plate})}{r}, \tag{3.21}$$

$$\theta_0 = \arcsin \frac{(z_s - z_{plate})}{r_0}, \tag{3.22}$$

where the subscript s denotes the coordinate for the source position, *obs* for the observer position and *plate* for the plate's trailing edge position. The angles θ and θ_0 are defined in $[0, 2\pi[$.

3.4.1 Source derivative problems

Due to the undesirable results caused by the double spatial derivatives of turbulent velocity data, it is more convenient to switch the derivatives to the Green's function. By applying integration by parts twice in equation 3.9,

$$\int_V \frac{\partial^2 T}{\partial \mathbf{y}^2} G d\mathbf{y} = \int_V T \frac{\partial^2 G}{\partial \mathbf{y}^2} d\mathbf{y} + \int_S \left(\frac{\partial T}{\partial \mathbf{y}} G - T \frac{\partial G}{\partial \mathbf{y}} \right) \mathbf{n} dS \tag{3.23}$$

The surface integral is null as long as fluctuations are zero at the boundaries. Under these assumptions, equation 3.23 shows that the double derivative in the source term can be switched to the Green's function. The source term in equation 3.9 term is now represented by,

$$S = T_{xx} = \rho_0 2\overline{U_x} u_x(x, r, m = 0, \omega), \tag{3.24}$$

and the Green's function

$$G_{xx} = \frac{\partial^2 G(\mathbf{x}, \mathbf{y}, \omega)}{\partial x^2}. \tag{3.25}$$

For the free-field Green's function the derivatives are,

$$\begin{aligned} \frac{\partial G}{\partial x^2} = -ik \frac{\exp(-ikR)}{4\pi R^2} &+ (1 - k^2) \frac{\exp(-ikR)}{4\pi R^3} \\ &- (2(x_{obs} - x_s)^2 + ik) \frac{\exp(-ikR)}{4\pi R^4} \\ &+ (x_{obs} - x_s)^2 \frac{\exp(-ikR)}{4\pi R^5}. \end{aligned} \tag{3.26}$$

For the tailored Green's function, a derivation procedure was conducted by Nogueira *et al.* (2016a). Their final result are adopted in this study but the final equations are omitted here. In order to simplify the notation, $G = G_{xx}$ will now refer to the double derivative of the Green's function.

3.4.2 Two-point statistics approach

The Fourier transform of turbulent flow variables is not defined since they are not square-integrable functions as observed by Cavalieri and Agarwal (2014). In this sense, the auto- and cross-correlations of the fluctuating velocity field can be used to overcome this problem, as they possess a Fourier transform. Thus Equation 3.9 can be rewritten by multiplying it for its complex conjugate and writing it in terms of its ensemble average:

$$\langle p(\mathbf{x}, m, \omega) p^*(\mathbf{x}, m, \omega) \rangle = \int_V \int_V \langle S(\mathbf{y_a}, m, \omega) S^*(\mathbf{y_b}, m, \omega) \rangle G(\mathbf{x}, \mathbf{y_a}, \omega) G^*(\mathbf{x}, \mathbf{y_b}, \omega) d\mathbf{y_a} d\mathbf{y_b} \tag{3.27}$$

where $\mathbf{y_a} = (x_a, r_a, \phi_a)$ and $\mathbf{y_b} = (x_b, r_b, \phi_b)$ represent the first and second source coordinates, $\langle \cdot \rangle$ denotes an ensemble average and $*$ the complex conjugate. This equation relates Power Spectral Density (PSD) of the acoustic pressure field to the Cross Spectral Density (CSD) of the source field. By including the discussed assumptions, the fundamental equation of this study can be obtained:

$$\langle p(\mathbf{x}, m, \omega) p^*(\mathbf{x}, m, \omega) \rangle = \int_V \int_V \langle T_{xx}(\mathbf{y_a}, m = 0, \omega) T^*_{xx}(\mathbf{y_b}, m = 0, \omega) \rangle \frac{\partial G(\mathbf{x}, \mathbf{y_a}, \omega)}{\partial x_a^2} \frac{\partial G^*(\mathbf{x}, \mathbf{y_b}, \omega)}{\partial x_b^2} d\mathbf{y_a} d\mathbf{y_b}. \tag{3.28}$$

3.4.3 Numerical integration procedure

For the noise calculations the numerical procedure is performed for one St and one observer position at a time as follows:

- The CSD of the source term is calculated for each set of points $i = 1, 2, ...N$ and $j = 1, 2, ...N$ in the discretized source domain consisting of a total of N points. As the $m = 0$ source is independent of the azimuthal coordinate, it is defined in a

plane. The data is processed the form of a complex matrix $N \times N$, $C_{ij} = S_i S_j^*$

- For a given St and observer position, calculate the derivative of the Green's function for each source point at each azimuthal angle $[G_1, G_2 ... G_N]_\phi$
- Calculate $[G_i G_j^*]_\phi$ for each point and integrate the result in the azimuthal direction. As $m = 0$, the source is independent of ϕ, the integration is done only for $G_i G_j^*$
- Multiply each position of the source CSD matrix $C_{ij} = S_i S_j^*$ by the resulting integral $[G_i G_j^*]$ and integrate the products numerically.

To perform the aforementioned procedure, a script was developed in Matlab with the two-point statistics approach (Equation 3.28). The developed code was based on the codes used by Cavalieri *et al.* (2014) and Piantanida *et al.* (2016b), which were focused on the solution of Equation 3.9. For calculating the differentiated tailored Green's function, the code from Nogueira *et al.* (2017) was adapted.

The implementation of the code was validated by using the source terms employed by Cavalieri *et al.* (2012) and Cavalieri and Agarwal (2014) for the free jet case and by Cavalieri *et al.* (2014) for the installed case. The used parameters source parameters were based on those obtained by (CAVALIERI *et al.*, 2012) for $M = 0.6$ and $St = 0.2$: $k_h L = 6$ and $L = 4.6D$ .Results with the two-point statistics code are compared to analytical solutions in Figure 3.2 (a) and (b). Very good agreement can be observed, with the exception of high angles ($\theta_{obs} \geq 150°$) in Figure 3.2 (a). In fact, noise levels are very low in this region (below 0 dB) and may present the same order as computational errors. These errors do not appear when the source with modeled coherence is considered, as shown in Figure 3.2(c). In the jet-plate case, results showed good agreement with those obtained by Cavalieri *et al.* (2014) (Figure 3.2(b)).

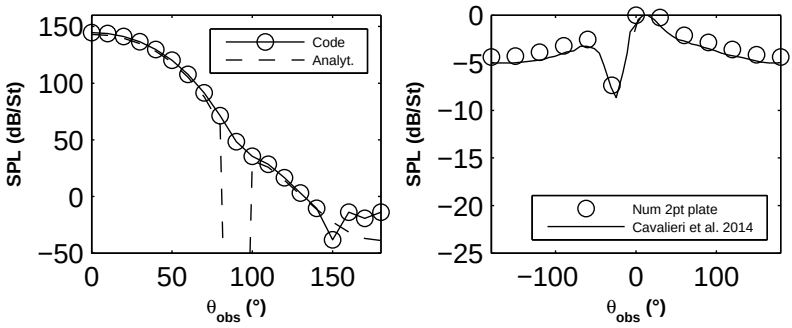

(a) Free-jet (b) Installed jet

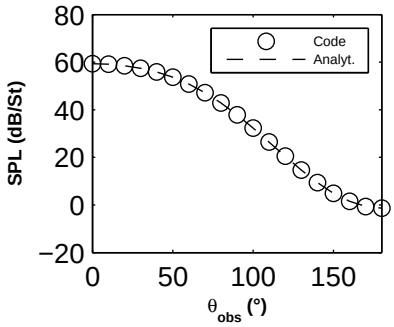

(c) Free jet with modelled coherence

Figure 3.2 – Validation of the implemented code by comparison to analytical data from Cavalieri *et al.* (2012), Cavalieri and Agarwal (2014) and results from Cavalieri *et al.* (2014).

3.5 CALCULATION OF THE CSD FROM THE NUMERICAL DATA

The cross spectral densities are calculated by the Welch method (WELCH, 1967), by dividing the time signal S_n^t, for each i or j point of the $Nx \times Nr$ domain, in sub-samples of $Nfft$ points. Each sub-sample n or block is multiplied by a window function $w(t)$ and its discrete Fourier transform is taken by means of a fast Fourier transform (fft) algorithm. Thus the CSD is given by:

$$CSD_n = [S_i S_j^*]_n / Nfft, \tag{3.29}$$

where,

$$[S_i S_j^*]_n = \\ [fft(S_i^t(r_i, x_i, Sub_n)w(t))fft(S_j^t(r_j, x_j, Sub_n)w(t))^*]/Nfft. \tag{3.30}$$

The CSD is estimated by averaging the results for all the blocks (N_{blocks}),

$$\langle S_i S_j^* \rangle = \frac{1}{N_{blocks}} \sum_n [S_i S_j^*]_{sub-n}. \tag{3.31}$$

Results are presented divided by the resulting St band. Amplitudes are also corrected with a scaling factor (Sf) depending on the window function (SHIN; HAMMOND, 2008):

$$Sf = \sqrt{\frac{\int_{-T_w/2}^{T_w/2} w_{rect}^2 dt}{\int_{-T_w/2}^{T_w/2} w^2 dt}} \tag{3.32}$$

where w_{rect} is the rectangular window function and T_w is the width of the window. The choice of the window function is further discussed in Chapter 5.

The described procedure was implemented in a Matlab script in which the Cross spectral matrix $\langle S_i S_j^* \rangle$ is computed for an individual St at time for all the considered source positions. The output is a $(N_x N_r) \times (N_x N_r)$ complex matrix which can be used in two ways: to directly obtain the sound field or to adjust the source model parameters, as described in the next section.

3.6 MODELING OF THE SOURCE CSD

Model sources used in this work are based on the wavepacket line source model presented by Crow (1972) (see Crighton (1975)):

$$T_{xx}(x, r, m = 0, \omega) = 2\rho_0 \overline{U_x} u_x e^{-ik_h x} e^{-x^2/L^2}. \tag{3.33}$$

This source and variations were used by Cavalieri *et al.* (2012), Cavalieri *et al.* (2014), Piantanida *et al.* (2016b) and Nogueira *et al.* (2017), some of them introducing radial information with the insertion of radial profiles obtained via PSE solutions. Based on the source proposed by Cavalieri and Agarwal (2014) the following source model is proposed:

$$\begin{aligned}\langle S(\mathbf{y_a}, \omega) S^*(\mathbf{y_b}, \omega) \rangle = \\ A \exp\left(-\frac{(x_a - X_c)^2}{L_x^2} - \frac{(x_b - X_c)^2}{L_x^2}\right) \exp\left(-\frac{r_a^2}{L_r^2} - \frac{r_b^2}{L_r^2}\right) \\ \exp\left[-ik_h(x_a - x_b)\right] \exp\left(-\frac{|\mathbf{y_a} - \mathbf{y_b}|^2}{L_c^2}\right),\end{aligned} \tag{3.34}$$

in which the CSD of the source term is represented by 6 global parameters. A represents the maximum PSD amplitude, whose axial decay is represented by a Gaussian profile centered at X_c with characteristic length L_x. The radial profile is also represented by a Gaussian profile with envelope length L_r. Centering this second Gaussian at zero was taken as a reasonable assumption. Axial phase difference is defined by the hydrodynamic wavenumber k_h, related to the phase velocity U_c. Finally the coherence decay is represented by Gaussian profiles of characteristic length L_c. The parameters were obtained by minimizing the sum of the squares of the absolute error between the numerical source and the proposed model. The process is carried out with the Nelder-Mead Simplex Algorithm (NELDER; MEAD, 1965).

In order to further simplify the model, a line source approach, similar to Cavalieri and Agarwal (2014) is derived. For a free-jet case, at low St number, with the observer at the far-field with $r_{obs} \gg r_s$, it is acceptable to assume independence of the Green's function with the radial distance. Thus, from equation 3.28, as the $m = 0$ source

is independent of the azimuthal coordinate ϕ, with $\mathbf{y_a} = (x_a, r_a, \phi_a)$ and $\mathbf{y_b} = (x_b, r_b, \phi_b)$,

$$\langle p(\mathbf{x}, m, \omega) p^*(\mathbf{x}, m, \omega) \rangle = \int\int \left[(2\pi)^2 \int\int \langle S(\mathbf{y_a}, m = 0, \omega) S^*(\mathbf{y_b}, m = 0, \omega) \rangle r_a r_b dr_a dr_b \right] \frac{\partial G(\mathbf{x}, \mathbf{y_a}, \omega)}{\partial x_a^2} \frac{\partial G^*(\mathbf{x}, \mathbf{y_b}, \omega)}{\partial x_b^2} dx_a dx_b, \tag{3.35}$$

with the CSD of the line source, S_l, defined as:

$$\langle S_l(x_a, m = 0, \omega) S_l^*(x_b, m = 0, \omega) \rangle = (2\pi)^2 \int\int \langle S(\mathbf{y_a}, m = 0, \omega) S^*(\mathbf{y_b}, m = 0, \omega) \rangle r_a r_b dr_a dr_b, \tag{3.36}$$

Based on this result, the double integral of the LES source (equation 3.24) is used to adjust the parameters for the following line source model:

$$\langle S_l(x_a, m = 0, \omega) S_l^*(x_b, m = 0, \omega) \rangle = (2\pi)^2 A \exp\left(-\frac{(x_a - X_c)^2}{L_x^2} - \frac{(x_b - X_c)^2}{L_x^2} \right) \exp\left[-ik_h (x_a - x_b) \right] \exp\left(-\frac{(x_a - x_b)^2}{L_c^2} \right). \tag{3.37}$$

Both presented source models are compared in Chapter 6.

3.7 SOLUTION PROCEDURE

A summary of the solution procedure is show in Figure 3.3, in which the main steps are indicated by the numbers (1-4). The procedure is divided in two parts: the source definition and the noise field computation. First, the time dependent source obtained from the simulation data is processed and the CSD matrix is computed in step (1), for one specific St value, with the procedure described in Section 3.5. In the case of the model source, the CSDs from step (1) are used to adjust the model parameters for the same St value

in step (2), as described in section 3.6. Both sources can be used in the propagation code (3-4), described in section 3.4.3. In this part, both the Green's function calculation (3) and its integration with the source (4) are repeated for each observer position.

The steps (1), (2) and (3-4) are performed with independent codes and the output data are stored independently. The propagation step of the CSD obtained from the numerical database takes about 90 to 35 minutes per observer position and St value, depending on the size of the grid. For the volumetric source model, the propagation step takes an average of 1.75 minutes per observer position and St value. These values are based on serial computations carried out with an Intel® Core™i7-6700 workstation.

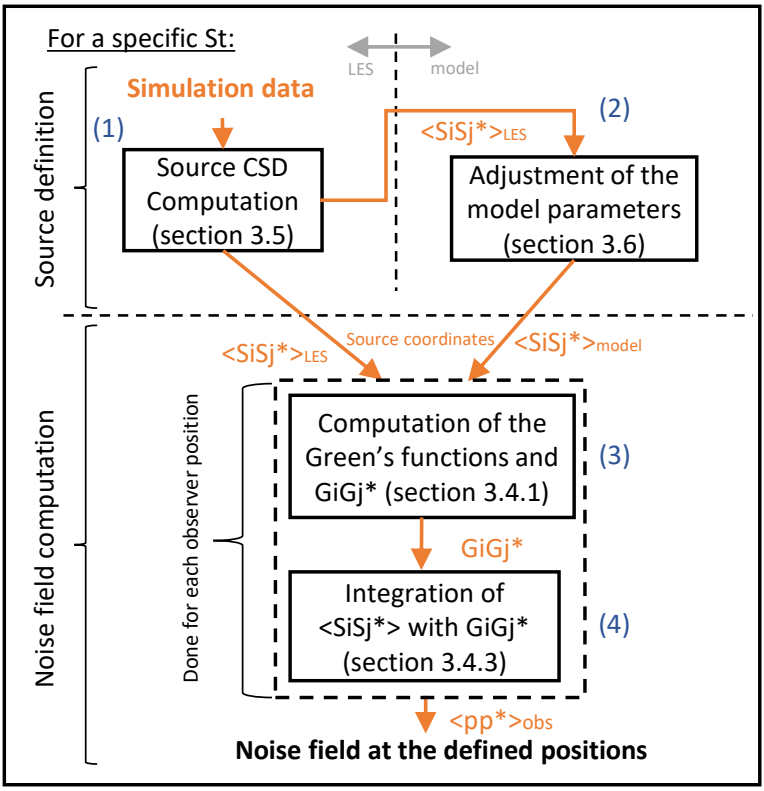

Figure 3.3 – Scheme of the solution procedure used in the present analysis.

4 NUMERICAL SIMULATION DATA

This chapter discusses the choice of a numerical database to be used in the present study. First, the prediction capabilities of a LBM-based commercial code are analyzed. The simulation model is presented and validated through comparisons with experimental data. The main difficulties and inconsistencies are discussed. Finally, an available LES database is chosen for the remaining analyses.

4.1 DEVELOPMENT OF A SIMULATION MODEL BASED ON LBM

4.1.1 Governing Equations

The solution of the discrete Boltzmann Equation for the particle distribution function f is linked to the use of a discrete set of particle velocities ξ_i. The used code, PowerFLOW v5.1, solves a variant of this equation:

$$\frac{\partial f_i}{\partial t} + \xi_i \frac{\partial f_i}{\partial \mathbf{x}} = C_i = \frac{F_i - f_i}{\tau} \tag{4.1}$$

where the collision operator C_i is approximated using the Bhatnagar-Gross-Krook (BGK) collision model. This source term is actually a relaxation towards a discrete form of the Maxwell-Boltzmann equilibrium distribution function F_i, with collision time τ (FARES, 2006). Each subscript i refers to one direction in the discretized velocity space. The lattice Boltzmann model used in this work allows Mach numbers $M > 0.5$, by using an extended regularized form of the collision operator (LATT; CHOPARD, 2006; ZHANG *et al.*, 2006; GOPALAKRISHNAN *et al.*, 2016), which increases the code stability at higher Mach numbers.

The adopted numerical scheme uses a symmetric discretization of the velocity space according to the D3Q19 model. The magnitude and direction of each particle velocity vector is such that the distribution function can be advected from one node of a computational lattice to the neighboring points during a single time step, independently of the local grid refinement. When discretized for an equidistant lattice, considering the space

increment $\xi_i \Delta t$, the Lattice Boltzmann Equation is obtained in the following form:

$$f_i(\mathbf{x} + \xi_i \Delta t, t + \Delta t) = f_i(\mathbf{x}, t) + \frac{\Delta t}{\tau}(F_i(\mathbf{x}, t) - f_i(\mathbf{x}, t)), \quad (4.2)$$

in which the equilibrium function is approximated up to third order,

$$F_i = \rho w_i \left[1 + \frac{\xi_i \cdot \mathbf{u}}{T_l} + \frac{(\xi_i \cdot \mathbf{u})^2}{2T_l^2} - \frac{(\mathbf{u})^2}{2T_l} + \frac{(\xi_i \cdot \mathbf{u})^3}{6T_l^3} - \frac{(\xi_i \cdot \mathbf{u})}{2T_l^2}\mathbf{u}^2\right]. \quad (4.3)$$

The weighting factors w_i, according to the D3Q19 scheme, are equal to 1/3 for the rest particles, 1/18 for the 12 bi-diagonal directions and 1/36 for the 6 coordinate directions. The lattice temperature is T_l, the relaxation time τ is related to the kinematic viscosity $\tau = \nu/T_l + \Delta t/2$ and its value is limited to a maximum in order to enhance code stability (FARES, 2006). The solver is also coupled with an entropy solver similar to that presented by Nie *et al.* (2009), Lew *et al.* (2014). The equation of the entropy s is solved by,

$$\partial_t s + u_\alpha \partial_\alpha s = -\frac{1}{\rho T_l}\partial_\alpha q_\alpha + \frac{\Phi}{\rho T_l} \quad (4.4)$$

where $s = c_v \ln[T/\rho^{\gamma-1}]$, c_v is the specific heat at constant volume and γ the ratio of specific heats, q_α is the heat flux and Φ the viscous dissipation function (NIE *et al.*, 2009). This equation is solved with a Lax-Wendroff finite difference scheme.

Each cubic volume of the mesh is called a *Voxel*. The grid refinement is defined by creating regions of Variable Resolution (VRs), which scale between each other by a factor of 2. Calculations in the VR transitions boundaries are done by a grid refinement algorithm described in (CHEN *et al.*, 2006), which was developed in order to satisfy conservation laws.

For high Reynolds number flows, the schemes use a turbulence modeling approach. In this approach, large scales are directly simulated, while the contribution of unsolved scales are accounted by means of an eddy viscosity model. In this case, the molecular relaxation time is replaced by an effective turbulent relaxation time, including the eddy viscosity effects. The turbulence model used is a modification of the two-equation

renormalization group (RNG) $k - \epsilon$ (TEIXEIRA, 1998; FARES, 2006).

The corrected relaxation time scale is,

$$\tau_{eff} = \tau + C_{\mu} \frac{k_t^2/\epsilon}{(1+\tilde{\eta}^2)^{1/2}}, \tag{4.5}$$

where C_{μ} is a turbulence model constant and $\tilde{\eta}$ is a combination of a local strain, local vorticity and local helicity parameters (HABIBI *et al.*, 2013).

Eddy viscosity values are reduced as a function of the local vorticity and shear rate, allowing structures that can be resolved by the grid to be developed and persist without numerical damping (CASALINO *et al.*, 2014b). The turbulence model equations are solved in the same grid as the LBM, but with a modified Lax-Wendroff explicit second order finite difference scheme (FARES, 2006).

A no-slip boundary condition is applied to the solid boundary surfaces by imposing a bounce-back rule on a volumetric scheme from Chen *et al.* (1998). Linear interpolation and weighted averaging ensures mass and momentum conservation. The numerical scheme also uses a wall model for boundary layers at high *Re* numbers (CASALINO *et al.*, 2014b), which is an extension of the standard wall functions from Launder and Spalding (1974).

The acoustic field is computed using the permeable/porous formulation of Ffowcs Williams-Hawkings (FW-H) surface integral method (DI FRANCESCANTONIO, 1997). This approach differs from the original (FFOWCS WILLIAMS; HAWKINGS, 1969) by the fact that the volume integrals, corresponding to quadrupole sources, can be neglected when an arbitrary shaped permeable surface enclosing the important source region is considered. The contribution of the enclosed sources inside the surface is computed by the pressure and velocity fluctuations that reach the permeable surface. This procedure allows the storage of data (pressure, velocity, density) in a surface, instead of a computational volume, thus reducing computational cost. Details of the formulation used in this work can be found in Najafi-Yazdi *et al.* (2010), Brès *et al.* (2010).

4.1.2 Solution Domain and Boundary Conditions

The nozzle geometry, the surfaces for data acquisition and several mesh refinement regions or VRs (Variable Resolution) compose a box-shaped computational domain of dimensions $490D \times 480D \times 480D$. The origin of the coordinate system is positioned at the nozzle exit, and the x axis is aligned with the jet axis. Several concentric boxes and cylinders form the rest of the simulation domain in which the VRs coarsen in the divergent direction in order to help acoustic wave damping. In the outer part, sponge layers are positioned between the VR transitions, where the damping coefficient in each layer is defined by an exponential law. In these regions, the viscosity value is increased in order to avoid reflections as the outgoing waves reach the outer boundaries. A close view of the nozzle region is shown in Figure 4.1, where the jet dynamics are calculated and the most refined VRs are located. The FW-H surface is shown in the same figure. No-slip conditions were considered at the solid walls, while a total pressure inflow boundary condition was applied to the nozzle inlet. The refinement level is defined by a parameter called resolution, $Res = D/\Delta x$, which defines the element pitch Δx for the most refined VR. The number of used VRs and Resolution value depend on the configuration of the employed grid. This information is shown in Table 4.1.

Table 4.1 – Summary of the parameters of the used computational grids.

Grid #	Voxels	Res	VRs
$M1$	2.97×10^8	195	12
$M2$	5.99×10^8	256	12
$M3$	2.49×10^8	763	14
$M4$	6.65×10^8	1024	14

In order to obtain desirable levels of resolved turbulence in the boundary layer and nozzle exit, an strategy of boundary layer tripping was applied. This approach is justified as in the experiment itself, the nozzle boundary layer was tripped in order to trigger transition to turbulence and hence reaching a turbulent velocity profile. A ring geometry was positioned inside the nozzle, after the convergent section, at $2.7D$ from the nozzle exit, in the

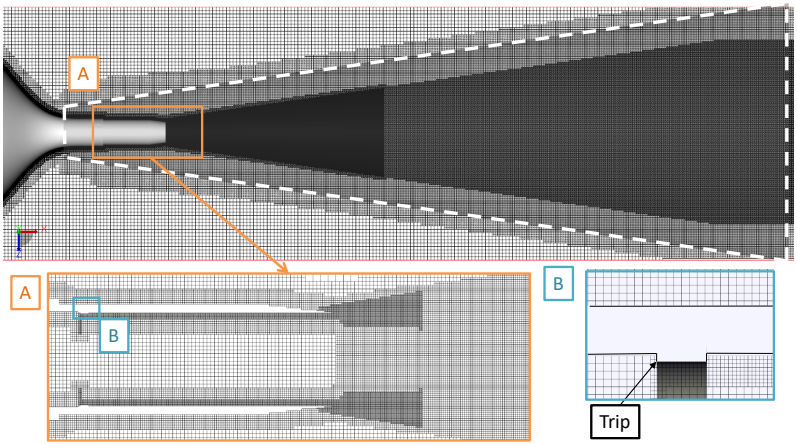

Figure 4.1 – xy plane view of the simulation domain showing the VR scheme. Computational grid in the region close to the nozzle [A]. Grid refinement around the tripping ring [B]. FW-H surface is represented by the white dashed line.

same position as the experiment. The thickness of the ring was $0.012D$.

The FW-H permeable surface for the isolated jet case has the shape of a tapered cylinder with closed ends, extending axially from $x = -10D$ to $x = 30D$. The surface data acquisition period was $\Delta t_{sim} U_J/D = 416$ with sampling frequency corresponding to $St = 22$. The simulation starts as a nozzle discharge in a stationary medium. Hence, data acquisition begins after the initial transient of the jet, determined by sensitivity tests. The total acquisition time was chosen in order to achieve desirable jet statistics convergence. Discrete Fourier Transform (DFT) was applied using Hanning windowing obtaining SPL spectra with resulting $St = 0.037$ bandwidth.

4.1.3 Preliminary results for M=0.4

4.1.3.1 Jet symmetry and use of Boundary layer Tripping

First, two values of grid resolution were used: 195 and 256, corresponding to $M1$ and $M2$ of Table 4.1. It was difficult to achieve a jet flow with significant levels of resolved turbulence

when no boundary layer (BL) tripping was used. Figure 4.2(a) shows isosurfaces of vorticity at $St = 3.5$ colored by contours of eddy viscosity. We can observe that the resulting jet showed a lack of circumferential homogeneity near the nozzle exit. Higher levels of eddy viscosity represent regions were a smaller part of the turbulent energy is directly solved, since the turbulence model is activated. The use of boundary layer tripping forced the direct resolution of turbulent fluctuations, reducing the eddy viscosity that could damp the formation of transient structures in previous cases. As a consequence, the azimuthal homogeneity was also improved, although not completely solving the problem (see Figure 4.2(b)).

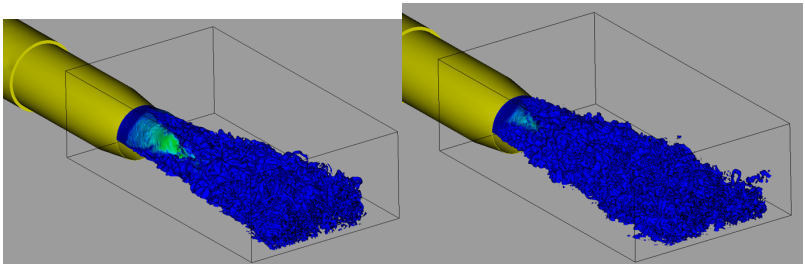

(a) No BL tripping (b) BL Tripping

Figure 4.2 – Instantaneous isosurfaces of vorticity colored by contours of eddy viscosity.

Such asymmetry is also observed in the boundary layer velocity profiles depicted in Figure 4.3(a), where h is the distance to the wall and the velocity U is normalized by the jet maximum velocity U_J. Profiles taken in different azimuthal slices in the nozzle exit present disparities between each other. Moreover, the velocity profile at $\phi = 90°$ shows considerable deviations from the experiments. The lack of axisymmetry is more evident in the resolved turbulence profiles (Figure 4.3(b)). Results showed an over prediction of turbulence levels in the boundary layer at some azimuthal position and underprediction at other positions. Such deviations may play an important role in the prediction of SPL levels (BOGEY; BAILLY, 2010; BOGEY *et al.*, 2012a; BOGEY *et al.*, 2012b; BRÈS *et al.*, 2015).

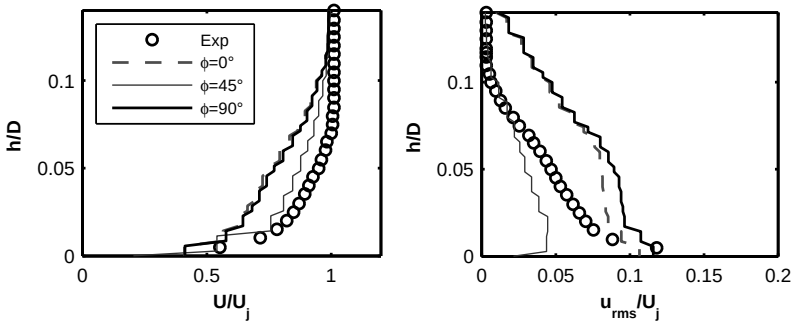

(a) (b)

Figure 4.3 – Comparison of layer profiles in different azimuthal positions measured next to the nozzle exit for $M = 0.4$ and $M2$ grid.

Aiming to solve these problems, a third grid configuration, designated by M3 in Table 4.1, was designed with the aid of the code developer. The domain is now composed from 14 VRs, where the most refined ones are positioned at the nozzle exit and around the tripping geometry. Figure 4.4 shows the refinement regions and highlight the different refinement around the ring geometry. The mesh modifications improved the circumferential homogeneity of the jet flow. Nozzle exit profiles are shown in Figure 4.5. Although significant advances could be observed in comparison to the results from the $M2$ grid, both mean and rms velocity profiles differ at different azimuthal slices. This is a possible drawback of using a regular Cartesian grid, with constant aspect ratio for each Voxel, for a round nozzle. As result, the grid refinement is also not homogeneous in the nozzle circumference, what is a possible cause for the observed inconsistency.

Figure 4.6 depicts the PSD profiles from axial velocity fluctuations at the centerline for $St = 0.2$, 0.4 and 0.6. According to Batchelor and Gill (1962), the axisymetric mode is the only one with non-zero axial velocity at the centerline. Although the trends in the development of the axisymmetric mode were reasonably captured, the numerical simulation overpredicted the fluctuation levels up to $x/D = 6$. Comparing $M2$ and $M3$, we can observe an improvement in the prediction at $St = 0.4$ for the latter.

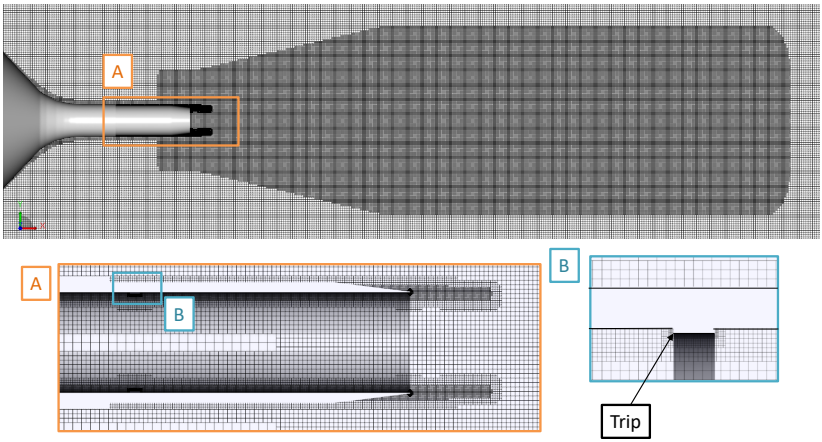

Figure 4.4 – xy plane view of the simulation domain showing the VR scheme for M3. Computational grid in the region close to the nozzle [A]. Grid refinement around the tripping ring [B].

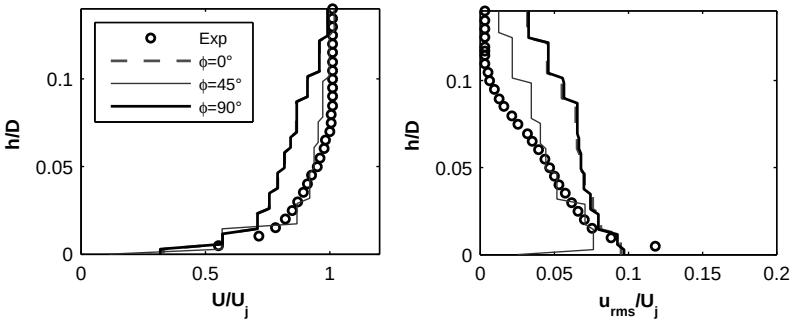

(a) (b)

Figure 4.5 – Comparison of boundary layer profiles in different azimuthal positions measured next to the nozzle exit for $M = 0.4$ and $M3$ grid. Experimental data from Cavalieri *et al.* (2013).

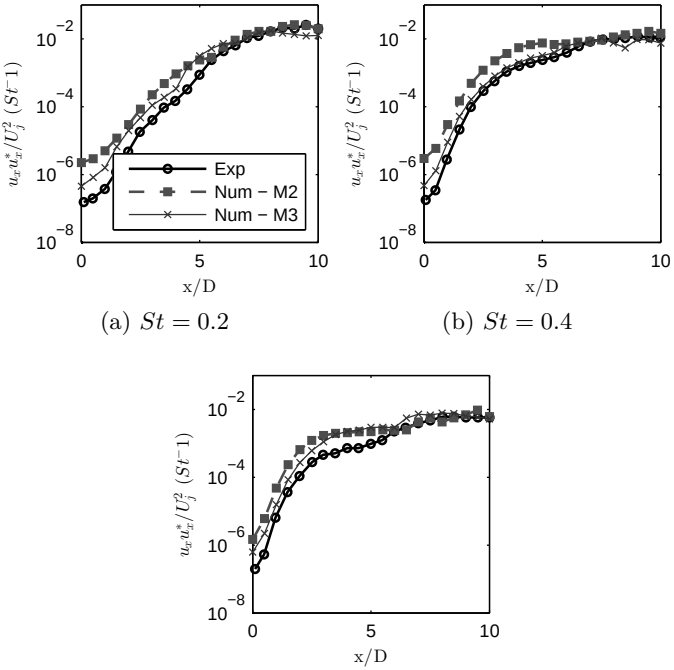

(a) $St = 0.2$ (b) $St = 0.4$

(c) $St = 0.6$

Figure 4.6 – Power spectral density of axial velocity fluctuations at the centerline for three different St. Experimental data from Cavalieri *et al.* (2013)

Mean velocity profiles in the jet plume were also obtained. Good agreement with experiments was achieved for the mean axial velocity at the centerline and at radial slices at $x/D = 2$ and $x/D = 4$ (Figure 4.7 (a), (b) and (d) respectively). The radial u_{rms} profile at $x/D = 2$ was also well reproduced by the simulation (Figure 4.7(c)). Radial profiles of the PSD of the axial velocity fluctuations are also compared to experimental data in Figure 4.8 at $x/D = 2.5$, 4 and 5 and $St = 0.4$ and $St = 0.5$. Good agreement with experimental profiles was observed, showing a consistent development of the jet flow. Spectra of the fluctuating velocity for two points at the centerline are shown in Figure 4.9. Numerical results presented higher levels for the whole St range for both analyzed points.

The lack of axisymmetry of the boundary layer profiles at the nozzle exit as well as the discrepancies with experimental results at the jet centerline raise significant concerns regarding the use of these results for model calibration purposes. The use of a Cartesian grid for a cylindrical jet, as well as the turbulence modeling near the wall are potential causes for the found inconsistencies. The thickness of the ring used to introduce perturbations could also contribute as a source of errors. The impact on the sound field caused by these deviations from the experiments at the flow field is assessed in the next section.

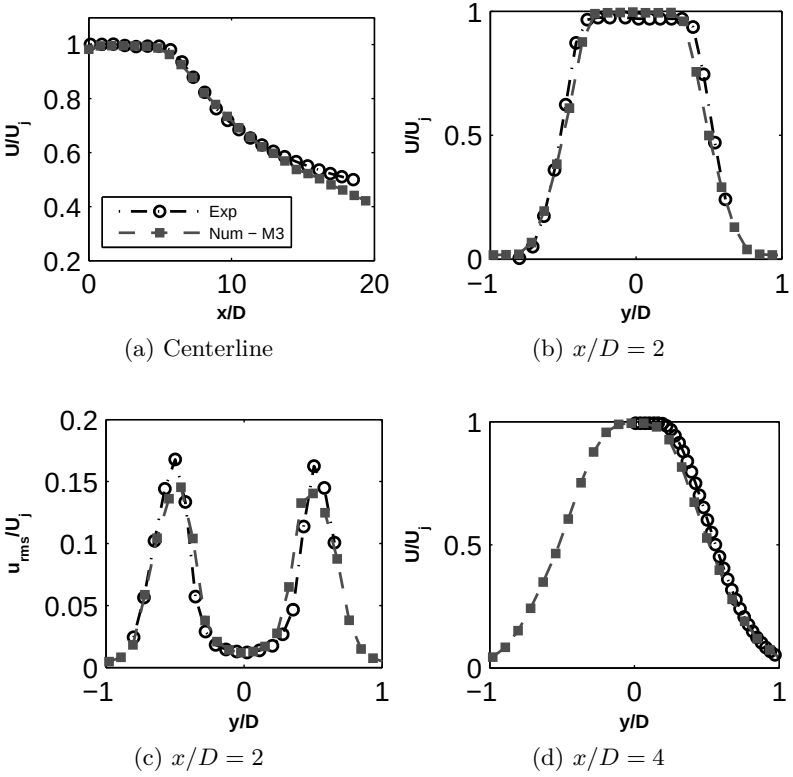

(a) Centerline (b) $x/D = 2$

(c) $x/D = 2$ (d) $x/D = 4$

Figure 4.7 – Mean flow axial velocity profiles for the $M = 0.4$ case. Experimental data from Cavalieri *et al.* (2013).

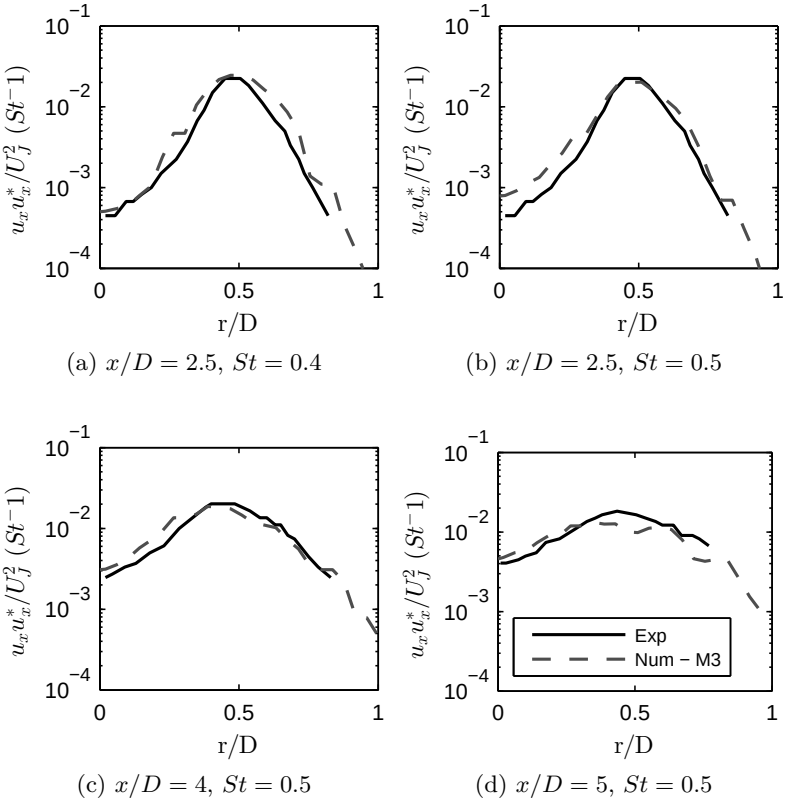

(a) $x/D = 2.5$, $St = 0.4$ (b) $x/D = 2.5$, $St = 0.5$

(c) $x/D = 4$, $St = 0.5$ (d) $x/D = 5$, $St = 0.5$

Figure 4.8 – Radial profiles of the PSD of axial velocity for the $M = 0.4$ case at different axial postions and St. Experimental data from Cavalieri *et al.* (2013).

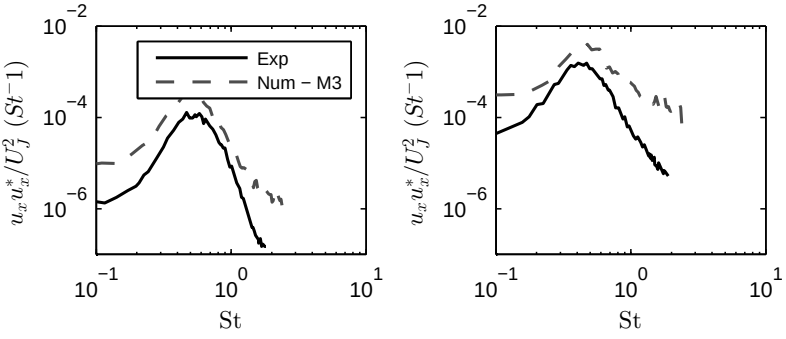

(a) $x/D = 2$ (b) $x/D = 4$

Figure 4.9 – Axial velocity spectra at two points at the centerline. Experimental data from Cavalieri *et al.* (2013).

4.1.3.2 Acoustic results

Acoustic results obtained with the same three grids are presented in Figure 4.10. There are significant differences between the coarse $M1$ and the fine $M2$ meshes. The third grid with wall refinement, $M3$, although globally coarser in the jet plume, presented results closer to $M2$. In general, reasonable agreement with experiment can be observed.

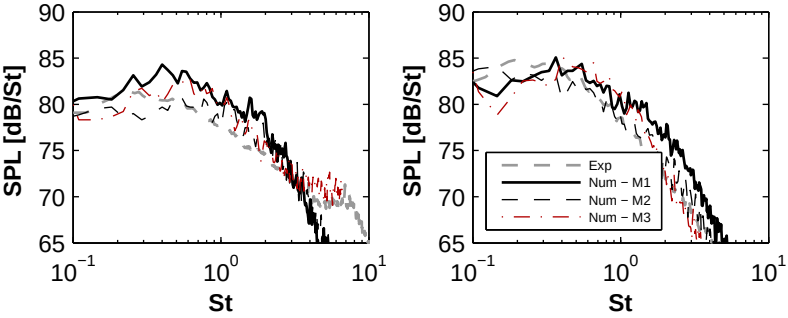

(a) $\theta_{obs} = 90°$ (b) $\theta_{obs} = 30°$

Figure 4.10 – Comparison of far-field spectra between experimental data and the used grids for $M = 0.4$.

Owing to its improved axisymmetry and better agreement with experiments at the centerline, comparison at other observer positions was done only with $M3$ (Figure 4.11). One can see that higher deviations from the reference data occurs bellow $St = 0.3$, specially at low polar angles. Levels were also overpredicted near $St = 1$. Maximum deviations were about $2 - 3$ dB. Directivity plots at specific St numbers are shown in Figure 4.12. Levels are underpredicted for $St = 0.2$. For $St = 0.3$, levels are underpredicted at angles smaller than 60° and overpredicted at higher angles. The directivity is well estimated only for $St = 0.4$.

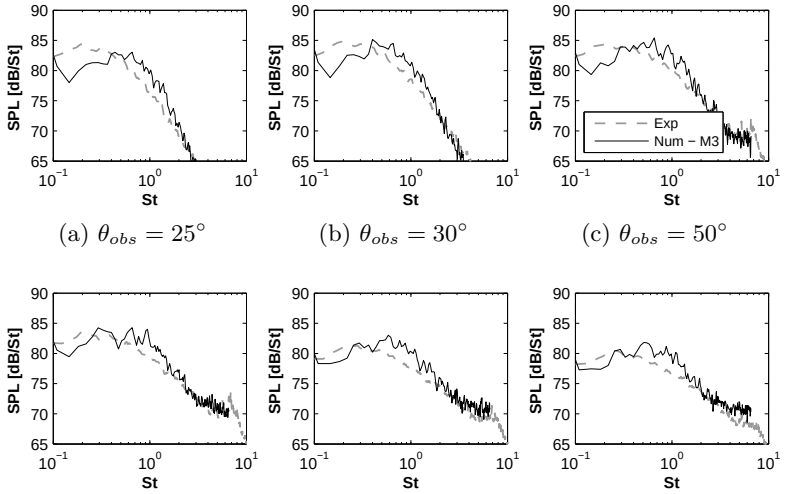

(a) $\theta_{obs} = 25°$ (b) $\theta_{obs} = 30°$ (c) $\theta_{obs} = 50°$

(d) $\theta_{obs} = 70°$ (e) $\theta_{obs} = 90°$ (f) $\theta_{obs} = 100°$

Figure 4.11 – Comparison SPL spectra at several polar positions ($M = 0.4$).

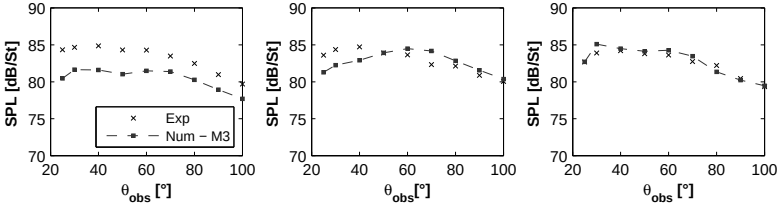

(a) $St = 0.2$ (b) $St = 0.3$ (c) $St = 0.4$

Figure 4.12 – Polar directivity plots at three different St ($M = 0.4$).

4.1.4 Results for M=0.9

In order to investigate the prediction capabilities of the method at higher Mach numbers, results for a Mach 0.9 jet are also analyzed using grid $M3$ and its more refined version $M4$. Mean velocity profiles at the centerline and lipline are depicted in figure 4.13 (a) and (c) respectively. The root mean square of velocity fluctuations is shown in Figures 4.13 (b) and (d). The trends at the centerline changed with grid refinement and results deviate more significantly from the experimental data. Turbulent intensities are underpredicted at both the lipline and centerline. Nozzle exit profiles are depicted in Figure 4.14. Although the profiles are now more homogeneous, they differ significantly from the experiments.

Noise spectra at the observer positions are shown in Figure 4.15. Results are not in good agreement with experimental data and they do not differ significantly between the different grid refinements. Deviations for low St are even more significant than those found for the $M = 0.4$ case. The predicted directivity trends depicted in Figure 4.16 are poor, except for $St = 0.3$. We should keep in mind that this Mach number is in the upper threshold capability of the current code version. Nevertheless, the predicted values for high subsonic Mach numbers diverge significantly from the experimental values and, for this reason are not adequate for the proposed analysis.

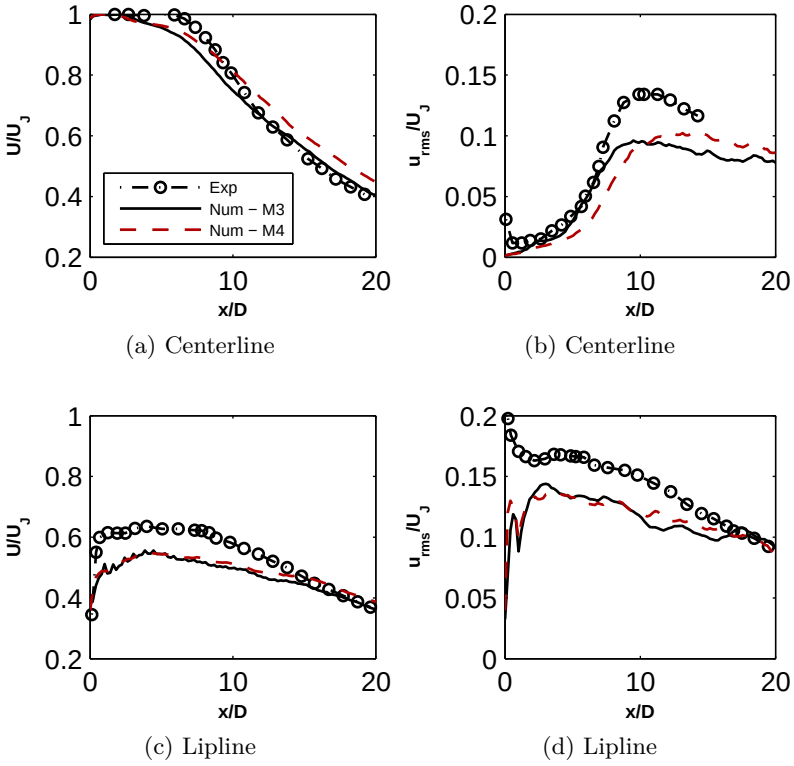

(a) Centerline (b) Centerline

(c) Lipline (d) Lipline

Figure 4.13 – Mean flow axial velocity profiles at centerline and lipline for the $M = 0.9$ case. Experimental data taken from Brès *et al.* (2015).

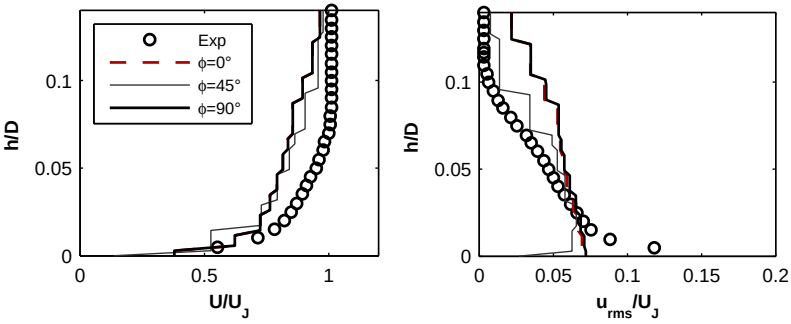

(a) (b)

Figure 4.14 – Comparison of boundary layer profiles at different azimuthal positions, obtained with the LBM approach, measured next to the nozzle exit for $M = 0.9$ and $M3$ grid. Experimental data from Cavalieri *et al.* (2013).

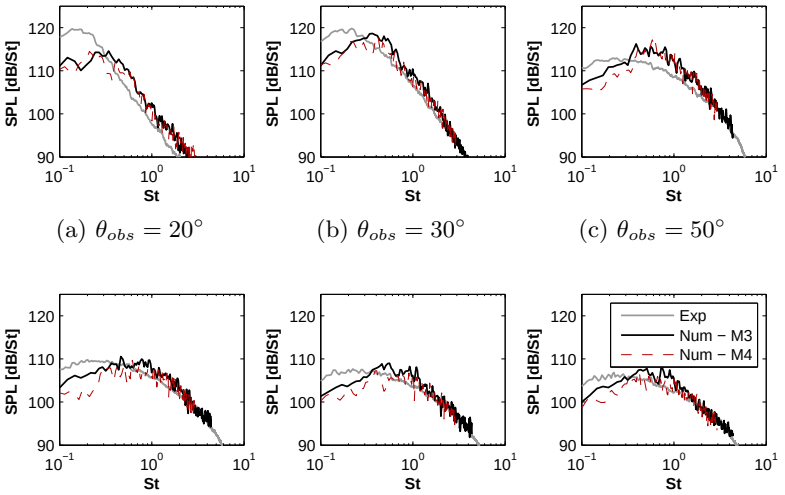

(a) $\theta_{obs} = 20°$ (b) $\theta_{obs} = 30°$ (c) $\theta_{obs} = 50°$

(d) $\theta_{obs} = 70°$ (e) $\theta_{obs} = 90°$ (f) $\theta_{obs} = 100°$

Figure 4.15 – Comparison SPL spectra, obtained with the LBM approach, at several polar positions ($M = 0.9$).

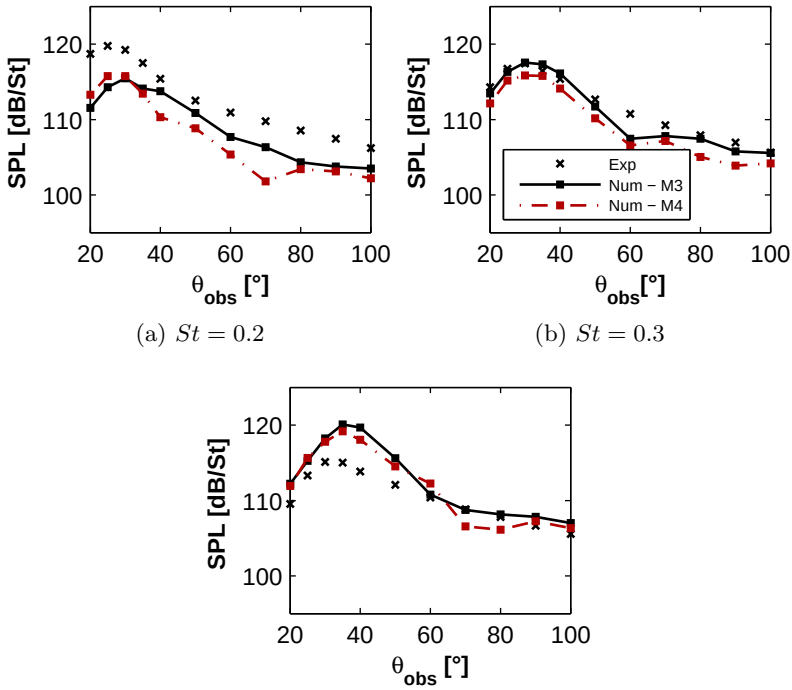

(a) $St = 0.2$ (b) $St = 0.3$

(c) $St = 0.4$

Figure 4.16 – Polar directivity plots at three different St obtained with the LBM approach ($M = 0.9$).

4.1.5 Final considerations about the LBM simulations

Although the obtained results could be considered acceptable in an industry context, they are not reliable enough for this fundamental study. A correct prediction of the boundary layer profiles was already shown to be a key factor for the prediction of jet noise (BRÈS *et al.*, 2015; BOGEY; BAILLY, 2010; BOGEY *et al.*, 2012a; BOGEY *et al.*, 2012b). In fact, the considerable deviations and lack of circumferential homogeneity at the nozzle exit, even with grid refinement, are important limitations of the adopted approach. Moreover, the simulations overpredicted the PSD levels of the axisymmetric mode, which is the main focus of this study. Prediction of the sound-field and directivity were not

sufficiently accurate. Results for $M = 0.9$ were clearly worse, considering that even the mean velocity profiles could not be well captured. The analysis proposed herein requires results with enough accuracy to allow meaningful adjustments in the parameters of the simplified models.

Running finer meshes, with longer simulation times to enhance the convergence of the statistics, could be a possible next attempt to improve the results. However, the short period of time left to conclude the present work made it difficult to conduct these analysis.

4.2 LES DATABASE

The mentioned difficulties with the LBM simulations, led to the decision of using other numerical database. In this respect, the LES results obtained by Brès *et al.* (2015)[1], using the compressible flow solver "Charles", appear to be a good option. The high fidelity simulation includes the nozzle geometry and the authors imposed synthetic perturbations on the boundary layers in order to match the nozzle exit profiles. This resulted in a very good agreement with the sound-field experimental data. Not only the results were very good, but also the long available time data (about 2000 convective units) provides very good convergence of the statistics. This is an important requirement for accurate computation of the cross spectral densities of the source field.

The same nozzle geometry described in Chapter 3 was simulated by Brès *et al.* (2015) with Mach 0.9, $Re = 10^6$ and isothermal conditions. The code is based on unstructured grids and an isotropic mesh refinement was used near the internal walls. Turbulent wall modelling was also used (KAWAI; LARSSON, 2012; BODART; LARSSON, 2011; BODART; LARSSON, 2012). The results considered in this study came from a mesh with 15.9×10^6 elements. The results were interpolated onto a cylindrical grid extending $0 \leq x/D \leq 30$ and $0 \leq r/D \leq 6$, with 626 points in the axial direction, 138 in the radial and 128 in the azimuthal direction. The total time length $t_{sim}c/D = 2000$ was sampled at $\Delta tc/D = 0.2$.

[1] The LES study was performed at Cascade Technologies, with support from NAVAIR SBIR project, under the supervision of Dr. John T. Spyropoulos. The main LES calculations were carried out on DoD HPC systems in ERDC DSRC.

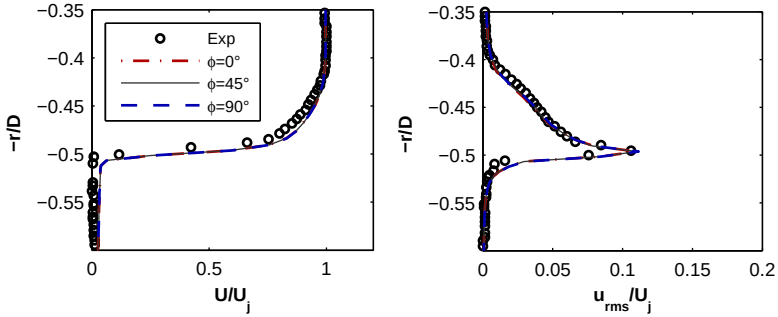

Figure 4.17 – Comparison of the LES boundary layer profiles at the nozzle exit. Adapted from Brès *et al.* (2015)

More information about the simulation and its validation can be found in Brès *et al.* (2014), Brès *et al.* (2015) and Brès *et al.* (2016). Some of the results are reproduced here. Figure 4.17 shows the comparison between the boundary layer profiles. These results highlight the circumferential homogeneity of the near-wall flow and are also in very good agreement with the experimental data. Figure 4.18 depict the comparison of experimental and LES noise spectra, the simulation results showed very good agreement with experimental data, with very good reproduction of the spectral shapes and directivity. Both the flow-field and acoustic results support the choice of the LES database in opposition to the LBM model presented in the previous sections.

The next chapter deals with the extraction of the Lighthill's source term from the numerical data. The contribution of the $m = 0$ linear part of T_{xx} to the sound field is assessed.

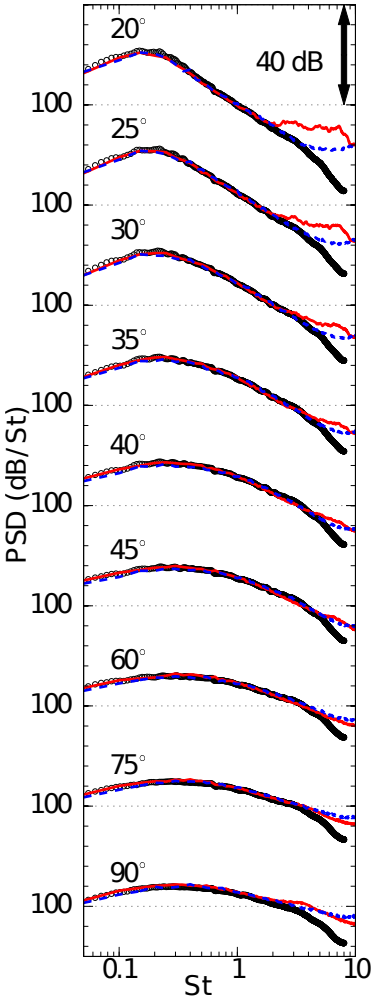

Figure 4.18 – Comparison of the noise spectra from experiment (∘) and LES grids with 15.9×10^6 elements (—-) and 69×10^6 elements (– – –). Reproduced from Brès *et al.* (2015)

5 ANALYSIS OF LES SOURCES

This chapter is dedicated to explore the simplified source term from the LES data (equation 3.5) and its derived sound field. Before showing the final results and discussion, a few preliminary sections aim at exploring the sensitivity of the model to some parameters involved in the data analysis, such as the window size and attenuation function. Analyzed St numbers were 0.2, 0.3, 0.4 and 0.75. The reasons for choosing these Strouhal values (except for $St = 0.4$) were based on the relevant range for installation noise and to avoid the contamination by the presence of trapped acoustic waves inside the potential core (see Towne *et al.* (2017), Schmidt *et al.* (2017), Jaunet *et al.* (2016)). Only $St = 0.4$ is in this range. Source levels are plotted in terms of non-dimensional values, by using the reference $\rho_0 U_J^2$.

5.1 WINDOWING ANALYSIS

The linearized T_{xx} source term, based on mode $m = 0$, was first extracted from the LES results and propagated by the integration with the free-field Green's function (Equation 3.28). In Figure 5.1 results for $St = 0.3$ and 0.75 are compared to two sets of experimental data from Piantanida *et al.* (2016b): the total noise at the far-field, represented by ($\times$), and the $m = 0$ sound field, represented by ($\circ$). The decomposition of the sound field in azimuthal Fourier modes follows Equation 5.1. As already known, the axisymmetric mode is dominant at low angles, while the contribution of higher order modes is important at high angles. The observed differences in levels between both experimental sets of data are consequence of this fact. From now on, only $m = 0$ experimental data is shown for the free jet case, while the complete set of azimuthal modes is used for the installed case.

$$p(r_{obs}, \theta_{obs}, m, t) = \frac{1}{2\pi} \int_{-\pi}^{\pi} p(r_{obs}, \theta_{obs}, \phi_{obs}, t) e^{im\phi_{obs}} d\phi_{obs} \quad (5.1)$$

Two sets of numerical results are presented, one obtained from the FFT of the source with rectangular window and the other with Hanning window. Both considered a block size of Nfft= 256 points and overlap of 75%. The CSD obtained with Hanning window was scaled using a factor of 8/3. One can clearly

note the differences in levels and directivity caused by the different windows, which occurred for both St values. Before any comparison to the experimental data, this issue should be further explored. This is done in the next sections.

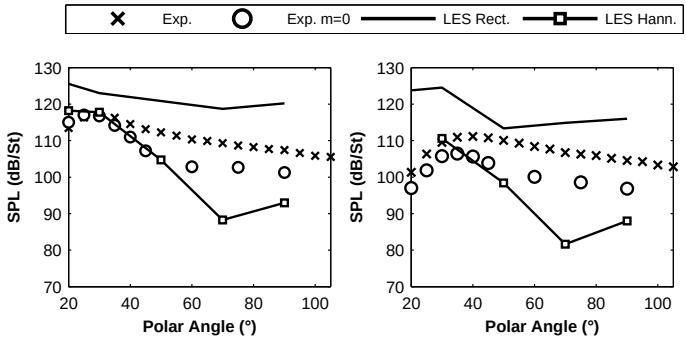

(a) $St = 0.3$ (b) $St = 0.75$

Figure 5.1 – Sound Pressure Level (SPL) results for free-field Green's function and two St numbers.

In order to help understanding such differences on the numerical results above, plots of the PSD and CSD of the source with and without use of the Hanning time window are compared in Figures 5.2 and 5.3 for different radial and axial distances of reference. Although some differences between results can be observed in the presented plots, it is not evident that they could cause the observed deviations in the noise field.

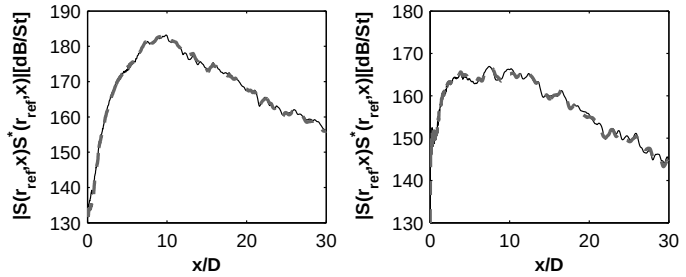

(a) Centerline (b) Lipline

Figure 5.2 – PSD of the source term for $St = 0.3$ using different windows in time. (—) Rectangular window, (- - - -) Hanning window.

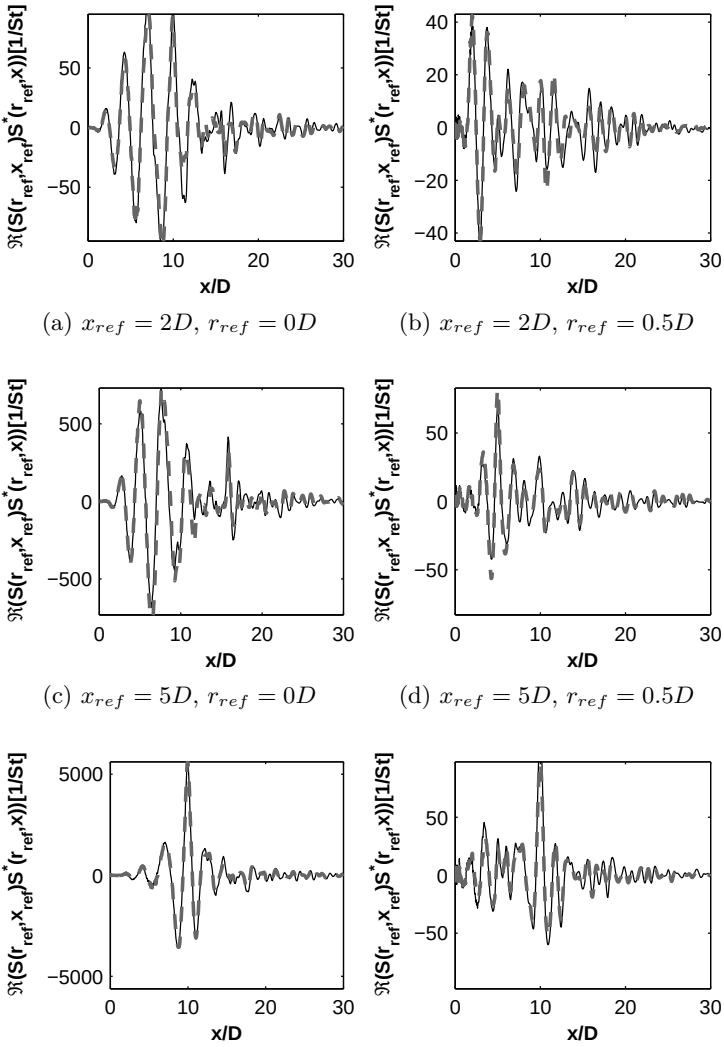

(a) $x_{ref} = 2D$, $r_{ref} = 0D$ (b) $x_{ref} = 2D$, $r_{ref} = 0.5D$

(c) $x_{ref} = 5D$, $r_{ref} = 0D$ (d) $x_{ref} = 5D$, $r_{ref} = 0.5D$

(e) $x_{ref} = 10D$, $r_{ref} = 0D$ (f) $x_{ref} = 10D$, $r_{ref} = 0.5D$

Figure 5.3 – Real part of the CSD of the source term for $St = 0.3$ using rectangular and Hanning windows in time. (—) Rectangular window, (- - - -) Hanning window.

5.1.1 Spatial discretization

The previous results were obtained by an integration with only 10 points in azimuth. In other to test the sensitivity to this aspect, other results obtained with 30 points were also considered. The comparison is depicted in Figure 5.4 and shows no significant changes with the azimuthal discretization.

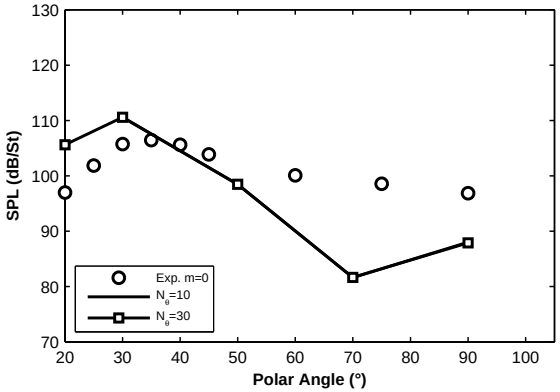

Figure 5.4 – Effect of azimuthal discretization for $St = 0.75$. Results obtained using the Hanning window.

The original LES data is contained in a cylinder with dimensions $r_{dom} = 6D$, $x_{dom} = 30D$ with 656 points in the axial, 138 in the radial and 128 in the azimuthal directions. In order to reduce the computational time, some of the results shown in this document were obtained in a reduced domain extending up to $r_{dom} = 3D$ and $x_{dom} = 30D$ with 328 points in the axial and 58 in the radial directions. The comparison between the results of both grids are shown in Figure 5.5 and only minor differences are observed.

Due to the considerations for transferring the derivatives to the Green's function (Equation 3.28), the source field should present zero amplitudes at the boundaries. In order to assure that, and avoid errors caused by the truncation of the domain, a window function similar to the one used by Martínez-Lera and Schram (2008), Nogueira *et al.* (2016b) was applied in space.

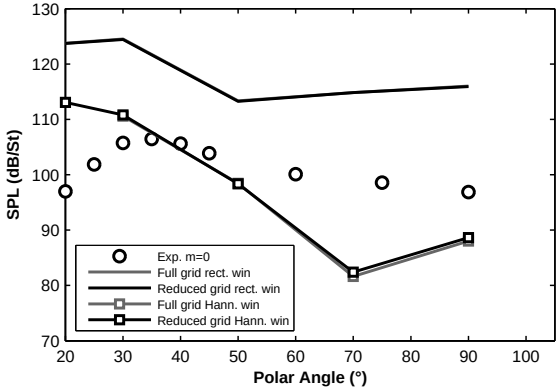

Figure 5.5 – Results comparing the full LES grid with the reduced grid.

5.1.2 Sensitivity to the Nfft parameter

In addition to the chosen Nfft=256 value, four other values were considered: 128, 512, 1024 and 2048. Results are shown for each window function in Figures 5.6 and 5.7 for $St = 0.3$ and 0.75 respectively. All the considered window functions are depicted in Figure 5.6(d). In addition to the ones mentioned above, the functions used by Freund (2001) and Bodony and Lele (2008) were also considered. Both are defined by the hyperbolic tangent functions in Equation 5.2 for a signal in the range $t_0 \leq t \leq t_f$:

$$w_t = \frac{1}{2}\left[\tanh\left(\frac{5(t-t_1)}{(t_1-t_0)}\right) + \tanh\left(\frac{5(t_2-t)}{(t_f-t_2)}\right)\right], \qquad (5.2)$$

where $t_1 = \eta(t_f - t_0) + t_0$ and $t_2 = (1-\eta)(t_f - t_0) + t_0$, with η defined as 5% as used by Freund (2001) and 20% as in Bodony and Lele (2008).

In Figure 5.6(b), the Hanning window results showed convergence of the noise levels within 1dB for all the Nfft values, but 512. It is not clear why this specific value resulted in this higher deviation. The results with rectangular window (Figure 5.6(a)) presented an undesirable dependence with the block size. The analyses with the weighting used by Freund (2001) are shown in Figure 5.6(c). We can see considerable differences for the lower Nfft values, but levels and directivity do converge to the same trends as the Hanning window with increasing Nfft.

In the case of $St = 0.75$ the sensitivity is even higher. The window function used by Bodony and Lele (2008) was also analyzed and showed similar trends to the Hanning results (Figure 5.7). Due to its convergence and similar results to the hyperbolic tangent windows, the Hanning window was chosen for the remaining analyses.

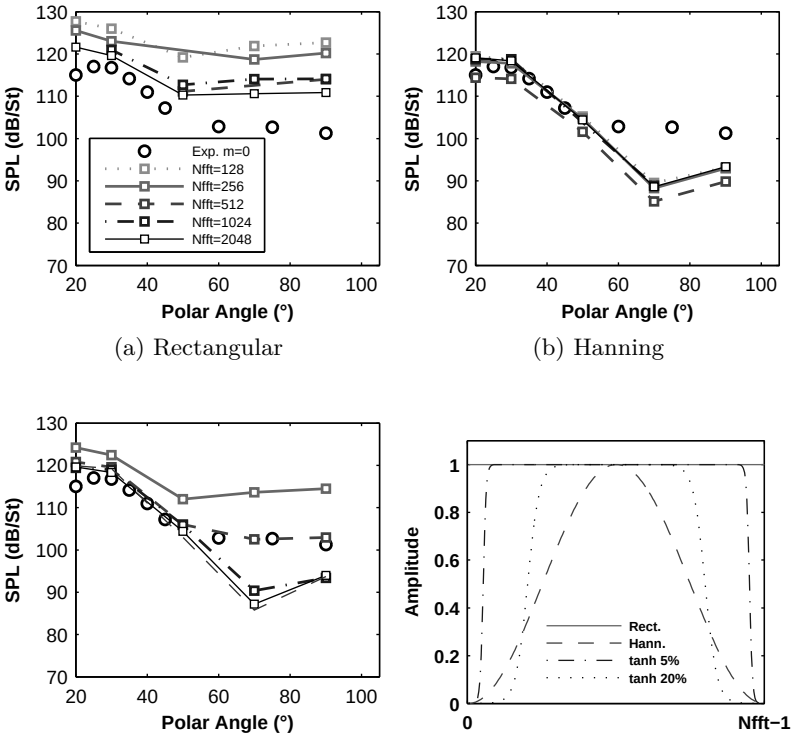

(a) Rectangular (b) Hanning

(c) Freund (2001) (d) Window functions

Figure 5.6 – Sound Pressure Level (SPL) results with several Nfft values for $St = 0.3$ and three window functions.

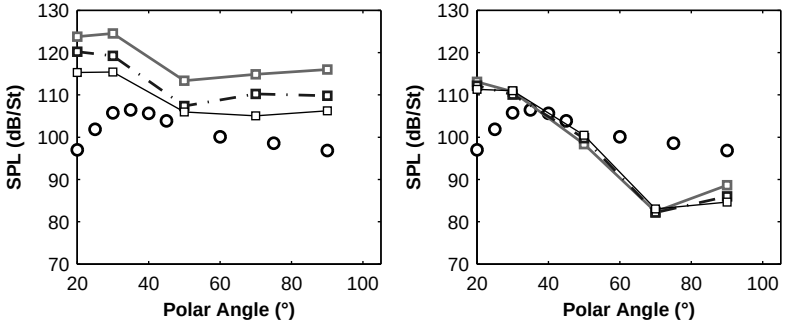

(a) Rectangular (b) Hanning

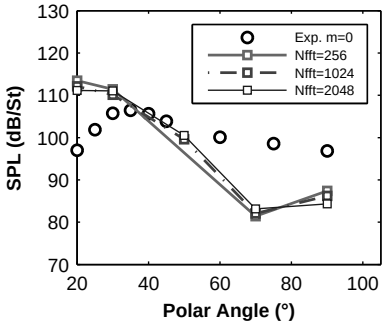

(c) Bodony (2008)

Figure 5.7 – Sound Pressure Level (SPL) results with several Nfft values for $St = 0.75$ for three window functions.

5.2 NOISE RESULTS FOR ISOLATED AND INSTALLED JETS

5.2.1 Isolated jet

Results obtained by integration with the free-field Green's function are shown in Figure 5.8 for $St = 0.2$, 0.3, 0.4 and 0.75. The results show very good agreement with the experimental data for $m = 0$ at low angles and St numbers, reproducing superdirectivity of the axisymmetric mode (CAVALIERI *et al.*, 2012). Although the agreement is indeed very good in this radiation direction for $St = 0.2$ (Figure 5.8(a)), levels are overpredicted at 20° and 30° for the other analyzed St.

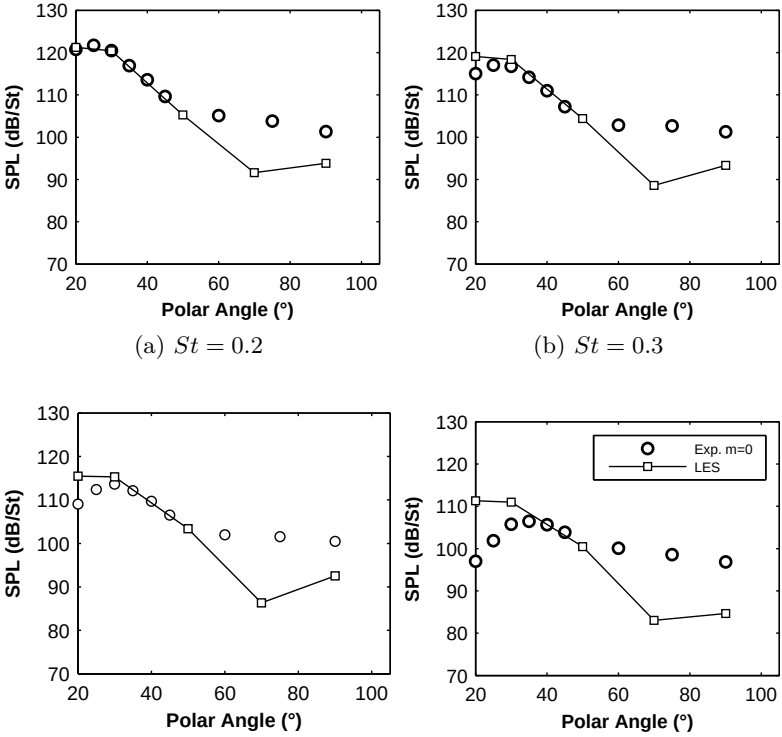

(a) $St = 0.2$ (b) $St = 0.3$

(c) $St = 0.4$ (d) $St = 0.75$

Figure 5.8 – Comparison of free jet results for the four considered St numbers.

Neglecting the entropy term in the definition of the source term could be an important issue for the observed overprediction, since Bodony and Lele (2008) identified a cancellation effect between the entropy and momentum terms for St bellow 0.3 at this radiation direction. Here, however, the deviation becomes larger with growing St, which is also aligned with the growing importance of refraction effects, neglected by the present approach. These deviations are expected to reduce once the complete Lighthill's tensor, with density fluctuations and non-linear terms, is taken into account.

Levels were underpredicted by about $10dB$, at angles higher than 60°. In these directions, both T_{rr}, T_{xr} and possibly non-linear terms may have significant contributions to total noise levels, but were not considered in this study (CRIGHTON, 1975). As already expected, more terms and more azimuthal Fourier modes should be accounted for when trying to predict noise at high angles for an isolated jet. In the sections to come, the role of the linear $T_{xx}(m = 0)$ is assessed for the edge scattering cases.

5.2.2 Installed jet: Plate at $r/D = 1$

As the trailing-edge scattering is not significant at high St, the analyses are limited to $St \leq 0.4$. The plate is now represented by a tailored Green's function for a semi-infinite plane (FFOWCS WILLIAMS; HALL, 1970). In this first case, the plate is positioned at $r/D = 1$ (measured from the jet centerline).

Figure 5.9 depicts the results for the installed case for azimuthal angle $\phi_{obs} = 260°$, in the unshielded side of the plate (See Figure 3.1). At the region dominated by the edge scattering, levels were very close to the experimental total noise (all modes), with larger deviations found for $St = 0.4$ in Figure 5.9(c). This suggests the dominance of the mode $m = 0$ and T_{xx} for installed jet noise, which agrees with the observations of Cavalieri *et al.* (2014) and Nogueira *et al.* (2017). This observation supports the work to be presented in the following chapter, where a simplified T_{xx} wavepacket source model is adjusted to predict the noise field.

Results for two other azimuthal positions are shown in Figure 5.10 for $\phi_{obs} = 220°$ and Figure 5.11 for $\phi_{obs} = 180°$. For $St = 0.2$ and 0.3 in Figure 5.10(a) and (b), results are underpredicted by about $2 \sim 4dB$. We should bear in mind that at $M = 0.9$, installation effects are not so prominent as in low Mach number[1]. In this sense, in some radiation directions, the free jet can present noise levels comparable to the scattered field, hence the remaining terms and modes could have a small contribution at this position but are not considered in the analysis. Also, the differences between the actual finite plate and its representation by the semi-infinite plate must play a role for the observed deviations. The latter is supported by the presence of level oscillations with the polar angle in the experimental data, caused by the secondary

[1] Trailing edge scattering noise scales with U_j^5, while the free-jet noise with U_j^8, approximately

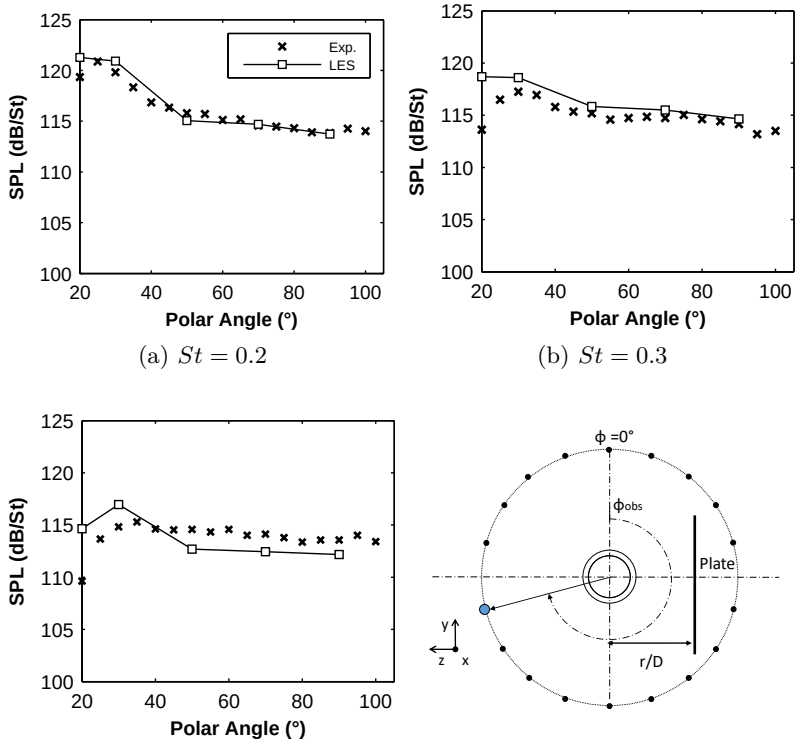

(a) $St = 0.2$ (b) $St = 0.3$

(c) $St = 0.4$ (d) Azimuthal Position

Figure 5.9 – Results obtained with the presence of the plate positioned at $r/D = 1$ for $\phi_{obs} = 260°$. Comparison between different St.

scattering by lateral edges (CAVALIERI *et al.*, 2014). Nevertheless, levels for $St = 0.4$ are underpredicted by about $10dB$. For this St number and observer positions, the missing terms should be even more important.

Minor scattering effects are expected in directions parallel to the trailing edge in the case of the semi-infinite plate. As a consequence, with the reduced installation effect, levels and directivity trends for $\phi_{obs} = 180°$ are more similar to those observed for the free jet. Therefore, the missing modes and momentum terms are also important. It is interesting however that

in Figure 5.11(a), for $St = 0.2$ and polar angle $\theta_{obs} = 90°$ levels are still very close to the experimental data.

Figure 5.12 shows a comparison of the noise levels with varying ϕ_{obs} and $\theta_{obs} = 90°$. The experimental data for the free-jet (all modes) is included in the comparison. As already commented, the installed jet noise levels are very similar to the free-jet levels in azimuthal directions close to $\phi_{obs} = 180°$. The used approach yields results closer to the installed jet experimental data in directions where the scattering effects are dominant over the free-jet noise.

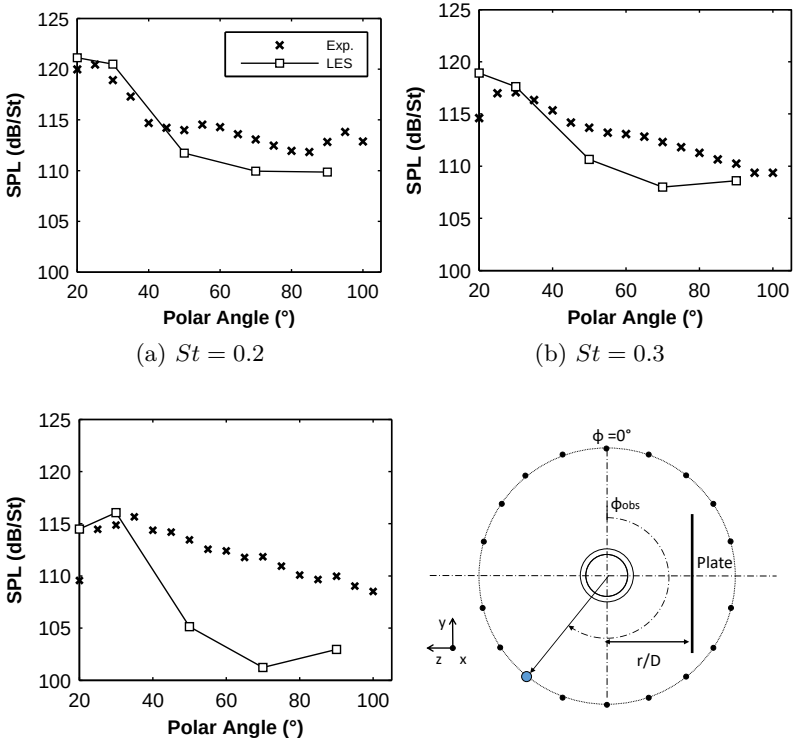

(a) $St = 0.2$ (b) $St = 0.3$

(c) $St = 0.4$ (d) Azimuthal Position

Figure 5.10 – Results obtained with the presence of the plate positioned at $r/D = 1$ for $\phi_{obs} = 220°$. Comparison between different St.

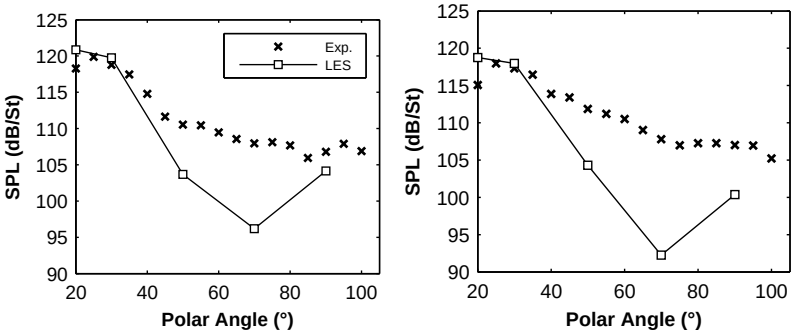

(a) $St = 0.2$ (b) $St = 0.3$

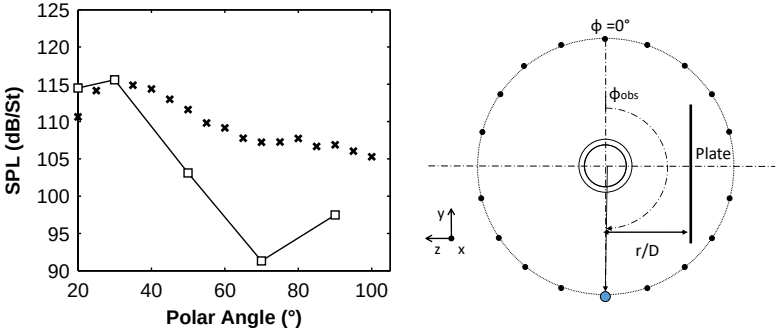

(c) $St = 0.4$ (d) Azimuthal Position

Figure 5.11 – Results obtained with the presence of the plate positioned at $r/D = 1$ for $\phi_{obs} = 180°$. Comparison between different St.

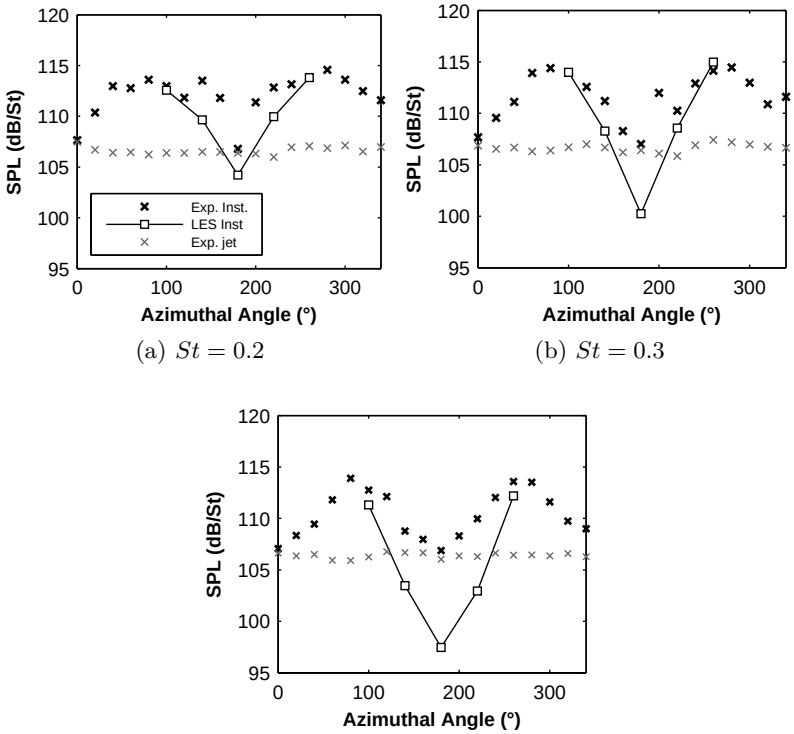

(a) $St = 0.2$ (b) $St = 0.3$

(c) $St = 0.4$

Figure 5.12 – Results for the the plate positioned at $r/D = 1$ at $\theta_{obs} = 90^{\circ}$ and varying azimuthal angle.

5.2.3 Plate at $r/D = 1.5$

When moving the plate away from the jet, say $r/D = 1.5$, reduction of the scattering effects is expected. Results for this case are shown in Figure 5.13, for $St = 0.2$ and 0.3 and $\phi_{obs} = 260°$ and $\phi_{obs} = 220°$. Although $T_{xx}(m = 0)$ seems to still dominate in the scattering noise regions for $\phi_{obs} = 260°$ (Figures 5.13(a) and (c)), some important source information is missing at $\phi_{obs} = 220°$ (Figure 5.13(b) and (d)). The same comments about the Mach number and reduction of the scattering noise levels apply here.

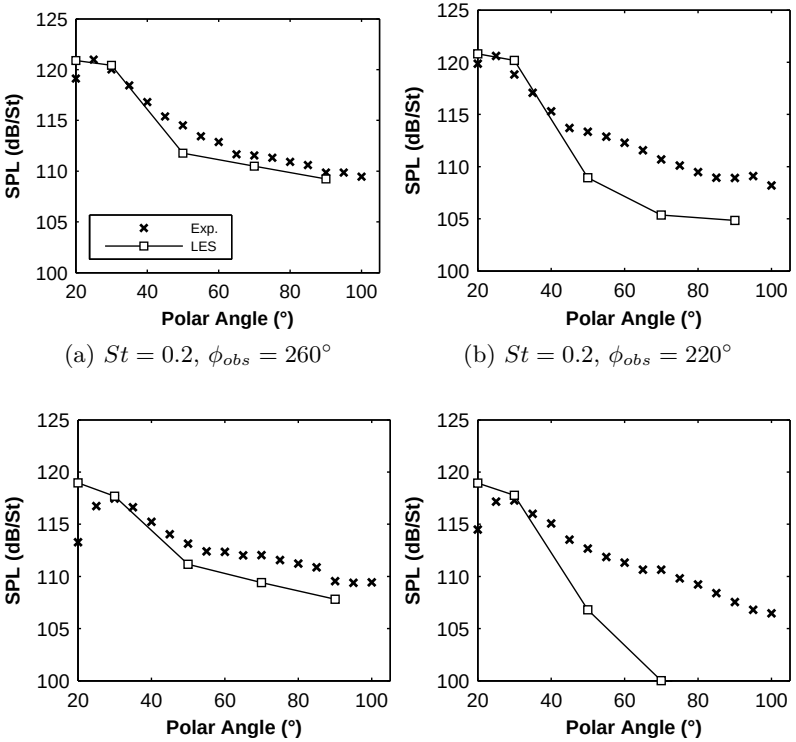

(a) $St = 0.2$, $\phi_{obs} = 260°$ (b) $St = 0.2$, $\phi_{obs} = 220°$

(c) $St = 0.3$, $\phi_{obs} = 260°$ (d) $St = 0.3$, $\phi_{obs} = 220°$

Figure 5.13 – Results obtained with the presence of the plate positioned at $r/D = 1.5$ and $\phi_{obs} = 220°$ and 260°. Comparison between different St.

5.3 CSD AND COHERENCE MAPS

This section aims at analyzing the characteristics of the source field, represented by the cross spectral density (CSD) of the simplified T_{xx} term. Figure 5.14 depicts contours of the power spectral density (PSD) of the source term for $St = 0.3$ and $St = 0.75$ in dB/St. The peak of the $PSDs$ are located at the centerline for both St. The contours for $St = 0.3$ show higher levels and a slower streamwise decay when compared to results for $St = 0.75$. Radial profiles also differ between St.

Figure 5.15 shows the contours of the CSD when the reference point is at the centerline and two axial positions ($x_{ref} = 2D$ and $5D$). Only the real part is shown for convenience. In the centerline, the CSD levels are stronger in comparison to the lipline (Figure 5.16). The plots show wavepacket structures whose axial extension varies with the radial position, being more concentrated in space in the shear layer region (Figure 5.16). In the inner jet region ($r/D < 0.5$), the wave structures are large, extending beyond $x/D = 8$ for low St.

The two-point coherence of the LES source data is computed for two points i and j by,

$$\gamma_{ij}^2 = \frac{|\langle S_i S_j^* \rangle|^2}{\langle |S_i|^2 \rangle \langle |S_j|^2 \rangle}. \tag{5.3}$$

With the reference point at the centerline, higher coherence levels (Figures 5.17) are more spread out in comparison with the lipline results (Figures 5.18). Similar observations can be drawn for $St = 0.75$ (Figures 5.20, 5.21 and 5.22), but with greater scale disparities between the different radial positions.

For both St evaluated, but more evident at $St = 0.75$, a very low coherence layer can be observed in the lower part of the shear layer. At the lipline (Figures 5.18 and 5.22(d)), the high coherence region is much more concentrated in a small circular region, losing the observed coherence with the other radial position observed when the reference was at the centerline (Figures 5.17 and 5.22(a)). This is more evident by observing the coherence variation with varying r_{ref} and fixed x_{ref} (Figures 5.19 and 5.22). However, these coherence plots are somewhat delusive, as the CSD plots still show significant correlation with the inner jet region, specially for $St = 0.3$ (Figure 5.18).

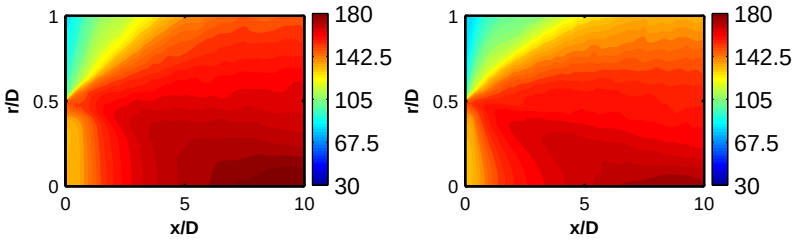

(a) $St = 0.3$ (b) $St = 0.75$

Figure 5.14 – LES PSD plots of the source term.

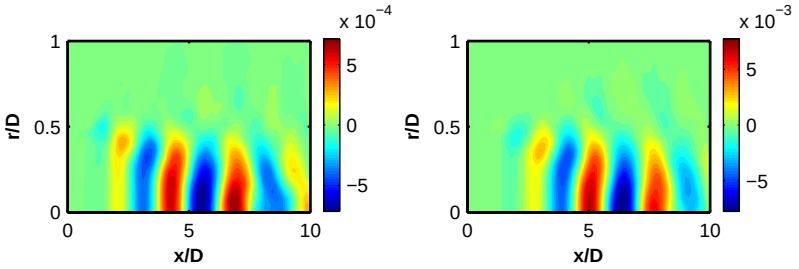

(a) $x_{ref} = 2D$ (b) $x_{ref} = 5D$

Figure 5.15 – LES real part of CSD plots varying the axial position at the centerline, $St = 0.30$

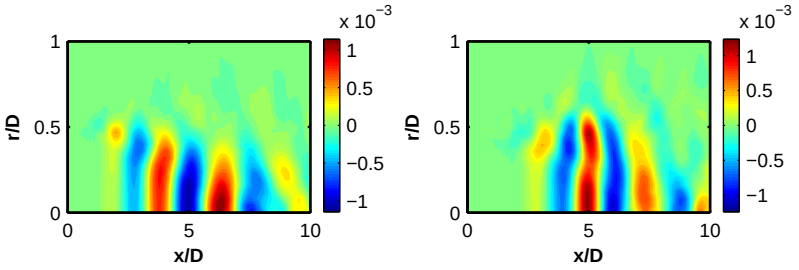

(a) $x_{ref} = 2D$ (b) $x_{ref} = 5D$

Figure 5.16 – LES real part of CSD plots varying the axial position at the lipline, $St = 0.30$

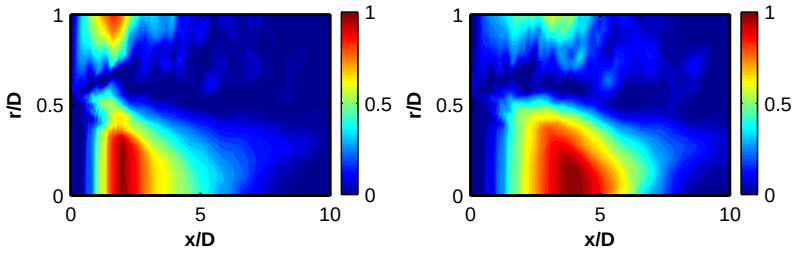

(a) $x_{ref} = 2D$ (b) $x_{ref} = 4D$

Figure 5.17 – LES Coherence plots varying the axial reference position at the centerline, $St = 0.3$

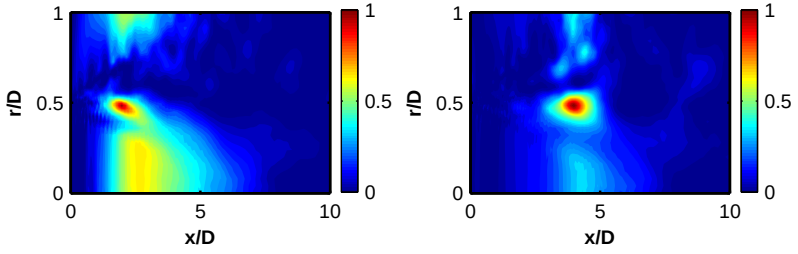

(a) $x_{ref} = 2D$ (b) $x_{ref} = 4D$

Figure 5.18 – LES Coherence plots varying the axial reference position at the lipline, $St = 0.30$

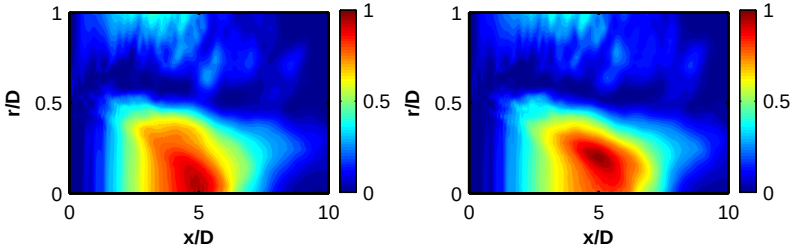

(a) $r_{ref} = 0D$ (b) $r_{ref} = 0.2D$

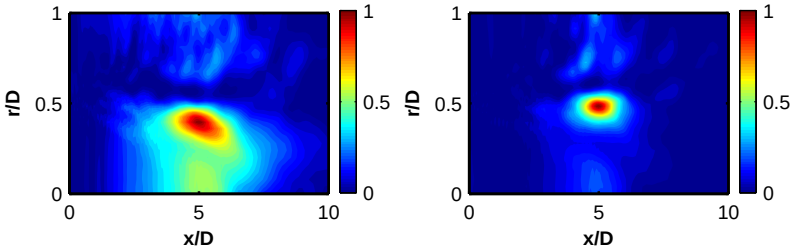

(c) $r_{ref} = 0.4D$ (d) $r_{ref} = 0.5D$

Figure 5.19 – LES Coherence plots varying the radial reference position in $x_{ref} = 5$, $St = 0.30$

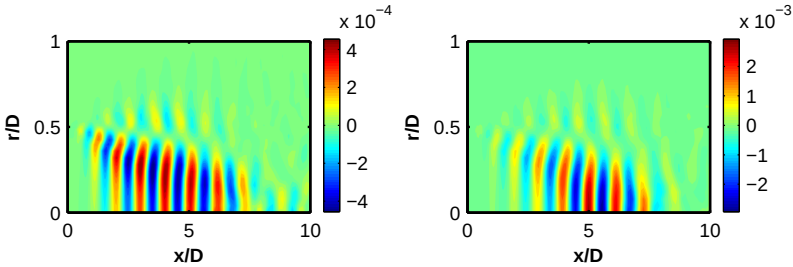

(a) $x_{ref} = 2D$ (b) $x_{ref} = 5D$

Figure 5.20 – Plots of the real part of CSD from the LES data varying the axial position at the centerline, $St = 0.75$

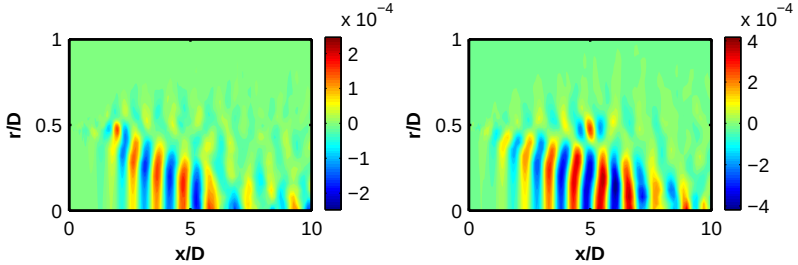

(a) $x_{ref} = 2D$ (b) $x_{ref} = 5D$

Figure 5.21 – Plots of the real part of CSD from the LES data varying the axial position at the lipline, $St = 0.75$

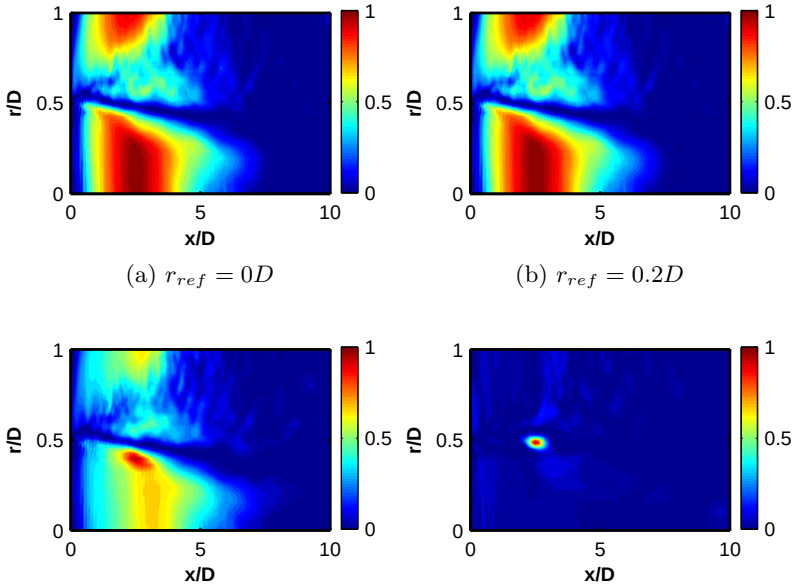

(a) $r_{ref} = 0D$ (b) $r_{ref} = 0.2D$

(c) $r_{ref} = 0.4D$ (d) $r_{ref} = 0.5D$

Figure 5.22 – LES Coherence plots varying the radial reference position at $x_{ref} = 2.5$, $St = 0.75$

5.4 COHERENCE LENGTH

The previous section showed significant variations of coherence patterns at different radial positions. For the source modeling, the axial two-point coherence (γ^2) decay is important. The proposed source models presented in Equations 3.34 and 3.37 imply a Gaussian coherence function, in the form of Equation 5.4. In this section, the accuracy of this approximation and the spatial variation of the axial coherence length (L_c) is analyzed. By using the least-squares method, L_c can be estimated from the numerical data. For each reference position (x_{ref}, r_{ref}), the L_c value is obtained by using the LES coherence data at the $r = r_{ref}$ line.

$$\gamma^2 = \exp\left(-\frac{(x_1 - x_2)^2}{L_c^2}\right) \tag{5.4}$$

Figures 5.23 and 5.24 depict the comparison of some of the fitted profiles with the LES coherence at different radial and axial positions for $St = 0.3$ and $St = 0.75$ respectively. It is clear that the used Gaussian function cannot represent the asymmetry of the LES profiles at $x_{ref} = 2.5D$ (Figures 5.23 (a), (b) and (c)). For $x_{ref} = 5D$, however, the profiles are more symmetric and the used function represents well the streamwise coherence decay (Figures 5.23 (d), (e) and (f)). The asymmetry of the LES profiles are even more evident for $St = 0.75$, in Figure 5.24. In spite of the deviations, the Gaussian function still seems to be a reasonable approach for modeling the coherence decay of the source model.

Figure 5.25 presents maps of the obtained L_c value with axis representing the reference positions. For all considered ranges, the maximum values are concentrated about $r/D = 0.2$. However, no clear trend could be identified with varying St. For $St = 0.2$, in Figure 5.25(a), the maximum is located around $x/D = 10$. Values about $L_c = 1D$ are located at $x < 2D$ and about $L_c = 1.5D$ at the lipline.

Even higher coherence lengths occur for $St = 0.3$ near the end of the potential core and radial position under $r/D = 0.4$ in Figure 5.25(b). The maximum position is now about $x/D = 5.5$. At the lipline, however, fitted values are lower at the higher St.

By examining results for $St = 0.75$, shown in Figure 5.25(d), it is possible to observe that the maximum value is moved further upstream, and L_c values higher than $2D$ are concentrated up to $x/D = 6$. At the lipline, L_c values are even smaller in comparison

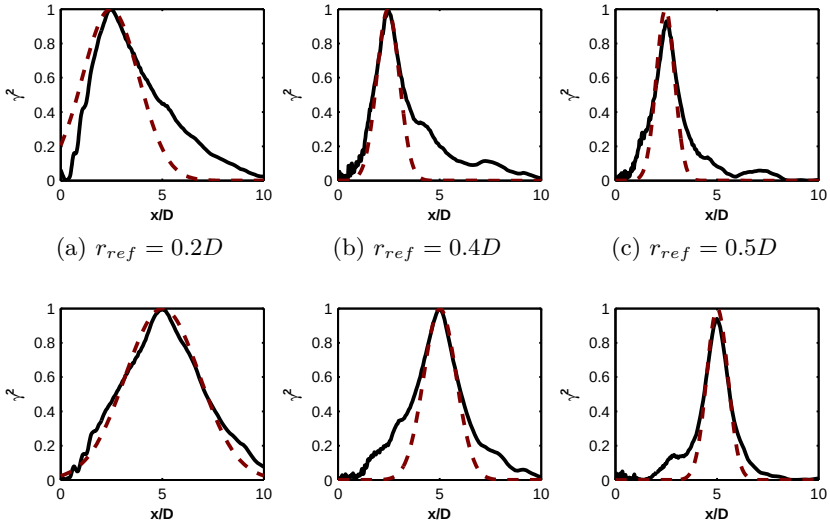

(a) $r_{ref} = 0.2D$ (b) $r_{ref} = 0.4D$ (c) $r_{ref} = 0.5D$

(d) $r_{ref} = 0.2D$ (e) $r_{ref} = 0.4D$ (f) $r_{ref} = 0.5D$

Figure 5.23 – Comparison of LES (—) and Gaussian (- - -) streamwise coherence profiles for $St = 0.30$. (a), (b) and (c) $x_{ref} = 2.5D$; (d), (e) and (f) $x_{ref} = 5D$

with $St = 0.3$ and $St = 0.2$, a fact also observed at the CSD plots of the previous section. The high values found at $r/D > 0.8$ are probably fitting errors due to the low CSD and PSD levels at this region (see Figures 5.20 and 5.14).

The results for $St = 0.4$ and 0.75 show that the relevant coherence area seems to move upstream as St increases. Some very high values appear near the nozzle exit for $St = 0.4$. This is probably due to fitting errors, as at this St value, the source CSDs present a strong presence of the trapped waves in the potential core. Due to possible fitting errors caused by this problem, obtaining parameters with curve fitting are avoided at this St.

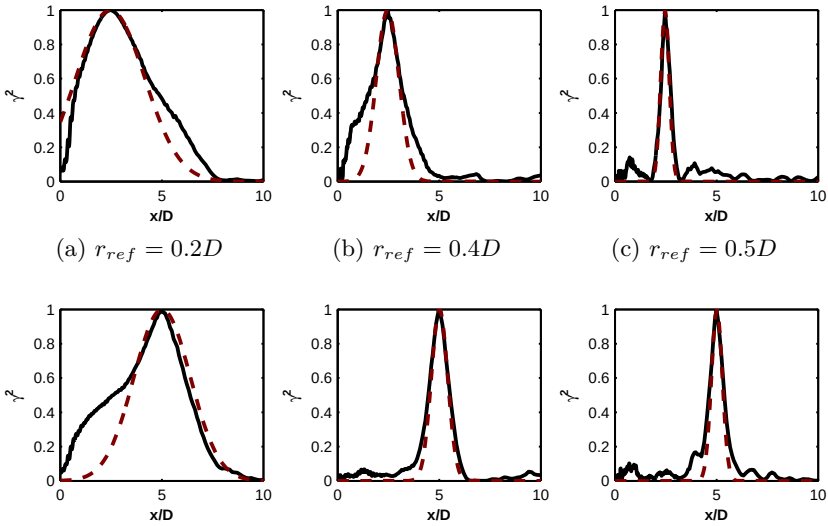

(a) $r_{ref} = 0.2D$ (b) $r_{ref} = 0.4D$ (c) $r_{ref} = 0.5D$

(d) $r_{ref} = 0.2D$ (e) $r_{ref} = 0.4D$ (f) $r_{ref} = 0.5D$

Figure 5.24 – Comparison of LES (—) and Gaussian (- - -) streamwise coherence profiles for $St = 0.75$. (a), (b) and (c) $x_{ref} = 2.5D$; (d), (e) and (f) $x_{ref} = 5D$

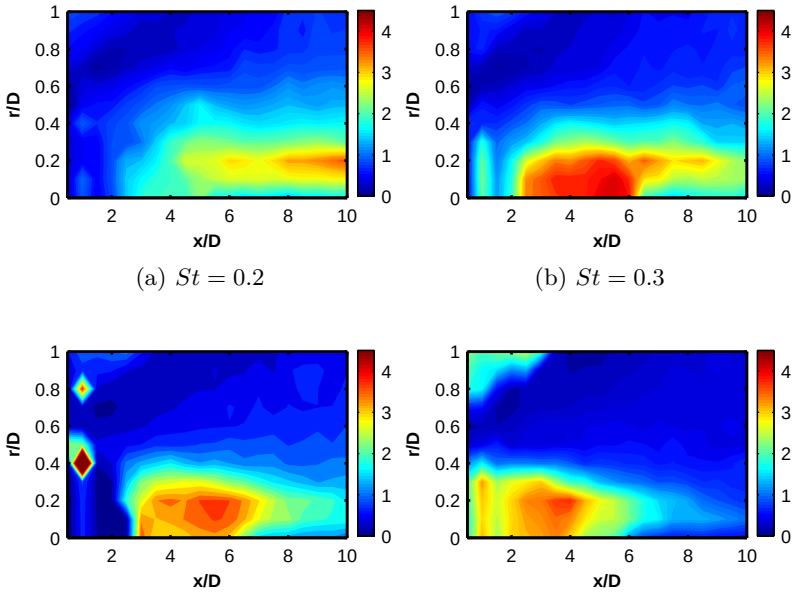

(a) $St = 0.2$ (b) $St = 0.3$

(c) $St = 0.4$ (d) $St = 0.75$

Figure 5.25 – L_c/D values calculated by Gaussian fits with varying reference positions

6 WAVEPACKET SOURCE MODEL

The objective of this chapter is to use the LES data presented in the previous chapter to adjust a simple kinematic wavepacket source model similar to those proposed by Crow (1972), Cavalieri *et al.* (2012), Cavalieri *et al.* (2014), Cavalieri and Agarwal (2014). The effects of the coherence decay in the installed jet case are also explored. The resulting model is useful for the understanding of the underlying physics of the problem and can also be regarded as a contribution towards a possible prediction tool.

6.1 FIT OF THE FULL CSD MATRIX

The source model presented in Equation 3.34, in Chapter 3, is repeated here for convenience:

$$\begin{aligned}&\langle S(\mathbf{y_a},\omega)S^*(\mathbf{y_b},\omega)\rangle = \\ &A\exp\left(-\frac{(x_a-X_c)^2}{L_x^2}-\frac{(x_b-X_c)^2}{L_x^2}\right)\exp\left(-\frac{r_a^2}{L_r^2}-\frac{r_b^2}{L_r^2}\right) \\ &\qquad\exp\left[-ik_h(x_a-x_b)\right]\exp\left(-\frac{|\mathbf{y_a}-\mathbf{y_b}|^2}{L_c^2}\right),\end{aligned} \tag{6.1}$$

in which the CSD of the source term is represented by 6 global parameters. A represents the maximum PSD amplitude, whose axial decay is represented by a Gaussian profile centered at X_c with characteristic length L_x. The radial profile is also represented by a Gaussian profile with envelope length L_r. Centering this second Gaussian at zero was taken as a reasonable assumption. Axial phase difference is defined by the hydrodynamic wavenumber k_h, related to the phase velocity $U_c/U_J = 2\pi St/k_h$. Finally the coherence decay is represented by Gaussian profiles of characteristic length L_c.

The parameters were obtained by minimizing the sum of the squares of the absolute error between the LES source and the proposed model. The domain for the fitting was limited between $x = 0.5D$ and $x = 15D$. The parameters found for each St are summarized in Table 6.1. The total relative error,

$$\Delta = \frac{\sum\sum||CSD_{LES}-CSD_{model}||}{\sum\sum||CSD_{LES}||}, \tag{6.2}$$

is shown in the same table.

Table 6.2 presents the evaluation of the source extension and axial interference. The obtained phase velocity U_c/U is presented in the same table. The parameter L_m,

$$L_m = \sqrt{\frac{L^2 L_c^2}{(2L^2 + L_c^2)}}, \tag{6.3}$$

was introduced by Cavalieri and Agarwal (2014) in order to represent the length scale of the problem when coherence decay is considered. Table 6.2 presents values for $k_h L$ and $k_h L_m$, quantifying the level of axial interference for the fitted source and for its unit coherence equivalent by the number of present oscillations. As observed by Cavalieri *et al.* (2012), these parameters are crucial for the superdirective characteristics of the wavepacket.

Values for $St = 0.2$ differ from the far-field fitted source models used by Cavalieri *et al.* (2012), which resulted in $k_h L = 6$ and $Uc/U = 0.97$ for $M = 0.6$. Although the results here are for $M = 0.9$, the resulting parameters showed increasing $k_h L_m$ with St, the opposite trend observed by Cavalieri *et al.* (2012). This fact is further explored with the noise-field results.

Table 6.1 – Values of the resulting source parameters from the CSD fits. Non-dimensional values.

	A $[\times 10^{-3}]$	X_c	L_x	L_r	k_h	L_c	Error (Δ)
$St = 0.2$	31.96	10.10	5.01	0.3	1.74	3.8	0.71
$St = 0.3$	26.34	8.81	5.28	0.267	2.49	3.21	0.65
$St = 0.75$	5.33	7.37	5.91	0.22	5.81	1.86	0.88

Table 6.2 – Values of the resulting source compactness parameters from the CSD fits. Non-dimensional values.

	L_m	$k_h L_m$	$k_h L$	U_c/U
$St = 0.2$	2.37	4.14	8.77	0.72
$St = 0.3$	2.09	5.19	13.15	0.75
$St = 0.75$	1.28	7.46	34.33	0.81

For the noise computation, the model source was defined on a grid extending from $x = -8L_x$ to $x = 8L_x$ and from $r = 0$ to $r = 1D$, with 25 points in the radial and 256 points in the axial directions. Results were verified to be grid independent with these values. Acoustic results are show in Figure 6.1 ($St = 0.2$), Figure 6.2 ($St = 0.3$) and Figure 6.3 ($St = 0.75$) for the free jet and the jet-plate case ($r/D = 1$). The LES results obtained with the simplified source term in Chapter 5 are reproduced in the same plots. It is important to emphasize that, although the experimental data is also presented for reference, it is more appropriate to compare the model results with the ones obtained from the LES data.

For all cases, levels were overpredicted by about 6 dB for $St = 0.2$ and 10 dB for $St = 0.3$ at 20°. In the free-jet case, levels were highly underpredicted over 60°. Figures 6.1(a), 6.2(a) and 6.3 show that the low-angle directivity trends for the axisymmetric mode could only be reasonably captured for $St = 0.2$. Agreement was poorer for $St = 0.75$, with levels matching the LES results about 40° and showing more that 10 dB of difference at the other angles.

Clearly, by observing Figure 6.2(a) and 6.3 the low-angle directivity was not followed by the model source. Deviations from the expected behavior increase with St. This is probably related to the also increasing $k_h L_m$ value shown in Table 6.2, which possibly came from errors in the parameter fitting process. The failure of the model in capturing the sideline noise may not be a major concern, since the axisymmetric mode and even T_{xx} do not have the main contributions to the total noise in this radiation direction. However, at low angles, the difficulties in predicting both the magnitude and directivity of the sound field do represent an important issue.

With the plate at $r/D = 1$, at polar angles dominated by the edge scattering noise and $\phi_{obs} = 260°$ (Figures 6.1(b) and 6.2(b)), levels were much closer to the reference experimental and LES data. Deviations were about 8 dB for $St = 0.2$ and ~ 1.5 dB for $St = 0.3$ at this azimuthal position. At $\phi_{obs} = 220°$ and $\phi_{obs} = 180°$ (Figures 6.1(c), (d) and 6.2(c), (d)), predictions followed the trends of the LES data, increasing the deviation from the experimental data as the observer is moved to a direction parallel to the plate.

At $\phi_{obs} = 180°$, the model predicted levels with magnitude very close to the free-jet case up to $\theta_{obs} = 60°$. Scattering effects seem to become important only at higher angles, but do not contribute significantly to the total noise. Trailing-edge effects are

not expected to be important at $St = 0.75$ so installed results were omitted for this case.

Figure 6.4 shows the comparison between experimental and model results for all the measured directivity range, with the plate at $r/D = 1$. The directivity trends could be well captured for azimuthal angles close to the plane perpendicular to the plate, say between $\phi_{obs} = 50°$ and $140°$ and between $\phi_{obs} = 220°$ and $320°$. Although the wavepacket model failed in the prediction of jet noise, specially at high angles and high St, results are promising whenever the edge scattering is dominant. These results are aligned with the observations from the previous chapter and Cavalieri *et al.* (2014).

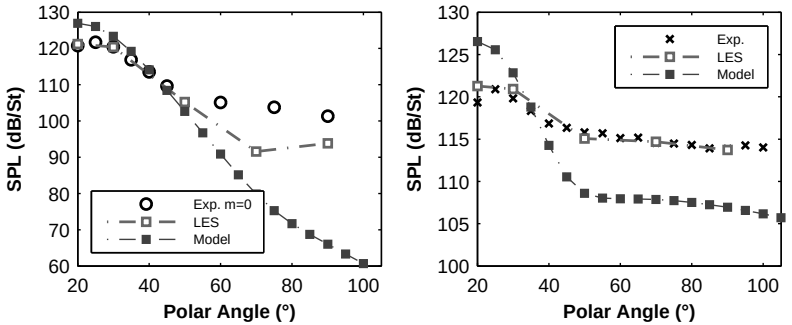

(a) Free-jet (b) Jet-plate $\phi_{obs} = 260°$

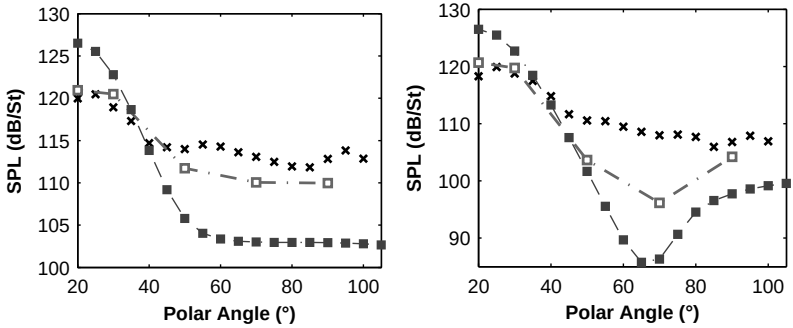

(c) Jet-plate $\phi_{obs} = 220°$ (d) Jet-plate $\phi_{obs} = 180°$

Figure 6.1 – Model source results compared to the experimental and LES data for $St = 0.2$ with Free-field and tailored Green's function.

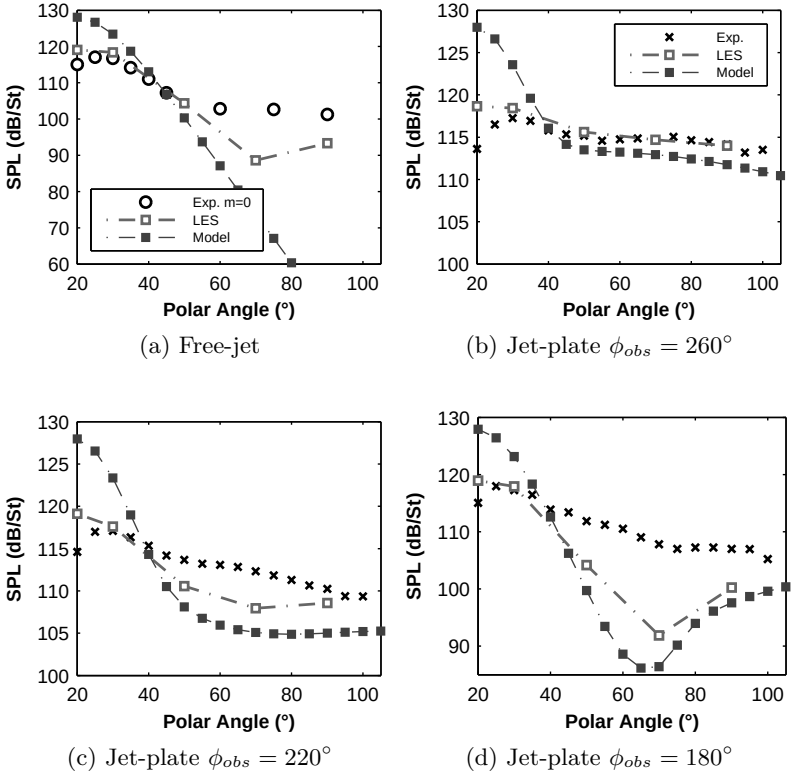

(a) Free-jet

(b) Jet-plate $\phi_{obs} = 260°$

(c) Jet-plate $\phi_{obs} = 220°$

(d) Jet-plate $\phi_{obs} = 180°$

Figure 6.2 – Model source results compared to the experimental and LES data for $St = 0.3$ with Free-field and tailored Green's function.

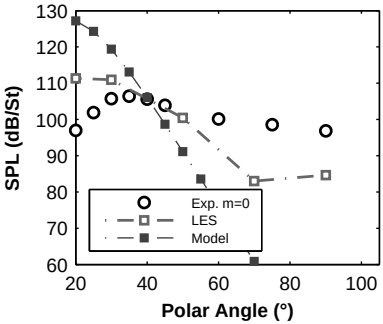

(a) Free-jet

Figure 6.3 – Model source results compared to the experimental and LES data for $St = 0.75$ with Free-field Green's function.

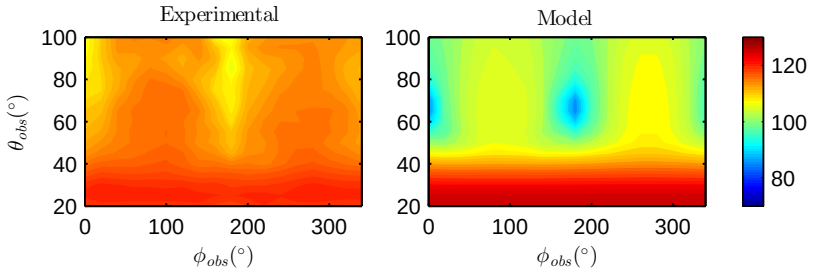

(a) $St = 0.2$

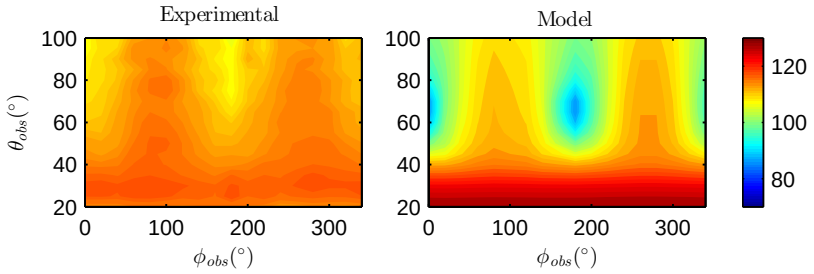

(b) $St = 0.3$

Figure 6.4 – Model source SPL results compared to the experimental data with tailored Green's function at all the measured positions.

The relative errors shown in table 6.1 are high, specially for $St = 0.75$, and imply a strong limitation of the used fit. In order to help understanding the possible causes of such deviations, plots of the LES and model source regions are compared in Figures 6.5 to 6.14. A clear mismatch in the PSD plots can be observed for different St in Figure 6.5. The fitting technique provided a good representation of the maximum amplitude, its position at the centerline and the source extension around the maximum. Nevertheless, there is a clear mismatch between the radial profiles up to $x/D = 5$ and in the jet shear layer. Also, the PSD levels are underestimated in the plate position ($r/D = 1$, $x/D \leq 4$). The use of Gaussian profiles for the axial and radial amplitudes contributed to these deviations, which become larger at higher St.

A further comparison between the LES and the wavepacket model is depicted in plots of CSD and coherence for different values of St and two fixed radial reference positions at $x_{ref} = X_c$. Figure 6.6(a) shows the real CSD plots with reference position at $r_{ref} = 0.3$ and $St = 0.2$. The model reproduces the main characteristics of the source between $x/D = 5$ and 10. However, greater divergence can be observed up to $x/D = 5$ around the lipline. When the reference point is at the lipline (Figure 6.7), the deviations are even more evident.

Figures 6.6(b) and 6.6(b) depict CSD plots multiplied by $r_{ref} \times r$. As they consider the source volume weighting (FREUND, 2001), these plots crudely represent which regions of the source may be important during the integration with the free-field Green's function (Equation 3.28). Information at $r = 0$, for instance, has no contribution to the free-jet sound field. The increased disparities between the LES and modeled contours, specially around the lipline, suggest that they could be the reason for the observed deviations at the far-field prediction. Coherence plots in Figure 6.8 also show the divergence in axial and radial coherence length at $r_{ref} = 0.5D$. These disparities were already expected considering the spatial variation of the coherence length highlighted by the Figure 5.25 in the previous chapter.

Similar conclusions can be drawn for $St = 0.3$ and $r_{ref} = 0.3$ (Figure 6.9 and 6.11(a)) but with greater errors at $r_{ref} = 0.5$ (Figure 6.10 and 6.11(b)). Again, disparities are more evident when the source CSD is multiplied by $r_{ref}r$ (Figures 6.9(b) and 6.10(b)). By observing these plots, it seems the low levels around $r = 0.5D$ may be a cause for the poor prediction of the $m = 0$ free-jet noise.

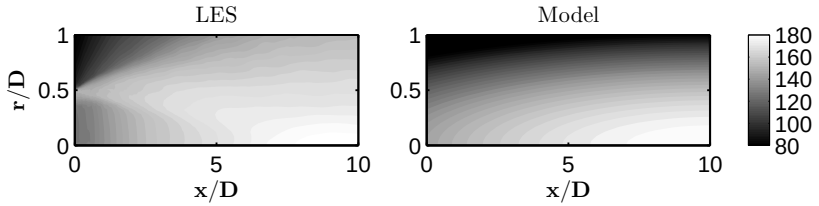

(a) $St = 0.2$

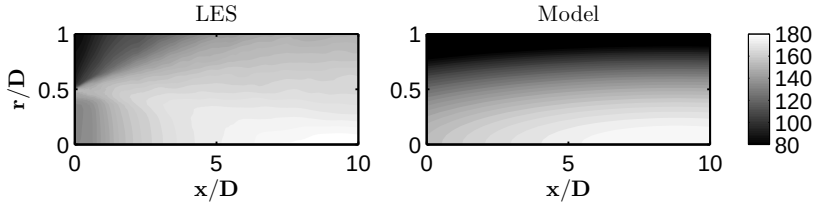

(b) $St = 0.3$

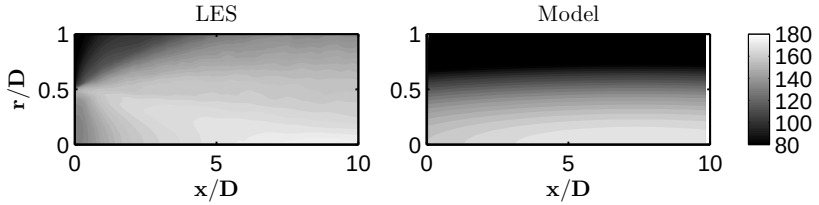

(c) $St = 0.75$

Figure 6.5 – Comparison between PSD [dB/St] plots of the source term obtained from the LES data and model source.

On the other hand, the integration with the tailored Green's function is much more complex, since the function is also dependent of the distances between source and trailing edge. In this sense, the observations above are not necessarily valid for the installed case. Moreover, the content of both Green's functions in the wavenumber space are different (CAVALIERI; AGARWAL, 2014; NOGUEIRA *et al.*, 2017), which would permit source wavenumbers that were not propagated in the free-field case to generate noise with the presence of the plate. This is possibly why the results with the plate were found in good agreement with the reference data, despite the differences observed in the free-jet case.

Similar observations can be made for $St = 0.75$ (Figures 6.12, 6.13 and 6.14). However, even large discrepancies are present, which can be the cause of the poor prediction of noise levels at this St. Moreover, it is important to emphasize that the present model does not account for the radial phase difference and coherence decay.

Although it is not straightforward to identify the causes of errors in the acoustic prediction by just examining the source field, it is evident that some considerable deviations are present in the modeling approach. Such shortcomings are possibly caused by the use of simple Gaussian functions for both the amplitudes and coherence, as well as neglecting the radial phase differences and coherence. However, the present study is in the framework of simple kinematic models, and hence, the inclusion of complicated parameters is not the goal of this work. Nevertheless, it is important to emphasize that, even with the mentioned simplifications, the model could reasonably represent the expected noise characteristics of the phenomenon, especially for the installed case. By using the same 6-parameter model, the next section aims at characterizing the sensitivity of the results to the coherence length.

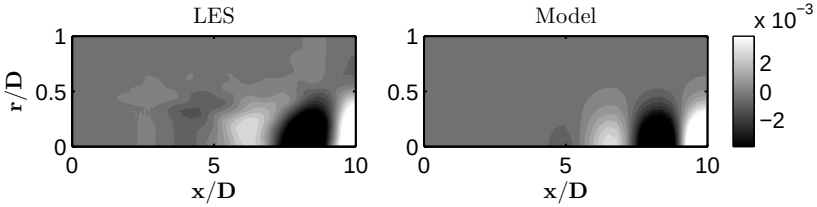

(a) $\Re(CSD)$

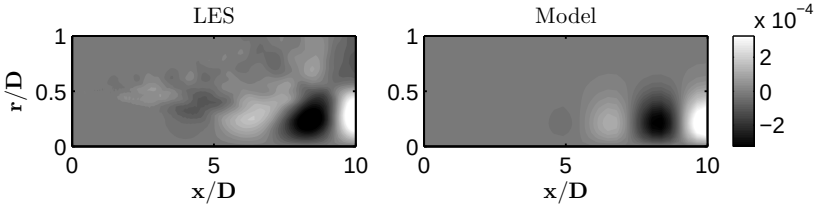

(b) $\Re(CSD) \times r_{ref} r$

Figure 6.6 – Comparison between plots of real part of the CSD obtained from the LES data and from the model source at $x_{ref} = X_c$ and $r_{ref} = 0.3D$, $St = 0.20$.

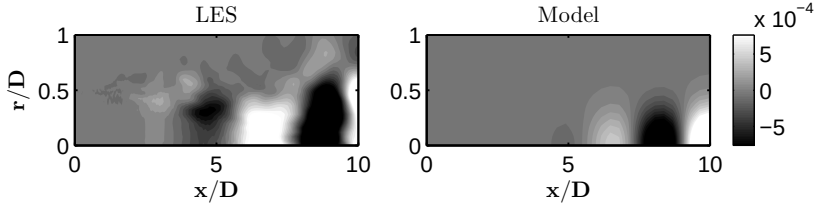

(a) $\Re(CSD)$

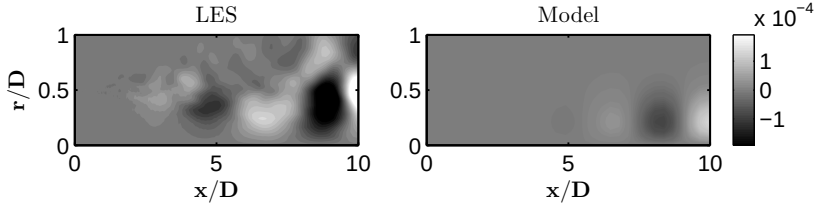

(b) $\Re(CSD) \times r_{ref} r$

Figure 6.7 – Comparison between plots of real part of the CSD obtained from the LES data and from the model source at $x_{ref} = X_c$ and $r_{ref} = 0.5D$, $St = 0.20$.

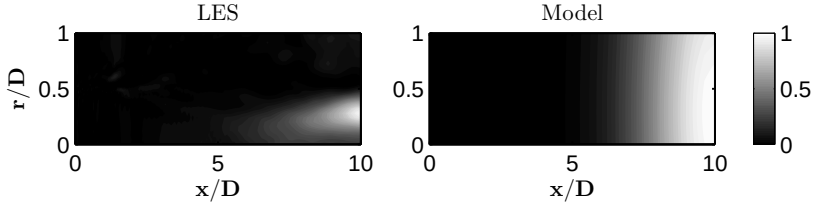

(a) $r_{ref} = 0.3D$

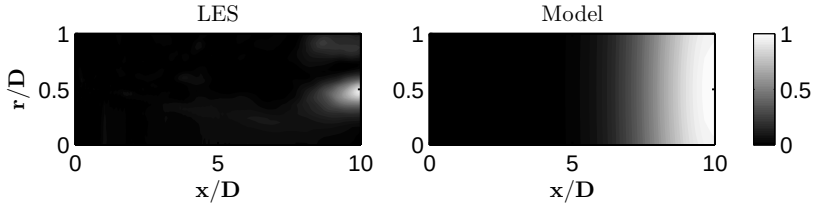

(b) $r_{ref} = 0.5D$

Figure 6.8 – Comparison between coherence plots of the source term from the LES data and from the model source at $x_{ref} = X_c$, $St = 0.20$.

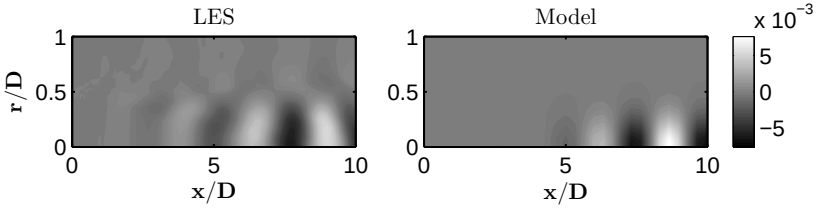

(a) $\Re(CSD)$

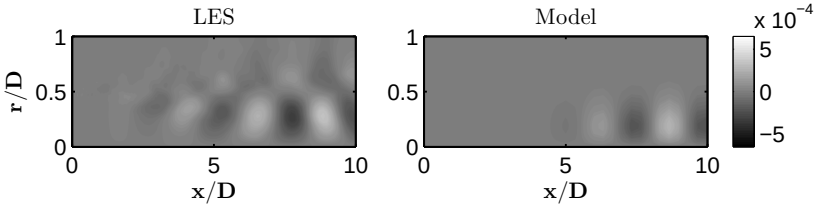

(b) $\Re(CSD) \times r_{ref} r$

Figure 6.9 – Comparison between plots of real part of the CSD obtained from the LES data and from the model source at $x_{ref} = X_c$ and $r_{ref} = 0.3D$, $St = 0.30$.

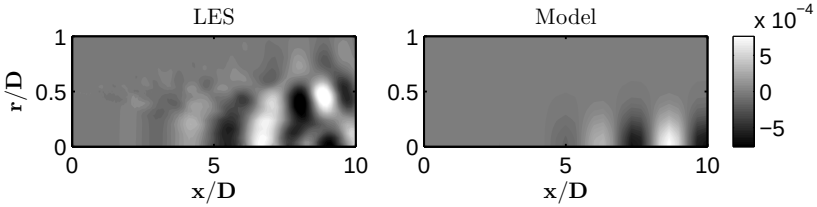

(a) $\Re(CSD)$

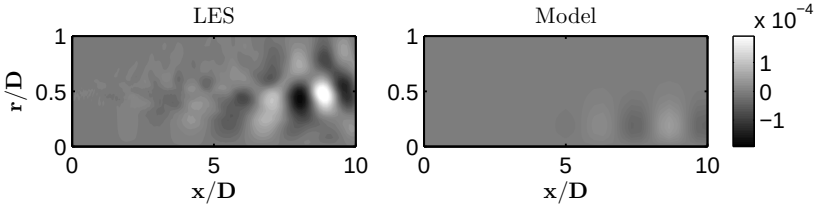

(b) $\Re(CSD) \times r_{ref} r$

Figure 6.10 – Comparison between plots of real part of the CSD obtained from the LES data and from the model source at $x_{ref} = X_c$ and $r_{ref} = 0.5D$, $St = 0.30$.

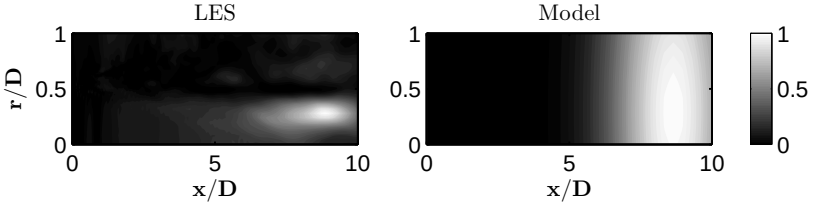

(a) $r_{ref} = 0.3D$

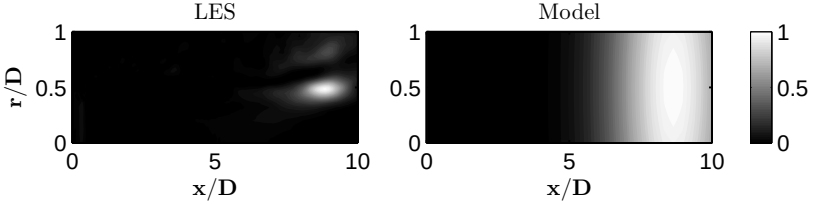

(b) $r_{ref} = 0.5D$

Figure 6.11 – Comparison between coherence plots of the source term obtained from the LES data and from the model source at $x_{ref} = X_c$, $St = 0.30$.

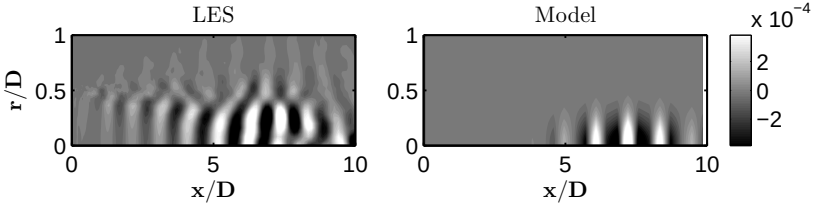

(a) $\Re(CSD)$

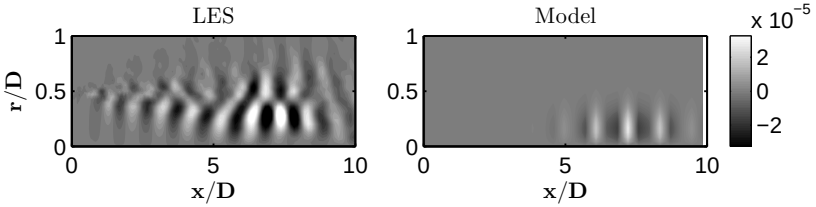

(b) $\Re(CSD) \times r_{ref} r$

Figure 6.12 – Comparison between plots of real part of the CSD obtained from the LES data and from the model source at $x_{ref} = X_c$ and $r_{ref} = 0.3D$, $St = 0.75$.

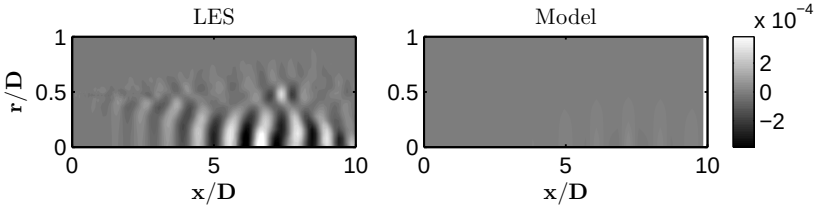

(a) $\Re(CSD)$

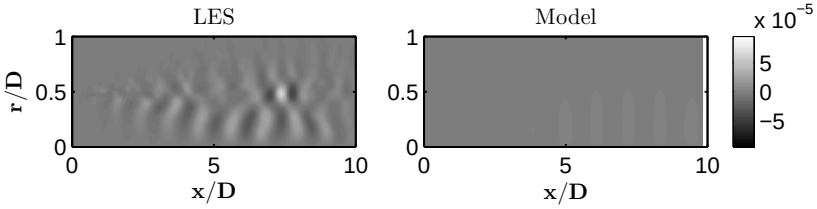

(b) $\Re(CSD) \times r_{ref} r$

Figure 6.13 – Comparison between plots of real part of the CSD obtained from the LES data and from the model source at $x_{ref} = X_c$ and $r_{ref} = 0.5D$, $St = 0.75$.

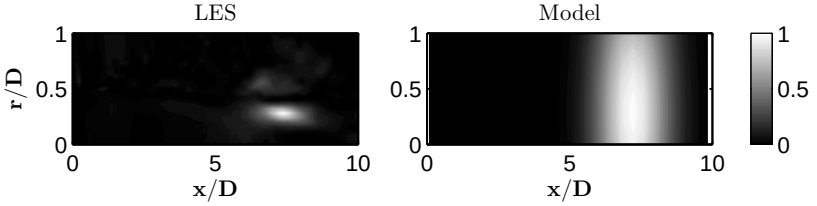

(a) $r_{ref} = 0.3D$

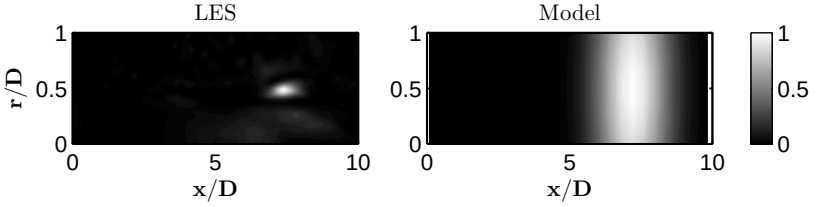

(b) $r_{ref} = 0.5D$

Figure 6.14 – Comparison between coherence plots of the source term obtained from the LES data and from the model source at $x_{ref} = X_c$, $St = 0.75$.

6.2 SENSITIVITY TO THE COHERENCE LENGTH

As already mentioned, the coherence length is a fundamental parameter in wavepacket models for isolated jet prediciton (CAVALIERI; AGARWAL, 2014; BAQUI *et al.*, 2015). The objective of this section is to assess the effects of the variation of this parameter on noise prediction. This variation is based on the range of values identified in the LES data in Figure 5.25 at $x = X_c(St)$. Three values were defined: the value at the lipline (L_c^C), the radial average of L_c until $r = 0.5D$ (L_c^B) and the original value from the previous section (L_c^A), as summarized in table 6.3.

Table 6.3 – Values of the resulting parameters of the model source. Non-dimensional values.

	L_c^A	L_c^B	L_c^C	$k_h L_m^A$	$k_h L_m^B$	$k_h L_m^C$
$St = 0.2$	3.8	1.63	1.36	4.14	1.96	1.65
$St = 0.3$	3.21	1.90	1.34	5.19	3.24	2.32
$St = 0.75$	1.86	0.70	0.32	7.46	2.87	1.33

Sound-field results for $St = 0.3$ in Figure 6.15(a), show a clear change in the noise directivity with the different L_c values. Results with an unit coherence source ($L_C^0 \longrightarrow$ inf) are also included in the comparison. Good prediction of the LES noise levels at high angles was achieved by considering the average of L_c values up to $r = 0.5D$. The source with the lipline L_c^C produces very high noise levels in comparison with the experiments and LES data. Although reasonable level agreement at low angles was only obtained when considering the larger, original L_c^A, only results with L_c^C reproduced the directivity trends.

Figure 6.16 shows similar trends for $St = 0.75$, but with much higher sensitivity to the coherence parameter. Reasonable agreement with LES data was only achieved at low angles. Considering the directivity, only Lc^C could reasonably capture directivity trends of the LES results, despite the very high levels. However, it is hard to draw conclusions about this region, since experimental results are affected by refraction effects.

Such sensitivity, however, does not occur for the installed case at $\phi_{obs} = 260°$, over $\theta_{obs} = 50°$ (Figure 6.15(b)). In this case, the results are much less dependent on the coherence parameter. The agreement with the reference data at the edge-scattering-dominated region is good even for the unit

coherence source. At the other azimuthal angles (Figure 6.15(c) and (d)), this sensitivity becomes higher as the observer moves to a direction parallel to the plate trailing edge, whenever the scattering effects are low. This also happens when the plate is moved away from the jet, as shown in Figure 6.17. Nevertheless, the sensitivity to coherence seems to be very low when edge scattering effects are dominant. It should also be observed that the levels obtained for the lower L_c^C are not so affected by the scattering at high angles, say above 80°. The possible reasons are that the resulting free jet noise is so high, that it masks the scattering noise and that the source is approaching the compact limit, so scattering effects are reduced, as observed by Nogueira *et al.* (2017).

Results for $St = 0.2$ showed similar trends to those for $St = 0.3$ and were omitted here. The overall conclusion from these results is that the scattered field shows low sensitivity to the coherence decay.

Figures 6.18 and 6.19 depict the comparison between LES and model results in terms of CSD, using the three chosen L_c values for $St = 0.30$, as well as the unit coherence source (Lc^0). CSD plots are shown for two radial reference positions $r/D = 0.3$ and 0.5. Figure 6.18 shows that sources with L_c^A and L_c^B reproduce well the LES CSD with reference at the central part of the jet, while L_c^C results in a source much more concentrated in space in comparison to the LES. This is due to the low value of L_c obtained at this axial position and $r/D = 0.5$.

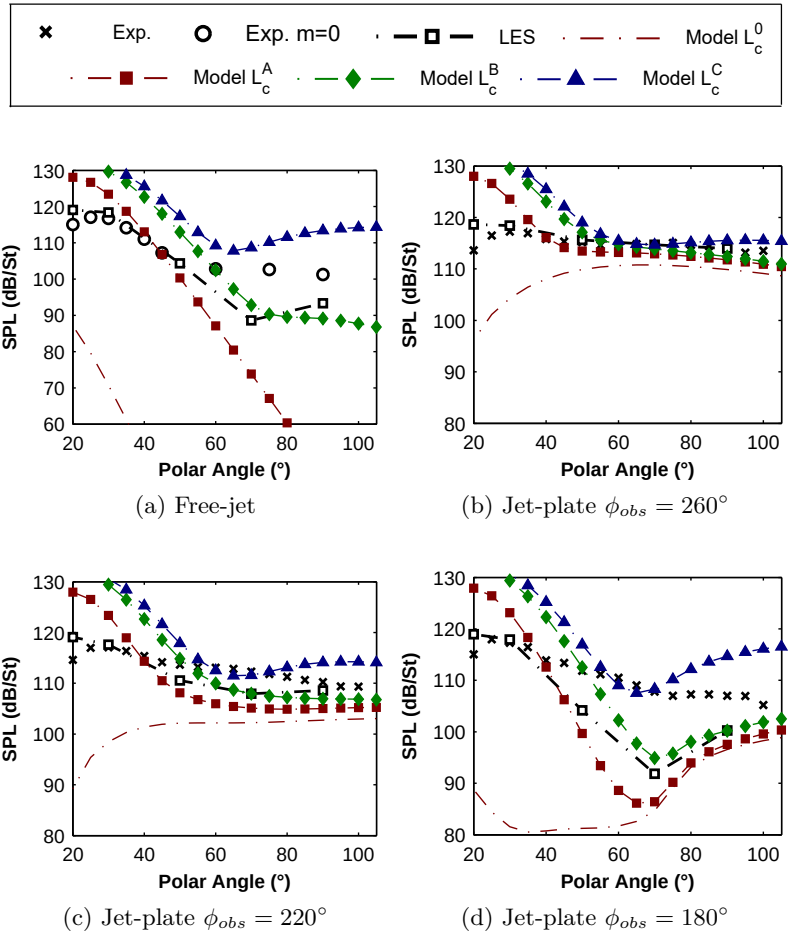

(a) Free-jet

(b) Jet-plate $\phi_{obs} = 260°$

(c) Jet-plate $\phi_{obs} = 220°$

(d) Jet-plate $\phi_{obs} = 180°$

Figure 6.15 – Model source results compared to the experiment and LES data for $St = 0.3$ with Free-field and tailored Green's function with varying L_c.

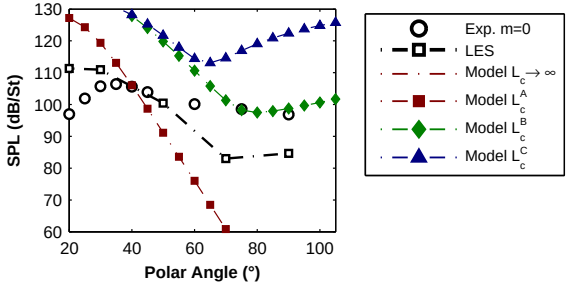

(a) Free-jet

Figure 6.16 – Model source results with Free-field Green's function compared to the experiment and LES data for $St = 0.75$.

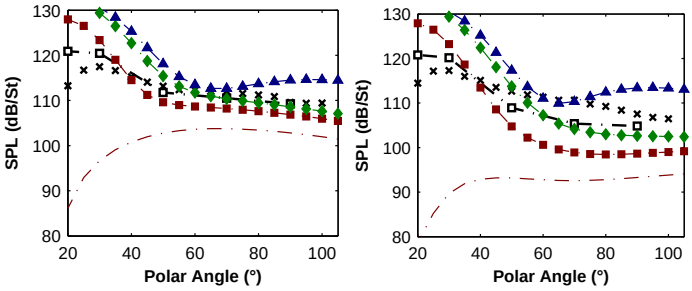

(a) Jet-plate $\phi_{obs} = 260°$ (b) Jet-plate $\phi_{obs} = 220°$

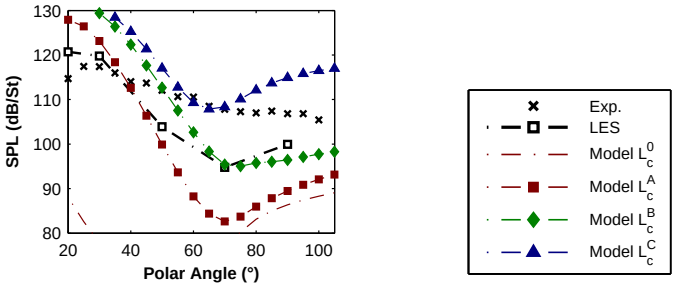

(c) Jet-plate $\phi_{obs} = 180°$

Figure 6.17 – Model source results with varying L_c compared to the reference data for $St = 0.3$ with tailored Green's function for $r/D = 1.5$.

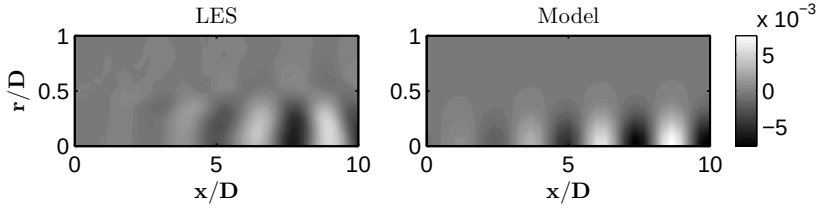

(a) L_c^0

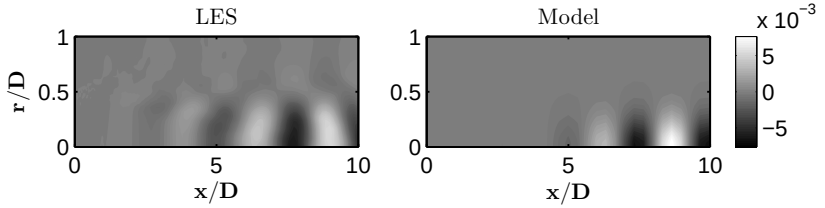

(b) L_c^A

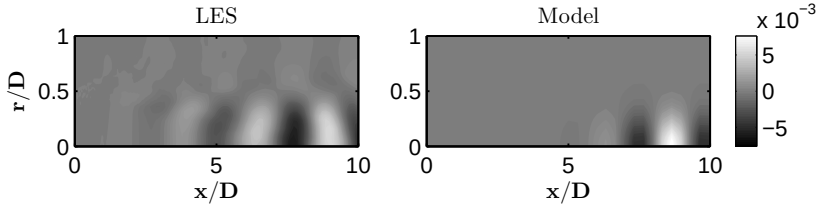

(c) L_c^B

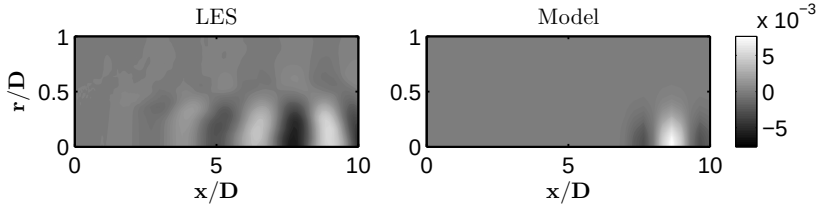

(d) L_c^C

Figure 6.18 – Comparison between plots of real part of the CSD obtained from the LES data and from the model source with three different L_c values at $r_{ref} = 0.3D$, $St = 0.30$.

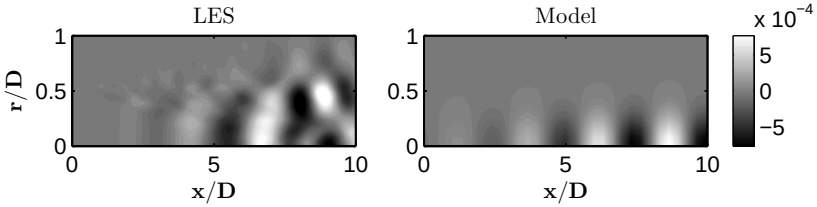

(a) L_c^0

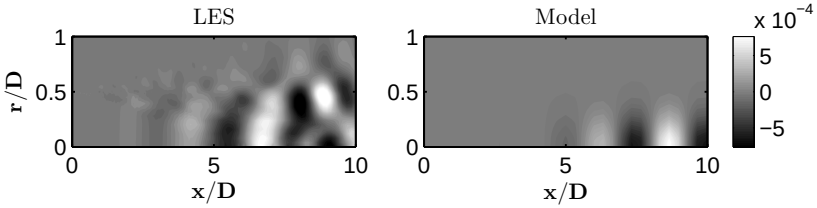

(b) L_c^A

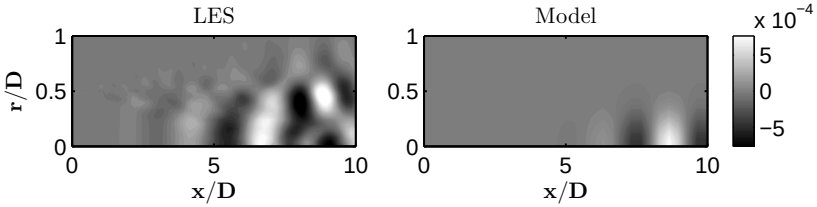

(c) L_c^B

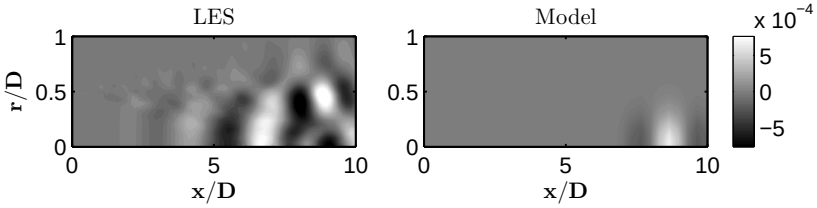

(d) L_c^C

Figure 6.19 – Comparison between plots of real part of the CSD obtained from the LES data and from the model source with three different L_c values at $r_{ref} = 0.5D$, $St = 0.30$.

6.3 ANALYSIS WITH LINE SOURCE

With the objective of reducing the observed errors in the parameter adjusting processed, the source is further simplified to eliminate the radial information. To this end, a line source was educed by considering radial compactness at low St. The derivation of the line source is described in Chapter 3 and the result is given by Equation 6.4. The source parameters are obtained by using the double radial integral of the LES source and are summarized in Table 6.4.

$$\langle S_l(x_a, m=0, \omega) S_l^*(x_b, m=0, \omega)\rangle = (2\pi)^2 A \exp\left(-\frac{(x_a - X_c)^2}{L_x^2} - \frac{(x_b - X_c)^2}{L_x^2}\right) \exp\left[-ik_h(x_a - x_b)\right] \exp\left(-\frac{(x_a - x_b)^2}{L_c^2}\right). \quad (6.4)$$

Table 6.4 – Values of the resulting source parameters from the line CSD fits. Non-dimensional values.

	X_c	L_x	U_c/U	L_c	$k_h L_m$
$St = 0.2$	8.07	5.56	0.64	2.76	3.62
$St = 0.3$	5.72	3.79	0.69	2.74	4.72
$St = 0.75$	3.46	2.41	0.73	3.76	11.52

Although the approximation seems valid for free jets, its application may be not correct for the installed case, since the Green's function depend on the distances between source and trailing-edge, which varies azimuthally. Assuming radial compactness in this case will probably lead to larger errors for the installed case. To reduce the effects of these simplifications, a cylindrical source concentrated on the lipline is also used, as defined by Nogueira *et al.* (2017). The same parameters used for the line source are used in the cylindrical surface approach.

Some of the values in Table 6.4 changed significantly from those in Table 6.1. The axial position of the maximum appears more upstream for all St. The L_x now decreases with St, i. e., the opposite trend from the observed with the two-dimensional model. The phase velocity also shows reduced values for all St. Again, the $k_h L_m$ value increases with St, an opposite trend from that observed by Cavalieri *et al.* (2012) with a far-field fitted source.

Acoustic results are show in Figure 6.20 for $St = 0.2$, comparing the line and cylindrical-surface sources. For the isolated jet, results are in better agreement with the reference data in both amplitude and directivity, when compared to the previously used source models. Regarding the installed jet cases, improvements could also be observed in the prediction of the scattered field for $St = 0.2$. Now the installation levels are in very good agreement with the reference data. However, it is important to emphasize that the fitting with the radially integrated data can lead to errors in the prediction of the jet-plate noise.

Comparing the parameters with Table 6.2 for $St = 0.2$, we can observe a considerable reduction of the phase velocity, reduction of L_c, X_c and $k_h L_m$. The latter is probably responsible for the better reproduction of the directivity of the free jet. As the installation is not very sensitive to the source extension and coherence, the reduction of X_c is a possible cause for the increased noise levels, as the maximum source levels are now closer to the trailing edge position.

Free-jet noise results were also improved for $St = 0.3$ (Figure 6.21 (a)). Minor differences can be noted between the line and cylindrical surface sources, even for the installed cases with plates at $r/D = 1$ (Figure 6.21) and $r/D = 1.5$ (Figure 6.22). In the one-dimensional source approaches, the model parameters can be more accurately evaluated. This is a possible cause for the better agreement of the line and cylindrical sources with the LES data at low St. On the other hand, results for $St = 0.75$, depicted in Figure 6.23, show a highly directive source with high deviations form the reference data. This was a result of the high $k_h L_m = 11.5$ obtained from the fitting, again indicating high axial interference and non-compactness. This was not expected at this St.

Figure 6.24 compares the radially integrated LES data with the fitted model sources with reference point at $X_c(St)$. As can be seen, the model can reproduce the main characteristics of the LES source in terms of PSD, CSD and coherence. Indeed, it becomes

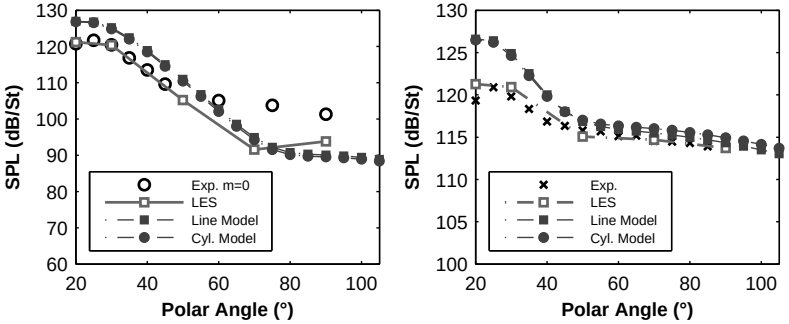

(a) Free-jet (b) Jet-plate $\phi_{obs} = 260°$

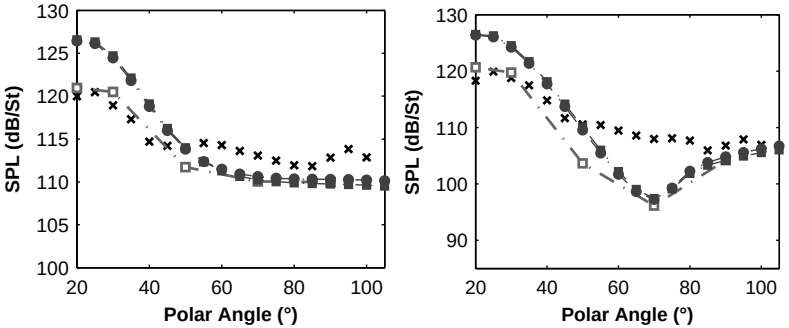

(c) Jet-plate $\phi_{obs} = 220°$ (d) Jet-plate $\phi_{obs} = 180°$

Figure 6.20 – Model source results compared to the experiment and LES data for $St = 0.2$ with Free-field and tailored Green's function for $r/D = 1$.

much simpler to fit line information with simple Gaussian functions in comparison with the two-dimensional cases presented in the previous sections. The difficulties regarding the radial variation of the L_c, for instance, are overcome by compacting the coherence information in a line. It is important to note, however, that the shapes of both the PSD and coherence are not symmetric, especially for $St = 0.75$. In Figure 6.24 (i), for instance, the coherence shows a narrow peak, with rapid decay, followed by a much slower decay at the left side. Figure 6.25 and 6.26 show CSD and coherence profiles at reference positions upstream and

downstream of X_c. Deviations from the LES reference data increase at these positions.

Even though the asymmetric shapes of both the PSD and coherence could not be completely represented by the used functions, it is clear the information was enough for a good and fast prediction of the trailing-edge scattering noise. In fact, more complex modeling seems to be required for the isolated jet at higher St, both regarding the radial information and the analysis of the coherence function. This is out of the scope of the present study.

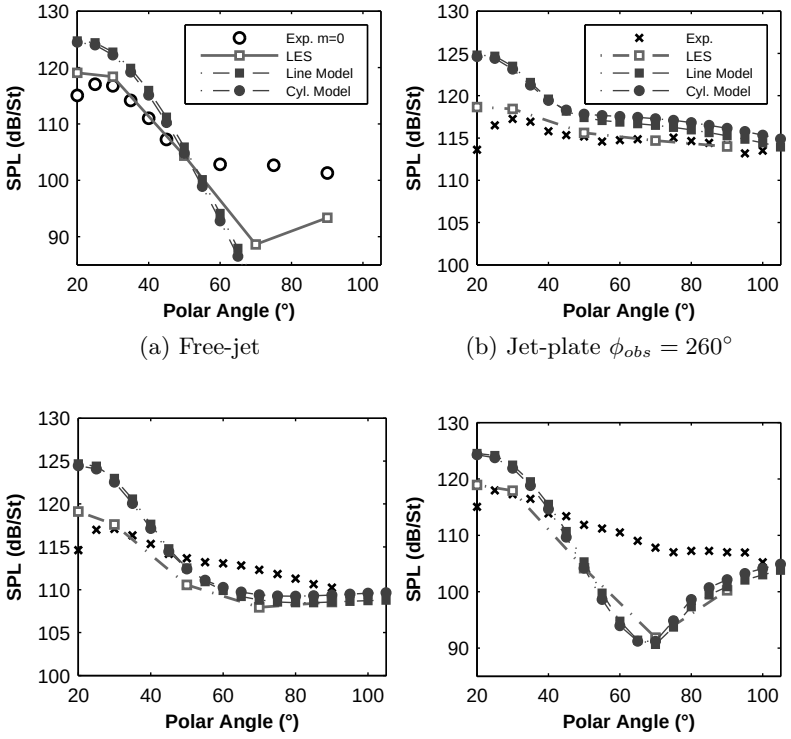

(a) Free-jet

(b) Jet-plate $\phi_{obs} = 260°$

(c) Jet-plate $\phi_{obs} = 220°$

(d) Jet-plate $\phi_{obs} = 180°$

Figure 6.21 – One-dimensional source results compared to the experimental and LES data for $St = 0.3$ with Free-field and tailored Green's function for $r/D = 1$.

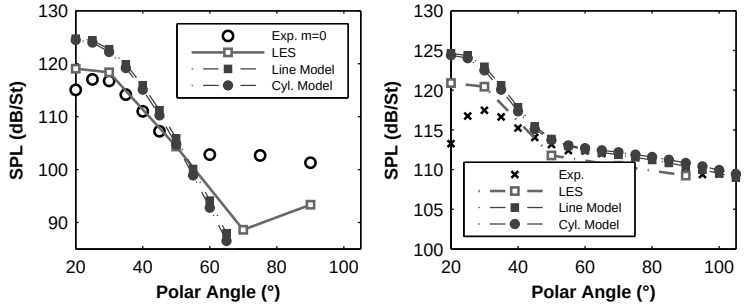

(a) Free-jet

(b) Jet-plate $\phi_{obs} = 260°$

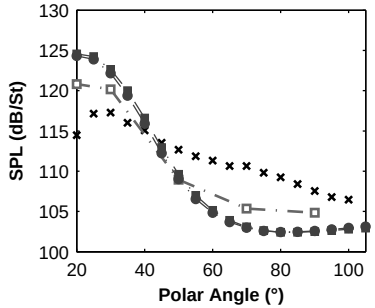

(c) Jet-plate $\phi_{obs} = 220°$

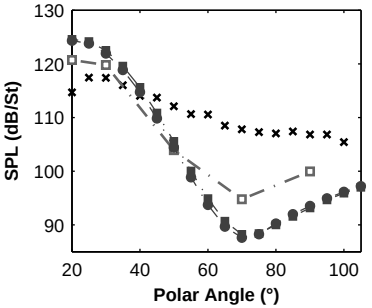

(d) Jet-plate $\phi_{obs} = 180°$

Figure 6.22 – One-dimensional source results compared to the experimental and LES data for $St = 0.3$ for $r/D = 1.5$.

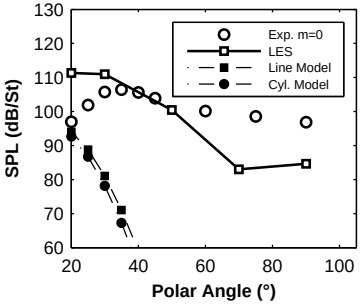

(a) Free-jet

Figure 6.23 – One-dimensional source results compared to the experimental data for $St = 0.75$ with Free-field Green's function.

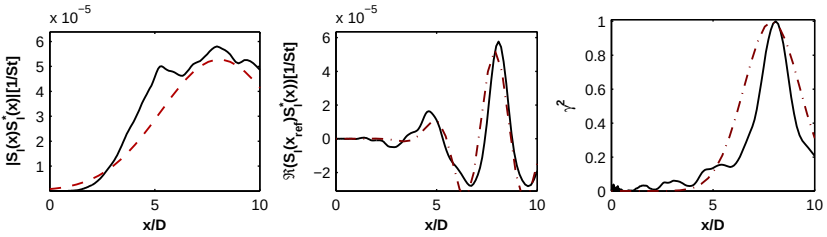

(a) PSD $St = 0.2$ (b) CSD $St = 0.2$ (c) Coherence $St = 0.2$

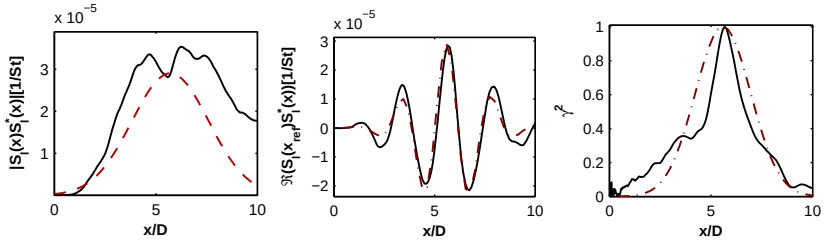

(d) PSD $St = 0.3$ (e) CSD $St = 0.3$ (f) Coherence $St = 0.3$

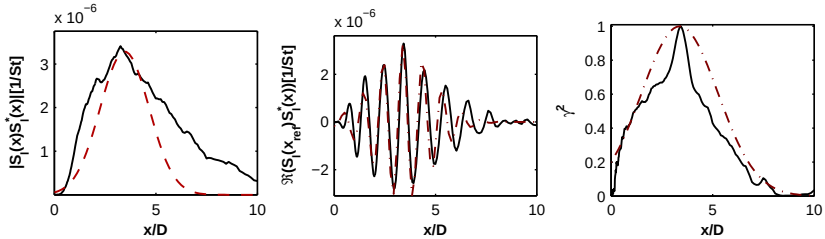

(g) PSD $St = 0.75$ (h) CSD $St = 0.75$ (i) Coherence $St = 0.75$

Figure 6.24 – Comparison between the integrated LES (—) and model line source (-.-.-.). CSD and coherence profiles at $x_{ref} = X_c(St)$.

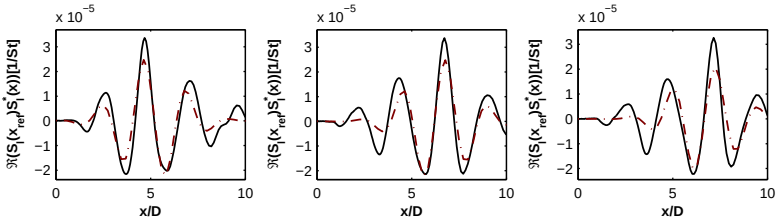

(a) $x_{ref} = X_c - 1D$ (b) $x_{ref} = X_c + 1D$ (c) $x_{ref} = X_c + 1.5D$

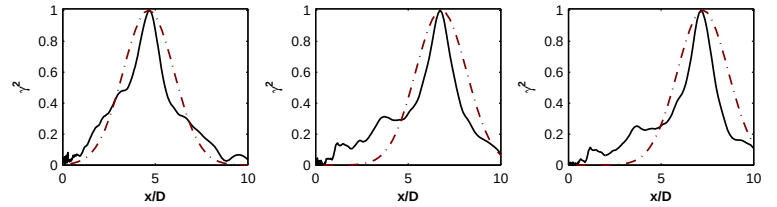

(d) $x_{ref} = X_c - 1D$ (e) $x_{ref} = X_c + 1D$ (f) $x_{ref} = X_c + 1.5D$

Figure 6.25 – Comparison between the integrated LES (—) and model line source (-.-.-.) for $St = 0.3$.

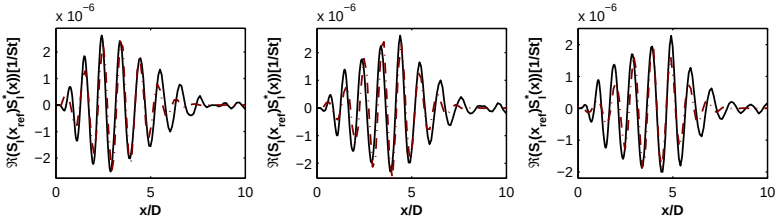

(a) $x_{ref} = X_c - 1D$ (b) $x_{ref} = X_c + 1D$ (c) $x_{ref} = X_c + 1.5D$

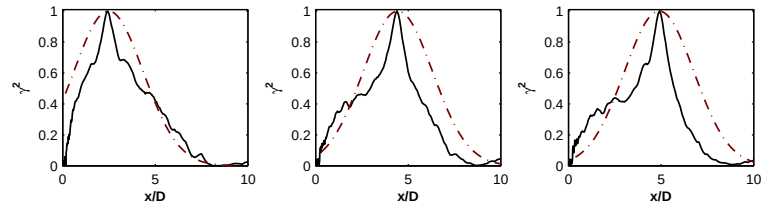

(d) $x_{ref} = X_c - 1D$ (e) $x_{ref} = X_c + 1D$ (f) $x_{ref} = X_c + 1.5D$

Figure 6.26 – Comparison between the integrated LES (—) and model line source (-.-.-.) for $St = 0.75$.

7 CONCLUSIONS

A study of jet-plate interaction noise was conducted using numerical data as input for wavepacket source models. A simplified source term was extracted from a numerical simulation database and the corresponding acoustic field was obtained for both the free-jet, by using the free-field Green's function, and for the installed jet by using a tailored function for a semi-infinite plate. After analyzing the main characteristics of the simplified source term, the numerical data was used to adjust the parameters of simple source models. The noise prediction capabilities of such models were assessed for both isolated and installed jets.

Initially, the adequacy of results obtained via the Lattice Boltzmann Method (LBM) and Large Eddy Simulation of the Navier-Stokes equations (LES) was analyzed. The LBM simulations demonstrated some deficiencies in the prediction of noise mainly at low St and low radiation angles for $M = 0.4$. Moreover, inconsistencies were present on the boundary layer profiles at the nozzle exit. Even greater limitations were found with the LBM approach for $M = 0.9$. The accuracy of the results was not considered enough for the analysis. On the other hand, the LES performed by Brès *et al.* (2015) showed very good agreement with experimental data for both flow and acoustic fields and, hence, its corresponding database was used in the present study.

Based on the LES data, the source term from Lighthill's equation was simplified and, using a two-point statistics approach, the generated acoustic fields were obtained and discussed. For the free-jet case, significant sensitivity of the sound levels was observed regarding the window function used to evaluate the source cross-spectral densities. Overall, results using rectangular window were not suitable, presenting large sensitivity to the block size in comparison to Hanning and hyperbolic tangent windows. Therefore, the suitable choice of the window function is important to avoid errors in the acoustic field computation. The main features of the sound field for the isolated jet at low St and low directivity angles could be obtained by considering only the linear part of the $T_{xx}(m = 0)$ source term extracted from the LES. Moreover, this term was shown to hold the main contribution to the jet-plate scattered field, confirming the observations from Cavalieri *et al.* (2014) by using a LES database.

After analyzing the main characteristics of the source field, a six-parameter volumetric source model was adjusted by minimizing the squared error with respect to the LES CSD. The model failed to predict both the magnitude and directivity of the free-jet at low angles. As the St increased, so did the deviations from the experimental data. The main reasons for such deviations may be the difficulties in reproducing the complexity of the CSD and coherence profiles from the LES data. On the other hand, the installed jet noise did not seem to be very sensitive to these deviations at the source region. The model showed good prediction of experimental noise field whenever the edge scattering effects were dominant, specially for $St = 0.3$.

Sensitivity to the modeled coherence was also investigated. The free-jet noise presented high sensitivity to the source coherence length. However, the installed jet results were practically unaffected by the variations of the coherence parameter at positions and St in which trailing-edge scattering was dominant.

The use of simpler source models, such as a line source adjusted with radially integrated LES data, proved to be effective. This approach resulted in improved agreement with experimental data, which was a consequence of involving less uncertainties in the fitting process. The results showed that simple models such as the ones used by Cavalieri and Agarwal (2014) and Nogueira *et al.* (2017) are able to correctly predict the noise levels for both installed and isolated jets, as long as they are provided with consistent source data.

Difficulties still lie in the prediction of both the levels and directivity of free-jet at high St. The prediction of noise at this St range may require more complex models. However, at $St = 0.75$ for instance, the axisymmetric mode has small contributions to the total noise, in comparison with the lower St range. In addition, trailing-edge effects are not dominant in this St range. Therefore, it may not be worth the effort of introducing complex parameters in such models for predicting both the isolated and installed jet noise.

In summary, simple wavepacket models adjusted with flow field data showed great capability of reproducing noise levels and directivity, specially for installed jets, with very low computational effort. The prediction for the installed jet was much less sensitive to fitting errors, specially to variations on the coherence, except when the coherence length value is too small and the source approaches

the compact limit. In this sense, modeling for installed jets was found to be much simpler than for the isolated jet.

7.1 SUGGESTIONS FOR FUTURE WORK

Despite being possible to observe important characteristics of the scattered fields with the $M = 0.9$ data, installation effects are not so prominent at high Mach numbers. Therefore, a similar study could be done for lower Mach number, in order to find the corresponding model parameters and analyze the installation effects more clearly.

It would also be interesting to quantify the contribution of the missing Lighthill's tensor terms, as well as the missing azimuthal modes. Moreover, at $M = 0.9$ filtering techniques could be used to eliminate the influence of the trapped acoustic waves in the potential core. This would lead to more confidence in fitting the data for other St values, say 0.4 and 0.5, thus reducing fitting errors and possibly improving the noise prediction.

Regarding the modeling, more effort could be directed to improve the model source, specially for the prediction of the free-jet noise at higher St. For reducing the errors in the parameter adjustment process, other methods, such as sparse regression, could be analyzed.

As discussed in Chapter 6, for the volumetric source, very low levels of the modeled PSD ad CSDs around the lipline and near the plate trailing-edge were observed. Centering the Gaussian function for the radial amplitude at other positions close to the lipline could be an option to reduce the disparities between the LES and modeled sources and possibly improve the results for both installed and isolated jets. Another suggestion is to consider the effects radial phase differences, radial coherence decay and the use of a function that better represents the asymmetric characteristics of the streamwise amplitude decay. Obviously, the increasing complexity of the modeling should be balanced with the objective of finding a simple and useful representation of the phenomenon.

Furthermore, the model should be extended to more complex geometries, closer to industrial applications. The effects of flap deflection should be also accounted. The present models are also not valid for plate positions $r/D < 1$, since a stronger deformation of the jet flow is expected, along with the formation

of a boundary layer which may also contribute to the noise field (PIANTANIDA *et al.*, 2016b). Other approaches may be necessary for such configurations.

BIBLIOGRAPHY

ARMSTRONG, R.; MICHALKE, A.; FUCHS, H. Coherent structures in jet turbulence and noise. *AIAA Journal*, v. 15, p. 1011, 1977.

BAILLY, C.; CANDEL, S.; LAFON, P. Prediction of supersonic jet noise from a statistical acoustic model and a compressible turbulence closure. *Journal of Sound and Vibration*, v. 194, n. 2, p. 219 – 242, 1996. ISSN 0022-460X.

BAQUI, Y. B.; AGARWAL, A.; CAVALIERI, A. V. G.; SINAYOKO, S. A coherence-matched linear source mechanism for subsonic jet noise. *Journal of Fluid Mechanics*, v. 776, p. 235–267, 8 2015. ISSN 1469-7645.

BASTIN, F.; LAFON, P.; CANDEL, S. Computation of jet mixing noise due to coherent structures: the plane jet case. *Journal of Fluid Mechanics*, Cambridge University Press, v. 335, p. 261–304, Mar 1997.

BATCHELOR, G. K.; GILL, A. Analysis of the stability of axisymmetric jets. *Journal of Fluid Mechanics*, v. 14, p. 529–551, 1962.

BHAT, T. R. S.; BLACKNER, A. M. Installed jet noise prediction model for coaxial jets. In: *36th AIAA Aerospace Sciences Meeting and Exhibit*. [S.l.]: American Institute of Aeronautics and Astronautics, 1998. (AIAA-98-0080).

BHATNAGAR, P. L.; GROSS, E. P.; KROOK, M. A model for collision processes in gases. i. small amplitude processes in charged and neutral one-component systems. *Phys. Rev.*, American Physical Society, v. 94, p. 511–525, May 1954.

BLACKNER, A. M.; BHAT, T. R. S. Installation effects on coaxial jet noise - an experimental study. In: *36th AIAA Aerospace Sciences Meeting and Exhibit*. [S.l.]: American Institute of Aeronautics and Astronautics, 1998.

BODART, J.; LARSSON, J. Wall-modeled large eddy simulation in complex geometries with application to high-lift devices. In: *Annual Research Briefs*. Stanford, CA: Center for Turbulence Research, Stanford University, 2011.

BODART, J.; LARSSON, J. *Wall-modeled large eddy simulation of the McDonnell-Douglas 30P/30N high-lift airfoil in near-stall conditions*. 2012. AIAA paper 2012-3022.

BODONY, D. J.; LELE, S. K. Low-frequency sound sources in high-speed turbulent jets. *Journal of Fluid Mechanics*, Cambridge University Press, Cambridge, UK, v. 617, p. 231–253, 12 2008.

BOGEY, C.; BAILLY, C. Investigation of downstream and sideline subsonic jet noise using large eddy simulation. *Theoretical and Computational Fluid Dynamics*, Springer-Verlag, v. 20, n. 1, p. 23–40, 2006. ISSN 0935-4964.

BOGEY, C.; BAILLY, C. On the importance of specifying appropriate nozzle-exit conditions in jet noise prediction. *Procedia Engineering*, v. 6, p. 38 – 43, 2010. ISSN 1877-7058.

BOGEY, C.; BAILLY, C.; JUVÉ, D. Noise investigation of a high subsonic, moderate reynolds number jet using a compressible large eddy simulation. *Theoretical and Computational Fluid Dynamics*, Springer-Verlag, v. 16, n. 4, p. 273–297, 2003. ISSN 0935-4964.

BOGEY, C.; MARSDEN, O.; BAILLY, C. Effects of moderate reynolds numbers on subsonic round jets with highly disturbed nozzle-exit boundary layers. *Physics of Fluids*, v. 24, n. 10, p. 105107, 2012.

BOGEY, C.; MARSDEN, O.; BAILLY, C. Influence of initial turbulence level on the flow and sound fields of a subsonic jet at a diameter-based reynolds number of 105. *Journal of Fluid Mechanics*, Cambridge University Press, v. 701, p. 352–385, 2012.

BONDAREKO, M.; HU, Z.; ZHANG, X. Large-eddy simulation of the interaction of a jet with a wing. In: *18th AIAA/CEAS Aeroacoustics Conference*. [S.l.]: American Institute of Aeronautics and Astronautics, 2012.

BREAKEY, D. E.; JORDAN, P.; CAVALIERI, A.; LÉON, O.; ZHANG, M.; LESHNASCH, G.; COLONIUS, T.; RODRÍGUEZ, D. Near-field wavepackets and the far-field sound of a subsonic jet. In: . [S.l.]: American Institute of Aeronautics and Astronautics, 2013.

BRÈS, G.; NICHOLS, J.; LELE, S.; HAM, F.; SCHLINKER, R.; REBA, R.; SIMONICH, J. Unstructured large eddy simulation of a

hot supersonic over-expanded jet with chevrons. In: *Aeroacoustics Conferences*. [S.l.]: American Institute of Aeronautics and Astronautics, 2012.

BRÈS, G.; PÉROT, F.; FREED, D. A ffowcs williams - hawkings solver for lattice-boltzmann based computational aeroacoustics. In: *16th AIAA/CEAS Aeroacoustics Conference*. [S.l.]: American Institute of Aeronautics and Astronautics, 2010.

BRÈS, G. A.; JAUNET, V.; RALLIC, M. L.; JORDAN, P.; COLONIUS, T.; LELE, S. K. Large eddy simulation for jet noise: the importance of getting the boundary layer right. In: *AIAA Aviation*. [S.l.]: American Institute of Aeronautics and Astronautics, 2015. p. –.

BRÈS, G. A.; JAUNET, V.; RALLIC, M. L.; JORDAN, P.; TOWNE, A.; SCHMIDT, O.; COLONIUS, T.; CAVALIERI, A. V.; LELE, S. K. Large eddy simulation for jet noise: azimuthal decomposition and intermittency of the radiated sound. In: . [S.l.]: American Institute of Aeronautics and Astronautics, 2016.

BRÈS, G. A.; JORDAN, P.; COLONIUS, T.; RALLIC, M. L.; JAUNET, V.; LELE, S. K. Large eddy simulation of a Mach 0.9 turbulent jet. In: *Proceedings of the Summer Program*. [S.l.]: Center for Turbulence Research, Stanford University, 2014.

BRÈS, G. A.; PÉROT, F.; FREED, D. Properties of the lattice-boltzmann method for acoustics. In: *15th AIAA/CEAS Aeroacoustics Conference*. [S.l.]: American Institute of Aeronautics and Astronautics, 2009. (AIAA2009-3395).

CASALINO, D.; LELE, S. K. Lattice-boltzmann simulation of coaxial jet noise generation. In: CENTER FOR TURBULENCE RESEARCH. *Proceedings of the Summer Program 2014*. [S.l.], 2014.

CASALINO, D.; RIBEIRO, A. F.; FARES, E. Facing rim cavities fluctuation modes. *Journal of Sound and Vibration*, v. 333, n. 13, p. 2812 – 2830, 2014. ISSN 0022-460X.

CASALINO, D.; RIBEIRO, A. F. P.; FARES, E.; NÖLTING, S. Lattice-boltzmann aeroacoustic analysis of the lagoon landing-gear configuration. *AIAA Journal*, American Institute of Aeronautics and Astronautics, v. 52, n. 6, p. 1232–1248, Apr. 2014. ISSN 0001-1452.

CAVALIERI, A. V.; DAVILLER, G.; COMTE, P.; JORDAN, P.; TADMOR, G.; GERVAIS, Y. Using large eddy simulation to explore sound-source mechanisms in jets. *Journal of Sound and Vibration*, v. 330, n. 17, p. 4098 – 4113, 2011a. ISSN 0022-460X.

CAVALIERI, A. V.; DONADON, M. V.; WOLF, W. Acoustic scattering by finite composite plates. In: . [S.l.]: American Institute of Aeronautics and Astronautics, 2015.

CAVALIERI, A. V.; JORDAN, P.; AGARWAL, A.; GERVAIS, Y. Jittering wave-packet models for subsonic jet noise. *Journal of Sound and Vibration*, v. 330, p. 4474 – 4492, 2011b. ISSN 0022-460X.

CAVALIERI, A. V.; JORDAN, P.; WOLF, W. R.; GERVAIS, Y. Scattering of wavepackets by a flat plate in the vicinity of a turbulent jet. *Journal of Sound and Vibration*, v. 333, n. 24, p. 6516–6531, 2014. ISSN 0022-460X.

CAVALIERI, A. V. G. *Wavepackets as sound-source mechanisms in subsonic jets*. Phd Thesis (Doutorado) — Science et Ingénierie en Materiaux, Méchanique, Énergétique et Aéronautique - Université de Poitiers, Franca, 2012.

CAVALIERI, A. V. G.; AGARWAL, A. Coherence decay and its impact on sound radiation by wavepackets. *Journal of Fluid Mechanics*, v. 748, p. 399–415, 6 2014. ISSN 1469-7645.

CAVALIERI, A. V. G.; JORDAN, P.; COLONIUS, T.; GERVAIS, Y. Axisymmetric superdirectivity in subsonic jets. *Journal of Fluid Mechanics*, v. 704, p. 388–420, 8 2012. ISSN 1469-7645.

CAVALIERI, A. V. G.; RODRÍGUEZ, D.; JORDAN, P.; COLONIUS, T.; GERVAIS, Y. Wavepackets in the velocity field of turbulent jets. *Journal of Fluid Mechanics*, v. 730, p. 559–592, 9 2013. ISSN 1469-7645.

CHEN, H.; FILIPPOVA, O.; HOCH, J.; MOLVIG, K.; SHOCK, R.; TEIXEIRA, C.; ZHANG, R. Grid refinement in lattice boltzmann methods based on volumetric formulation. *Physica A: Statistical Mechanics and its Applications*, v. 362, n. 1, p. 158 – 167, 2006. ISSN 0378-4371.

CHEN, H.; TEIXEIRA, C.; MOLVIG, K. Realization of fluid boundary conditions via discrete boltzmann dynamics.

International Journal of Modern Physics C, v. 09, n. 08, p. 1281–1292, 1998.

Committee on Environmental Health. Noise: A hazard for the fetus and newborn. *Pediatrics*, v. 100, n. 4, p. 724–727, Oct. 1997.

CRIGHTON, D. Basic principles of aerodynamic noise generation. *Progress in Aerospace Sciences*, v. 16, n. 1, p. 31 – 96, 1975. ISSN 0376-0421.

CRIGHTON, D. G.; GASTER, M. Stability of slowly diverging jet flow. *J. Fluid Mech.*, v. 77, p. 397, 1976.

CRIGHTON, D. G.; HUERRE, P. Shear-layer pressure fluctuations and superdirective acoustic sources. *Journal of Fluid Mechanics*, v. 220, p. 355–368, 11 1990. ISSN 1469-7645.

CROUSE, B.; FREED, D.; BALASUBRAMANIAN, G.; SENTHOORAN, S.; LEW, P.-T.; MONGEAU, L. Fundamental aeroacoustic capabilities of the lattice-boltzmann method. In: *12th AIAA/CEAS Aeroacoustics Conference*. [S.l.]: American Institute of Aeronautics and Astronautics, 2006.

CROW, S. C. Acoustic gain of a turbulent jet. In: *Phys. Soc. Meeting, Univ. Colorado, Boulder*. [S.l.: s.n.], 1972. v. 6, n. paper IE.

CROW, S. C.; CHAMPAGNE, F. H. Orderly structure in jet turbulence. *Journal of Fluid Mechanics*, v. 48, p. 547–591, 1971.

CURLE, N. The influence of solid boundaries upon aerodynamic sound. *Proceedings of the Royal Society of London*, n. 231 A, p. 505–517, 1955.

DEARDORFF, J. W. A numerical study of three-dimensional turbulent channel flow at large reynolds numbers. *Journal of Fluid Mechanics*, v. 41, p. 453–480, 4 1970. ISSN 1469-7645.

DI FRANCESCANTONIO, P. A new boundary integral formulation for the prediction of sound radiation. *Journal of Sound and Vibration*, 1997.

ELKOBY, R. Full-scale propulsion airframe aeroacoustics investigation. In: *11th AIAA/CEAS Aeroacoustics Conference*. [S.l.]: American Institute of Aeronautics and Astronautics, 2005.

EMBRAER. 2014. Available: <http://www.embraercommercialaviation.com/Pages/Ejets-170.aspx>.

FARANOSOV, G. A.; GOLOVIZNIN, V. M.; KARABASOV, S. A.; KONDAKOV, V. G.; KOPIEV, V. F.; ZAITSEV, M. A. CABARET method on unstructured hexahedral grids for jet noise computation. *Computers & Fluids*, v. 88, n. 0, p. 165 – 179, 2013. ISSN 0045-7930.

FARES, E. Unsteady flow simulation of the ahmed reference body using a lattice boltzmann approach. *Computers & Fluids*, v. 35, p. 940 – 950, 2006. ISSN 0045-7930. Proceedings of the First International Conference for Mesoscopic Methods in Engineering and Science.

FFOWCS WILIAMS, J. E.; LIGHTHILL, M. J. *Aerodynamic generation of sound*. 1971. Film Notes. National Committee for Fluid Mechanics Films.

FFOWCS WILLIAMS, J. E.; HALL, L. H. Aerodynamic sound generation by turbulent flow in the vicinity of a scattering half plane. *Journal of Fluid Mechanics*, v. 40, p. 657–670, 1970.

FFOWCS WILLIAMS, J. E.; HAWKINGS, D. L. Sound generation by turbulence and surfaces in arbitrary motion. *Philosophical Transactions of the Royal Society of London. Series A, Mathematical and Physical Sciences*, The Royal Society, v. 264, n. 1151, p. 321–342, May 1969. ISSN 00804614.

FFOWCS WILLIAMS, J. E.; KEMPTON, A. J. The noise from the large-scale structure of a jet. In: FIEDLER, H. (Ed.). *Structure and Mechanisms of Turbulence II: Proceedings of the Symposium on Turbulence Held at the Technische Universität Berlin, August 1–5, 1977*. Berlin, Heidelberg: Springer Berlin Heidelberg, 1978. p. 265–272. ISBN 978-3-540-35830-5.

FFOWCS WILLIAMS, J. E.; MAIDANIK, G. The mach wave field radiated by supersonic turbulent shear flows. *Journal of Fluid Mechanics*, v. 21, p. 641–657, 4 1965. ISSN 1469-7645.

FLEMING, G. G.; ZIEGLER, U. R. F. Environmental trends in aviation to 2050. In: _____. *ICAO Environmental Report 2013*. [S.l.]: International Civil Aviation Organization (ICAO), 2013. p. 22–27.

FREUND, J. B. Noise sources in a low-Reynolds-number turbulent jet at mach 0.9. *J. Fluid Mech.*, v. 438, p. 277, 2001.

FREUND, J. B. Noise-source turbulence statistics and the noise from a mach 0.9 jet. *Physics of Fluids*, v. 15, n. 6, p. 1788–1799, 2003.

FUCHS, H. Space correlations of the fluctuating pressure in subsonic turbulent jets. *Journal of Sound and Vibration*, v. 23, n. 1, p. 77 – 99, 1972. ISSN 0022-460X.

FUCHS, H. V.; MICHEL, U. Experimental evidence of turbulent source coherence affecting jet noise. *AIAA Journal*, American Institute of Aeronautics and Astronautics, v. 16, n. 9, p. 871–872, Sep. 1978. ISSN 0001-1452.

GOPALAKRISHNAN, P.; LI, Y.; ZHANG, R.; CHEN, H. Computation of high-subsonic and transonic flows by a lattice Boltzmann method. In: . [S.l.]: American Institute of Aeronautics and Astronautics, 2016.

GUDMUNDSSON, K.; COLONIUS, T. Instability wave models for the near-field fluctuations of turbulent jets. *Journal of Fluid Mechanics*, Cambridge University Press, Cambridge, UK, v. 689, p. 97–128, 12 2011.

GUJ, G.; CARLEY, M.; CAMUSSI, R.; RAGNI, A. Acoustic identification of coherent structures in a turbulent jet. *Journal of Sound and Vibration*, v. 259, n. 5, p. 1037 – 1065, 2003. ISSN 0022-460X.

HABIBI, K.; GONG, H.; NAJAFI-YAZDI, A.; MONGEAU, L. Numerical simulations of sound radiated from internal mixing nozzles with forced mixers using the lattice boltzmann method. In: *19th AIAA/CEAS Aeroacoustics Conference*. [S.l.]: American Institute of Aeronautics and Astronautics, 2013.

HABIBI, K.; MONGEAU, L. G.; CASALINO, D.; LEW, P.-T. Aeroacoustic study of internal mixing nozzles with forced lobed mixers using a high-mach subsonic lattice Boltzmann scheme. In: . [S.l.]: American Institute of Aeronautics and Astronautics, 2014, (AIAA AVIATION Forum).

HABIBI, K.; NAJAFI-YAZDI, A.; LEW, P.-T.; MONGEAU, L. Simulation of sound radiated from turbulent heated jets

using the lattice-Boltzmann method. In: *17th AIAA/CEAS Aeroacoustics Conference*. [S.l.]: American Institute of Aeronautics and Astronautics, 2011.

HALL, A. M.; GLAUSER, M. N.; TINNEY, C. E. Experimental investigation of the pressure-velocity correlation of a M=0.6 axisymmetric jet. In: *35th AIAA Fluid Dynamics Conference and Exhibit*. [S.l.]: American Institute of Aeronautics and Astronautics, 2005. (AIAA 2005-5294).

HE, X.; LUO, L.-S. Theory of the lattice boltzmann method: From the Boltzmann equation to the lattice Boltzmann equation. *Physical Review*, v. 56, n. 6, 1997.

HEGELE, L. A. J. *Equação de Boltzmann em Rede para Escoamentos Térmicos*. Phd Thesis (PhD Thesis) — Universidade Federal de Santa Catarina, Programa de Pós-Graduação em Engenharia Mecânica, 2010.

HILEMAN, J. I.; THUROW, B. S.; CARABALLO, E. J.; SAMIMY, M. Large-scale structure evolution and sound emission in high-speed jets: real-time visualization with simultaneous acoustic measurements. *Journal of Fluid Mechanics*, v. 544, p. 277–307, 12 2005. ISSN 1469-7645.

HÜTTL, T. The importance of aeroacoustics research. In: WAGNER, C.; HÜTTL, T.; SAGAUT, P. (Ed.). *Large-Eddy Simulation for Acoustics*. New York: Cambridge University Press, 2007. chap. 1.1, p. 1–6.

ICAO. *International Standards and Recommended Practices. Environment Protection. Annex 16 to the Convention on International Civil Aviation. Volume I: Aircraft Noise*. 2008.

ICAO. *ICAO Environmental Report 2010*. Québec, Canada, 2010.

ICAO. *ICAO Environmental Report 2013*. Québec, Canada, 2013.

JAUNET, V.; JORDAN, P.; CAVALIERI, A. V.; TOWNE, A.; COLONIUS, T.; SCHMIDT, O.; BRÈS, G. A. Tonal dynamics and sound in subsonic turbulent jets. In: *22nd AIAA/CEAS Aeroacoustics Conference*. [S.l.]: American Institute of Aeronautics and Astronautics, 2016.

JAUNET, V.; JORDAN, P.; CAVALIERI, A. V. G. Two-point coherence of wave packets in turbulent jets. *Phys. Rev. Fluids*, American Physical Society, v. 2, p. 024604, Feb 2017.

JORDAN, P.; COLONIUS, T. Wave packets and turbulent jet noise. *Annual Review of Fluid Mechanics*, v. 45, n. 1, p. 173–195, 2013.

JORDAN, P.; COLONIUS, T.; BRÈS, G. A.; ZHANG, M.; TOWNE, A.; LELE, S. K. Modeling intermittent wavepackets and their radiated sound in a turbulent jet. In: *Center for Turbulent Research - Proceedings of the Summer Program 2014*. [S.l.: s.n.], 2014.

JORDAN, P.; GERVAIS, Y. Modelling self- and shear-noise mechanisms in inhomogeneous, anisotropic turbulence. *Journal of Sound and Vibration*, v. 279, n. 3-5, p. 529 – 555, 2005. ISSN 0022-460X.

JORDAN, P.; GERVAIS, Y. Subsonic jet aeroacoustic: associating experiment, modemodel and simulation. *Experiments in Fluids*, v. 44, p. 1–21, 2008.

JUVÉ, D.; SUNYACH, M.; COMTE-BELLOT, G. Filtered azimuthal correlations in the acoustic far field of a subsonic jet. *AIAA Journal*, American Institute of Aeronautics and Astronautics, v. 17, n. 1, p. 112–113, Jan. 1979. ISSN 0001-1452.

JUVÉ, D.; SUNYACH, M.; COMTE-BELLOT, G. Intermittency of the noise emission in subsonic cold jets. *Journal of Sound and Vibration*, v. 71, n. 3, p. 319 – 332, 1980. ISSN 0022-460X.

KAWAI, S.; LARSSON, J. Wall-modeling in large eddy simulation: Length scales, grid resolution, and accuracy. v. 24(015105), 2012.

KERHERVÉ, F.; FITZPATRICK, J.; JORDAN, P. The frequency dependence of jet turbulence for noise source modelling. *Journal of Sound and Vibration*, v. 296, n. 1-2, p. 209 – 225, 2006. ISSN 0022-460X.

KERHERVÉ, F.; JORDAN, P.; CAVALIERI, A. V. G.; DELVILLE, J.; BOGEY, C.; JUVÉ, D. Educing the source mechanism associated with downstream radiation in subsonic jets. *Journal of Fluid Mechanics*, Cambridge University Press, Cambridge, UK, v. 710, p. 606–640, 11 2012.

KERHERVÉ, F.; JORDAN, P.; GERVAIS, Y.; VALIÈRE, J.-C.; BRAUD, P. Two-point laser Doppler velocimetry measurements in a mach 1.2 cold supersonic jet for statistical aeroacoustic source model. *Experiments in Fluids*, v. 37, n. 3, p. 419–437, 2004. ISSN 1432-1114.

KESSLER, M. Introduction to computational aeroacoustics. In: WAGNER, C.; HÜTTL, T.; SAGAUT, P. (Ed.). *Large-Eddy Simulation for Acoustics*. New York: Cambridge University Press, 2007. chap. 1.2, p. 7–14.

KHALIGHI, Y.; HAM, F.; NICHOLS, J.; LELE, S.; MOIN, P. Unstructured large eddy simulation for prediction of noise issued from turbulent jets in various configurations. In: *Aeroacoustics Conferences*. [S.l.]: American Institute of Aeronautics and Astronautics, 2011.

KLEINMAN, R. R.; FREUND, J. B. The sound from mixing layers simulated with different ranges of turbulence scales. *Physics of Fluids*, v. 20, n. 10, p. 101503, 2008.

KOENIG, M.; CAVALIERI, A. V.; JORDAN, P.; DELVILLE, J.; GERVAIS, Y.; PAPAMOSCHOU, D. Farfield filtering and source imaging of subsonic jet noise. *Journal of Sound and Vibration*, v. 332u, n. 18, p. 4067 – 4088, 2013. ISSN 0022-460X.

KOPIEV, V. F.; FARANOSOV, G. A.; ZAYTSEV, M. Y.; VLASOV, E. V.; KARAVOSOV, R. K.; BELYAEV, I. V.; OSTRIKOV, N. N. Intensification and suppression of jet noise sources in the vicinity of lifting surfaces. In: *19th AIAA/CEAS Aeroacoustics Conference*. [S.l.]: American Institute of Aeronautics and Astronautics, 2013.

LABBÉ, O.; PEYRET, C.; RAHIER, G.; HUET, M. A CFD/CAA coupling method applied to jet noise prediction. *Computers & Fluids*, v. 86, n. 0, p. 1 – 13, 2013. ISSN 0045-7930.

LATT, J.; CHOPARD, B. Lattice boltzmann method with regularized pre-collision distribution functions. *Mathematics and Computers in Simulation*, v. 72, n. 2, p. 165 – 168, 2006. ISSN 0378-4754. Discrete Simulation of Fluid Dynamics in Complex Systems.

LAU, J.; FISHER, M.; FUCHS, H. The intrinsic structure of turbulent jets. *Journal of Sound and Vibration*, v. 22, n. 4, p. 379 – 406, 1972. ISSN 0022-460X.

LAUNDER, B.; SPALDING, D. The numerical computation of turbulent flows. *Computer Methods in Applied Mechanics and Engineering*, v. 3, n. 2, p. 269 – 289, 1974. ISSN 0045-7825.

LAWRENCE, J. *Aeroacoustic Interactions of Installed Subsonic Round Jets*. PhD Thesis — University of Southampton, Faculty of Engineering and the Environment, 2014.

LAWRENCE, J.; SELF, R. H. Installed jet-flap impingement tonal noise. In: . [S.l.]: American Institute of Aeronautics and Astronautics, 2015.

LAWRENCE, J. L. T.; AZARPEYVAND, M.; SELF, R. H. Interaction between a flat plate and a circular subsonic jet. In: *17th AIAA/CEAS Aeroacoustics Conference*. [S.l.]: American Institute of Aeronautics and Astronautics, 2011.

LECONTE, J. On the influence of musical sounds on the flame of a jet of coal-gas. *Philosophical Magazine Series 4*, v. 15, n. 99, p. 235–239, 1858.

LELE, S. K.; MENDEZ, S.; RYU, J.; NICHOLS, J.; SHOEYBI, M.; MOIN, P. Sources of high-speed jet noise: Analysis of les data and modeling. *Procedia Engineering*, v. 6, p. 84 – 93, 2010. ISSN 1877-7058.

LÉON, O.; BRAZIER, J.-P. Application of the linear parabolized stability equations to a subsonic coaxial jet. In: . [S.l.]: American Institute of Aeronautics and Astronautics, 2011.

LEW, P.-T.; GOPALAKRISHNAN, P.; CASALINO, D.; SHOCK, R.; LI, Y.; ZHANG, R.; CHEN, H.; HABIBI, K.; MONGEAU, L. G. An extended lattice Boltzmann methodology for high subsonic jet noise prediction. In: *AIAA Aviation - 20th AIAA/CEAS Aeroacoustics Conference*. [S.l.]: American Institute of Aeronautics and Astronautics, 2014.

LEW, P.-T.; MONGEAU, L.; LYRINTZIS, A. Noise prediction of a subsonic turbulent round jet using the lattice-Boltzmann method. *The Journal of the Acoustical Society of America*, v. 128, n. 3, p. 1118–1127, 2010.

LEW, P.-T.; NAJAFI-YAZDI, A.; MONGEAU, L. Unsteady numerical simulation of a round jet with impinging microjets for noise suppression. *The Journal of the Acoustical Society of America*, v. 134, n. 3, p. 1982–1989, 2013.

LIGHTHILL, M. J. On sound generated aerodynamically. I. general theory. *Proceedings of the Royal Society of London. Series A. Mathematical and Physical Sciences*, v. 211, n. 1107, p. 564–587, 1952.

LIGHTHILL, M. J. On sound generated aerodynamically. II. turbulence as a source of sound. *Proceedings of the Royal Society of London. Series A. Mathematical and Physical Sciences*, v. 222, n. 1148, p. 1–32, 1954.

LU, H. Y. An empirical model for prediction of coaxial jet noise in ambient flow. In: *10th AIAA/CEAS Aeroacoustics Conference*. [S.l.]: American Institute of Aeronautics and Astronautics, 1986.

LYUBIMOV, D. Investigation of the effect of a pylon and a wing with flaps on the flow within an exhaust jet of a double-flow turbojet engine by a simulation method for large eddies. *High Temperature*, SP MAIK Nauka/Interperiodica, v. 51, n. 1, p. 111–127, 2013. ISSN 0018-151X.

MAESTRELLO, L. *Two-Point Correlations of Sound Pressure in the Far Field of a Jet: Experiment*. [S.l.], 1976.

MARTÍNEZ-LERA, P.; SCHRAM, C. Correction techniques for the truncation of the source field in acoustic analogies. *The Journal of the Acoustical Society of America*, v. 124, n. 6, p. 3421–3429, 2008.

MATHIEU, J.; SCOTT, J. *An Introduction to Turbulent Flow*. [S.l.]: Cambridge University Press, 2000. ISBN 9780521775380.

MC LAUGHLIN, P.; SELF, R. H.; POWLES, C. J.; WRIGHTON, C.; STRANGE, P. J. R.; MOORE, A. D. High frequency jet noise installation effects for and under wing mounted aircraft. In: *14th AIAA/CEAS Aeroacoustics Conference*. [S.l.]: American Institute of Aeronautics and Astronautics, 2008.

MC LAUGHLIN, P.; SELF, R. H.; STRANGE, P. J. R.; MOORE, A. D. A 3-dimensional installation effects prediction method for a distributed jet source. In: *13th AIAA/CEAS Aeroacoustics Conference*. [S.l.]: American Institute of Aeronautics and Astronautics, 2007. (AIAA2007-3607).

MEAD, C. J.; STRANGE, P. J. R. Under-wing installation effects on jet noise at sideline. In: *4th AIAA/CEAS Aeroacoustics*

Conference. [S.l.]: American Institute of Aeronautics and Astronautics, 1998.

MENGLE, V. G. The effect of nozzle-to-wing gulley height on jet flow attachment to the wing and jet-flap interaction noise. In: *17th AIAA/CEAS Aeroacoustics Conference*. [S.l.]: American Institute of Aeronautics and Astronautics, 2011.

MENGLE, V. G.; STOKER, R. W.; BRUSNIAK, L.; ELKOBY, R. Flaperon modification effect on jet-flap interaction noise reduction for chevron nozzles. In: *13th AIAA/CEAS Aeroacoustics Conference*. [S.l.]: American Institute of Aeronautics and Astronautics, 2007.

MICHALKE, A. *A Wave Model for Sound Generation in Circular Jets*. [S.l.]: Zentralstelle für Luftfahrtdokumentation und -information, 1970. (Deutsche Luft- und Raumfahrt: Forschungsbericht).

MICHALKE, A. *Instability of a compressible circular free jet with consideration of the Influence of the jet boundary layer*. [S.l.], 1977.

MICHALKE, A.; FUCHS, H. On turbulence and noise of an axisymmetric shear flow. *J. Fluid Mech.*, v. 70, p. 179, 1975.

MOLLO-CHRISTENSEN, E. *Measurements of near field ppressure of subsonic jets*. [S.l.], 1963.

MOLLO-CHRISTENSEN, E. Jet noise and shear flow instability seen from an experimenter's viewpoint. *Journal of Applied Mechanics*, v. 34, n. 1, p. 1–7, Mar. 1967. ISSN 0021-8936.

MOLLO-CHRISTENSEN, E.; KOLPIN, M. A.; MARTUCCELLI, J. R. Experiments on jet flows and jet noise far-field spectra and directivity patterns. *Journal of Fluid Mechanics*, Cambridge University Press, v. 18, n. 2, p. 285–301, 1964.

MOORE, C. J. The role of shear-layer instability waves in jet exhaust noise. *Journal of Fluid Mechanics*, Cambridge University Press, v. 80, n. 2, p. 321–367, 1977.

MOORE, P. D. *Aeroacoustics of compressible Subsonic jets - Direct Numerical Simulation of a low Reynolds number subsonic jet and the associated sound field*. Phd Thesis (PhD Thesis) — Technische Universiteit Delft, 2009.

MORRIS, P. J.; ZAMAN, K. Velocity measurements in jets with application to noise source modeling. *Journal of Sound and Vibration*, v. 329, n. 4, p. 394 – 414, 2010. ISSN 0022-460X.

NAJAFI-YAZDI, A.; BRÈS, G. A.; MONGEAU, L. An acoustic analogy formulation for moving sources in uniformly moving media. *Proceedings of the Royal Society of London A: Mathematical, Physical and Engineering Sciences*, The Royal Society, 2010. ISSN 1364-5021.

NELDER, J. A.; MEAD, R. A simplex method for function minimization. *The Computer Journal*, v. 7, n. 4, p. 308, 1965.

NELSON, P. *Transportation noise reference book*. [S.l.]: Butterworth, 1987. ISBN 9780408014465.

NIE, X.; SHAN, X.; CHEN, H. A lattice-boltzmann / finite-difference hybrid simulation of transonic flow. In: . [S.l.]: American Institute of Aeronautics and Astronautics, 2009, (Aerospace Sciences Meetings).

NOGUEIRA, P. A.; CAVALIERI, A. V.; JORDAN, P. A model problem for sound radiation by an installed jet. *Journal of Sound and Vibration*, v. 391, p. 95 – 115, 2017. ISSN 0022-460X.

NOGUEIRA, P. A.; PIANTANIDA, S.; CAVALIERI, A. V.; JORDAN, P. Pse-based prediction of sound radiation by installed jets. In: *22nd AIAA/CEAS Aeroacoustics Conference*. [S.l.]: American Institute of Aeronautics and Astronautics, 2016, (Aeroacoustics Conferences).

NOGUEIRA, P. A. S.; PIANTANIDA, S.; CAVALIERI, A. V. G.; JORDAN, P. Pse-based prediction of sound radiation by installed jets. In: *22nd AIAA/CEAS Aeroacoustics Conference*. [S.l.: s.n.], 2016.

PANDA, J.; SEASHOLTZ, R. G.; ELAM, K. A. Investigation of noise sources in high-speed jets via correlation measurements. *Journal of Fluid Mechanics*, v. 537, p. 349–385, 8 2005. ISSN 1469-7645.

PASTOUCHENKO, N. N.; TAM, C. K. W. Installation effects on the flow and noise of an under-the-wing mounted dual stream jet. In: *43rd AIAA Aerospace Sciences Meeting and Exhibit*. [S.l.]: American Institute of Aeronautics and Astronautics, 2005. (AIAA2005-604).

PHILIPPI, P. C.; HEGELE, L. A. J.; SANTOS, L. O. E. dos; SURMAS, R. From the continuous to the lattice Boltzmann equation: The discretization problem and thermal models. *Physical Review*, v. 73, 2006.

PHILIPPI, P. C.; HEGELE, L. A. J.; SURMAS, R.; SIEBERT, D. N.; SANTOS, L. O. E. dos. From the Boltzmann to the lattice-Boltzmann equation: Beyond BGK collision models. *International Journal of Modern Physics C*, v. 18, n. 4, p. 556–565, 2007.

PIANTANIDA, S.; CAVALIERI, A. V.; WOLF, W.; DANADON, M.; JORDAN, P. Scattering of turbulent-jet wavepackets by a flexible composite plate. In: . [S.l.]: American Institute of Aeronautics and Astronautics, 2016.

PIANTANIDA, S.; JAUNET, V.; HUBER, J.; WOLF, W. R.; JORDAN, P.; CAVALIERI, A. V. G. Scattering of turbulent-jet wavepackets by a swept trailing edge. *The Journal of the Acoustical Society of America*, v. 140, n. 6, p. 4350–4359, 2016.

PICARD, C.; DELVILLE, J. Pressure velocity coupling in a subsonic round jet. *International Journal of Heat and Fluid Flow*, v. 21, n. 3, p. 359 – 364, 2000. ISSN 0142-727X.

POKORA, C. D.; MCGUIRK, J. J. Stereo-PIV measurements of spatio-temporal turbulence correlations in an axisymmetric jet. *Journal of Fluid Mechanics*, Cambridge University Press, Cambridge, UK, v. 778, p. 216–252, 009 2015.

POTT-POLLENSKE, M. Aeroacoustic characteristics of externally blown flap systems. In: *17thAIAA/CEAS Aeroacoustics Conference*. [S.l.]: American Institute of Aeronautics and Astronautics, 2011.

QIAN, Y. H.; D'HUMIÈRES, D.; LALLEMAND, P. Lattice BGK models for navier-stokes equation. *Europhysics Letters*, v. 17, p. 479–484, 1992.

REBA, R.; NARAYANAN, S.; COLONIUS, T. Wave-packet models for large-scale mixing noise. *International Journal of Aeroacoustics*, v. 9, n. 4-5, p. 533–557, 2010.

RIBNER, H. S. Quadrupole correlations governing the pattern of jet noise. *Journal of Fluid Mechanics*, Cambridge University Press, Cambridge, UK, v. 38, n. 1, p. 1–24, 08 1969.

ROSA, V. H.; SELF, R.; ILÁRIO, C.; NAQAVI, I.; TUCKER, P. Modelling velocity correlations with LES and RANS for prediction of noise from isothermal or hot jets. In: . [S.l.]: American Institute of Aeronautics and Astronautics, 2016.

SAGAUT, P. Theoretical background: Large-eddy simulation. In: WAGNER, C.; HÜTTL, T.; SAGAUT, P. (Ed.). *Large-Eddy Simulation for Acoustics*. [S.l.]: Cambridge University Press, 2007. chap. 3, p. 89–127.

SAMANTA, A.; FREUND, J. B.; WEI, M.; LELE, S. K. Robustness of acoustic analogies for predicting mixing-layer noise. *AIAA Journal*, American Institute of Aeronautics and Astronautics, v. 44, n. 11, p. 2780–2786, Nov. 2006. ISSN 0001-1452.

SANDHAM, N.; MORFEY, C.; HU, Z. Sound radiation from exponentially growing and decaying surface waves. *Journal of Sound and Vibration*, v. 294, n. 1-2, p. 355 – 361, 2006. ISSN 0022-460X.

SCHMIDT, O. T.; TOWNE, A.; COLONIUS, T.; CAVALIERI, A. V. G.; JORDAN, P.; BRÈS, G. A. Wavepackets and trapped acoustic modes in a turbulent jet: coherent structure eduction and global stability. *Journal of Fluid Mechanics*, Cambridge University Press, v. 825, p. 1153–1181, 2017.

SELF, R. Jet noise prediction using the Lighthill acoustic analogy. *Journal of Sound and Vibration*, v. 275, p. 757 – 768, 2004. ISSN 0022-460X.

SHEARIN, J. G. *Investigation of Jet-Installation Noise Sources Under Static Conditions*. [S.l.], 1983.

SHIN, K.; HAMMOND, J. K. *Fundamentals of Signal Processing for Sound and Vibration Engineers*. [S.l.]: John Wiley & Sons, 2008.

SHIVASHANKARA, B. N.; BLACKNER, A. M. Installed jet noise. In: *3rd AIAA/CEAS Aeroacoustics Conference*. [S.l.]: American Institute of Aeronautics and Astronautics, 1997. p. 138–148.

SINHA, A.; RODRÍGUEZ, D.; BRÈS, G. A.; COLONIUS, T. Wavepacket models for supersonic jet noise. *Journal of Fluid Mechanics*, Cambridge University Press, Cambridge, UK, v. 742, p. 71–95, 003 2014.

SMAGORINSKY, J. General circulation experiments with the primitive equations. I. the basic experiment. *Monthly Weather Review*, v. 91, n. 3, p. 99–163, March 1963.

SMITH, M. J. T. *Aircraft Noise*. [S.l.]: Cambridge University Press, 1989.

SUCCI, S. *The Lattice Boltzmann Equation for Fluid Dynamics and Beyond*. Roma, Italy: Clarendon Press, 2001.

SUZUKI, T.; COLONIUS, T. Instability waves in a subsonic round jet detected using a near-field phased microphone array. *Journal of Fluid Mechanics*, v. 565, p. 197–226, 10 2006. ISSN 1469-7645.

TAM, C. K. W. Jet noise: Since 1952. *Theoretical and Computational Fluid Dynamics*, v. 10, p. 393–405, 1998.

TAM, C. K. W.; AURIAULT, L. Jet mixing noise from fine scale turbulence. *AIAA Journal*, v. 37, p. 145–153, 1999.

TAM, C. K. W.; GOLEBIOWSKI, M.; SEINER, J. M. On the two components of turbulent mixing noise from subsonic jets. In: *2nd AIAA/CEAS Aeroacoustics Conference*. [S.l.]: American Institute of Aeronautics and Astronautics, 1996.

TEIXEIRA, C. M. Incorporating turbulence models into the lattice-boltzmann method. *International Journal of Modern Physics C*, v. 09, n. 08, p. 1159–1175, 1998.

TINNEY, C. E.; JORDAN, P. The near pressure field of coaxial subsonic jets. *Journal of Fluid Mechanics*, v. 611, p. 175–204, 2008.

TISSOT, G.; ZHANG, M.; LAJÚS, F. C.; CAVALIERI, A. V. G.; JORDAN, P. Sensitivity of wavepackets in jets to nonlinear effects: the role of the critical layer. *Journal of Fluid Mechanics*, Cambridge University Press, Cambridge, UK, v. 811, p. 95–137, 001 2017.

TOWNE, A.; CAVALIERI, A. V. G.; JORDAN, P.; COLONIUS, T.; SCHMIDT, O.; JAUNET, V.; BRÈS, G. A. Acoustic resonance in the potential core of subsonic jets. *Journal of Fluid Mechanics*, Cambridge University Press, v. 825, p. 1113–1152, 2017.

UZUN, A. *3-D Large Eddy Simulation for Jet Aeroacoustics*. PhD Thesis — Purdue University, December 2003.

UZUN, A.; LYRINTZIS, A. S.; BLAISDELL, G. A. Coupling of integral acoustic methods with LES for jet noise prediction. *International Journal of Aeroacoustics*, 2005.

VISWANATHAN, R.; UNDERBRINK, J. R.; BRUSNIAK, L. Space-time correlation measurements in nearfield of jets. In: *16th AIAA/CEAS Aeroacoustics Conference*. [S.l.]: American Institute of Aeronautics and Astronautics, 2010.

WANG, M. E. Wing effect on jet noise propagation. In: *AIAA 6th Aeroacoustics Conference*. [S.l.]: American Institute of Aeronautics and Astronautics, 1980.

WELCH, P. The use of fast fourier transform for the estimation of power spectra: A method based on time averaging over short, modified periodograms. *IEEE Transactions on Audio and Electroacoustics*, v. 15, n. 2, p. 70–73, Jun 1967. ISSN 0018-9278.

XIA, H.; TUCKER, P. G.; EASTWOOD, S.; MAHAK, M. The influence of geometry on jet plume development. *Progress in Aerospace Sciencies*, v. 52, p. 56–66, July 2012.

ZHANG, R.; SHAN, X.; CHEN, H. Efficient kinetic method for fluid simulation beyond the navier-stokes equation. *Phys. Rev. E*, American Physical Society, v. 74, p. 046703, Oct 2006.